Intense femtosecond laser interactions with ions in beams and traps

Jofre Pedregosa Gutierrez

Intense Femtosecond Laser Interactions with Ions in Beams and Traps

A thesis presented on application for the degree of Doctor of Philosophy in the Faculty of Engineering and Physical Sciences by

Jofre Pedregosa Gutierrez

BSc 2002

Department of Pure and Applied Physics

The Queen's University of Belfast

Northern Ireland

January 2006

Sense vosaltres avui no seria qui soc.
Sense vosaltres avui no estaria aqui.
Sempre heu estat, esteu i estareu dintre meu.
Gracies.

This thesis is dedicated to my parents.

Acknowledgements

I would like to express my sincere thanks and gratitude to everyone who has supported me during and/or contributed to the research presented in this thesis.

First of all, I owe an enormous debt of gratitude to my supervisor Jason Greenwood, for all his help and support. Jason's enthusiasm and approachability have made this three years of research a pleasure. Thanks for believing on me.

To all my colleagues, past and present, I would like to express thanks. To Gerry for show me the way during my early days in the team. To Philip for his support, specially in the stressful months on Germany. To Jarlath, for so many good discussions about physics.

I am extremely grateful to John Costello for his help, advise and helpful discussions. Thanks also to Robert Moshammer and his team in the Max Plank Institute for the support received during the months in Heidelberg.

I would like to thanks also Ian Williams for his support and help in the ion trap project. Thanks also to Bob McCullough for letting us use the ECR ion source, to Mansukh Shah for his encouragement, so much needed at the start. Thanks also to all the staff an students of the Atomic and Molecular Physics Research Division at QUB and the staff of the mechanical and electrical workshops, specially Kieran McAreavey, for so many advise and helpfulness during this years.

Finally, to all my family and friends and to a very special person, my future wife, Alice, for all their patience, encouragement and support, thanks.

Abstract

The interaction of intense ($> 10^{14} W/cm^2$), ultra-short laser light with atoms and molecules has led to the discovery of new phenomena such as bond softening, enhanced ionization and high harmonic generation. Some of these processes are believed to proceed through a re-scattering process where an electron is ionized, propagated in the laser field and is driven back to the core. This thesis describes the techniques used in preparing ionic targets for interaction with intense, femtosecond lasers, and the outcomes and analysis of this work.

While the study of ionic species is considerably more difficult than for neutrals, it enables access to species which are of theoretical interest. H_2^+ is the most fundamental molecule and therefore the most amenable for quantum calculations. Meanwhile, the potential experienced by an electron detached from a negative ion by an intense laser is non-Coulombic, which is in contrast to that experienced in a neutral atom.

Multiple ionization of negative ions in an intense laser field has been studied experimentally for I^- and F^- as a function of laser intensity and ellipticity. For I^-, it was found that there was no discernable difference between ionization yields when using linearly and circularly polarized light, indicating that a sequential ionization process was completely dominant. For F^-, once the sequential component of the signal was estimated using a tunnel ionization theory, there was a clear enhancement in the double ionization signal for the linearly polarized light at lower intensities. This is interpreted as the first experimental evidence for the re-scattering process occurring in negative ions which is supported by very recent theoretical work.

The design, simulation, construction, and testing of a linear electrostatic ion storage device, which behaves as a charge particle optics analog of a laser cavity, is also reported. By trapping ions, the internal energies of the

ions can be manipulated to allow the study of ions in prepared states. This would be desirable in, for example, the study of ionization and dissociation of H_2^+ by intense lasers. To date experimental work has been limited by the broad population of vibrational states in H_2^+ which makes interpretation of time of flight spectra difficult. Trapping ions enables long-lived excited states of atomic and molecular ions to decay into their ground state or provides sufficient time for excitation, de-excitation or destruction by a laser.

The conditions for optimum trapping have been simulated and confirmed experimentally. A range of positive and negative ions have been trapped with this device with lifetimes of several hundred milliseconds. Preliminary studies of the interaction of trapped ions with femtosecond laser pulses have been performed, which demonstrate that the excited state population in Al_2^- can be influenced dynamically.

Contents

Part I

Interaction of intense laser pulses with negative ions

Chapter 1

Atomic Structure

The aim of this chapter is to review the basic concepts of quantum mechanics and how we apply them to the study of the atomic structure at a basic level. For a more complete exposition, the author recommends the excellent book by Sakurai,"Modern Quantum Physics" [1]

1.1 Quantum Mechanics Formalisms

Let's start by how a physical state is defined in quantum mechanics. We represented the state of an atom (or any other physical state) by a state vector in a complex vector space. We call such a vector a **ket** and denote it by $|\alpha\rangle$. This will generate the ket-space, but we can also generate a dual correspondence space, which we call **bra**-space, and denote it by $\langle\alpha|$. A bra and ket talk to each other through the inner product (equivalent of a scalar product in Euclidean space), for example:

$$\langle\beta|\alpha\rangle = (\langle\beta|) \cdot (|\alpha\rangle) \tag{1.1}$$

We can also write, what is known as the outer product:

$$|\beta\rangle\langle\alpha| = (|\beta\rangle) \cdot (\langle\alpha|) \tag{1.2}$$

Both are essentially different, while from the inner product we obtain a complex number, with the outer product the resultant is regarded as an operator.

One of the postulates of quantum mechanics is that a ket (or a bra) contain complete information about the physical state.

A second postulate is that an *observable*, such as momentum and spin components, can be represented by an **operator** in the vector space in question. The operator A acts over a state in the following form:

$$A \cdot (|\alpha\rangle) = a|\alpha\rangle \tag{1.3}$$

$$(\langle\alpha|) \cdot A = a\langle\alpha| \tag{1.4}$$

where we have assumed that $|\alpha\rangle$ is an eigenket of operator A, and we call a the eigenvalue of operator A.

1.2 Measurements

When we are going to do a measurement of the observable A, the system is assumed to be represented by some linear combination of eigenstates:

$$|\alpha\rangle = \sum_{a'} |a'\rangle\langle a'|\alpha\rangle = \sum_{a'} c_{a'}|a'\rangle \tag{1.5}$$

but when we actually perform the measurement, the system collapses into one of the eigenstates, $|a'\rangle$ for example, of the observable A:

$$|\alpha\rangle \rightarrow A\ measurement \rightarrow |a'\rangle \tag{1.6}$$

So a *measurement generally changes the state*!, except in the case when the state is already in one of the eigenstates of the observable being measured. What equation 1.6 is telling us is that we can not say which value of $|a'\rangle$ we are going to read as a result of the measurement. But, one of the fundamental

postulates of quantum mechanics [1] tells us that what we can know is the probability of jumping into some particular $|a'\rangle$ state, and that is given by

$$\text{Probaility for } a' = P(a') = |\langle a'|\alpha\rangle|^2 \tag{1.7}$$

assuming that $|\alpha\rangle$ is normalized.

We define the **expectation value** of A, taken with respect to state $|\alpha\rangle$, as

$$\langle A\rangle \equiv \langle\alpha|A|\alpha\rangle \tag{1.8}$$

$\langle A\rangle$ could be interpreted as an averaged measured value.

1.3 Quantum Dynamics

Let's study now the time evolution of a state ket:

$$|\alpha, t_0\rangle = |\alpha\rangle \rightarrow \text{time evolution} \rightarrow |\alpha, t\rangle, \quad (t > t_0) \tag{1.9}$$

We define the time-evolution operator $U(t, t_0)$ as:

$$|\alpha, t\rangle = U(t, t_0)|\alpha, t_0\rangle \tag{1.10}$$

Everything that has to do with time evolution follows from the Schrödinger equation[2] for the time-evolution operator[3]:

$$i\hbar\frac{\partial}{\partial t}U(t, t_0) = HU(t, t_0) \tag{1.11}$$

where H is the Hamiltonian operator of the system and $\hbar = 6.5821220 \cdot 10^{-16} eVs$.

If we assume that H is time independent, the solution of the equation 1.11 is

$$U(t, t_0) = \exp[\frac{-iH(t - t_0)}{\hbar}] \tag{1.12}$$

[1] Which is known as the *Born's interpretation*, for which Max Born obtain the Nobel Prize for physics in 1954

[2] That is true for a non-relativistic description of quantum mechanics.

[3] The units used in this chapter are S.I.

While Dirac's notation in terms of bra and ket is extremely useful, in atomic physics it is more common to talk in terms of waves functions,$\Psi(\mathbf{x}, t)$, in which case, we just need to project our ket space over the x-representation:

$$\Psi(\mathbf{x}, t) = \langle \mathbf{x} | \alpha, t_0; t \rangle \tag{1.13}$$

Multiplying both side of 1.11 by $|\alpha, t_0\rangle$ on the right and using 1.10 we can write the Schrödinger equation for a state ket as:

$$i\hbar \frac{\partial}{\partial t} |\alpha, t_0; t\rangle = H |\alpha, t_0; t\rangle \tag{1.14}$$

If the Hamiltonian is taken to be:

$$H = \frac{\mathbf{p}^2}{2m} + V(x) \tag{1.15}$$

where $\mathbf{p}$ is the momentum of the particle with mass m in a potential $V(x)$, multiplying both sides of 1.14 by $\langle x|$, together with 1.13, we obtain the Schrödinger equation for a ket-state written explicitly in the x-basis:

$$i\hbar \frac{\partial}{\partial t} \Psi(\mathbf{x}, t) = -\frac{\hbar^2}{2m} \nabla^2 \Psi(\mathbf{x}, t) + V(x) \Psi(\mathbf{x}, t) \tag{1.16}$$

where we have used $\mathbf{p} \rightarrow -i\hbar\nabla$

If we are interested in a time-independent problem, we can reduce 1.16 to:

$$-\frac{\hbar^2}{2m} \nabla^2 \Psi(\mathbf{x}) + V(\mathbf{x}) \Psi(\mathbf{x}) = E \Psi(\mathbf{x}) \tag{1.17}$$

where E is the eigenvalue for the hamiltonian, also know as the energy of the system.

1.4 One-Electron Atoms

For a one electron atom with a nucleus of charge Ze and mass M, the Hamiltonian of the system is

$$H = \frac{p^2}{2\mu} - \frac{Ze^2}{(4\pi\epsilon_0) r} \tag{1.18}$$

where r is the distance between the nucleus and the electron, and $\mu = \frac{mM}{m+M}$ (m being the mass of the electron), is the reduced mass. Using 1.17, we can write:

$$\left[-\frac{\hbar^2}{2\mu}\nabla^2 - \frac{Ze^2}{(4\pi\epsilon_0)r} \right] \Psi(\mathbf{r}) = E\Psi(\mathbf{r}) \tag{1.19}$$

One electron systems are a special case because we can solve 1.19 analytically. Thanks to the symmetry of the potential, we can separate the 1.19 into spherical polar coordinates, and after some work, find out that the general solution for the bound states with principal quantum number n and orbital angular momentum quantum number l with m being its projection, can be expressed as:

$$\psi_{nlm}(r,\theta,\phi) = R_{nl}(r)Y_{lm}(\theta,\phi) \tag{1.20}$$

$$\begin{aligned} R_{nl} &= \{(\frac{2Z}{na_\mu})^3 \frac{(n-l-1)!}{2n[(n+1)!]^3}\}^{1/2}\ exp(-\rho/2)\ \rho^l\ L_{n+1}^{2l+1}(\rho) \\ \rho &= \frac{2Z}{na_\mu} \\ a_\mu &= \frac{4\pi\varepsilon_0\hbar^2}{\mu e^2} = a_0\frac{m}{\mu} \end{aligned}$$

where R_{nl} are known as radial functions, Y_{lm} are the well known spherical harmonics and a_0 is the Bohr radius.

The energy levels can be express as

$$E_n = -\frac{1}{2}\mu c^2 \frac{(Z\alpha)^2}{n^2} \tag{1.21}$$

where $\alpha = e^2/(4\pi\varepsilon_0\hbar c)$ is the fine structure constant.

1.5 Many-electron atoms

In the non-analytical case of the many-electron problem, an accurate quantum mechanical description of an atomic system should take into account:

1. The kinetic energy of the electrons and their potential energy in the electrostatic attractive field of the nucleus (assumed to be point-like and infinitely massive).

2. The electrostatic repulsion between the electrons.

3. The magnetic interactions of the electronic spins with their orbital motion.

4. Several small effects: spin-spin interaction between the electrons, relativistic effects, radiative corrections and nuclear corrections (due to the finite mass of the nucleus, its finite extension, etc)

To take into account all the points mentioned above is a very difficult task. The simplest model starts by taking into account in the Hamiltonian just the first two points mentioned above. A lot of corrections can be introduced, but a more rigorous treatment will lead to the use of Dirac's equation, which is the relativistic version of Schrödinger equation, where the spin dependent interactions (as well as the relativistic effects) are treated correctly. Still, Dirac's theory does not allow for interactions in which the number of particles in a system changes. To take this into account, the relativistic field theory, known as QED (Quantum Electrodynamics), needs to be used.

When the Schrödinger equation is used, a common simplification is the central field approximation, in which each electron moves in an effective potential which represents the attraction of nucleus and the average effect of the repulsive interaction between this electron and the (N-1) other electrons. This approximates the effective potential energy of an electron by a spherically symmetric potential. This is not the place for an extensive description on many-electron atoms, what is interesting here is to introduce the negative ions.

1.6 Negative Ions

An isolated atom is a neutral particle at large distances, so how is it that an entity that is considered neutrally charge is able to attached an extra electron? Let's perform a simple calculation for the hydrogen case to demonstrate how this is possible. If we regard the nucleus as a point charge of $+e$ and the charge of the atomic electron spreads out in a spherically symmetrical cloud around the nucleus, then we can write the potential generated by the fraction, α, of the total charge of the atomic electron contained within a distance r_1, as $V_1 = e(1-\alpha)/r_1$. If we consider that the remaining charge is all concentrated in a sphere of radius r_1 it will give a potential of $V_2 = -e(1-\alpha)/r_1$, therefore neutralizing V_1. But the charge is actually distributed from 0 to ∞, so the second potential is actually $V_2 = \beta e(\alpha - 1)/r_1$, where $\beta < 1$. So the total potential energy created by the atomic charge is

$$V(r_1) = -(1-\beta)(1-\alpha)e^2/r_1 \tag{1.22}$$

and so is negative, therefore the extra electron will feel an attractive force. Furthermore, since

$$\lim_{r_1 \to \infty} (1-\beta(r_1))(1-\alpha(r_1)) \to 0 \tag{1.23}$$

the effective field acting on the electron falls off much more rapidly with distance than a Coulomb field. The simple calculation presented above is equivalent to the physical situation of an electron approaching an atom. In this situation, the electric field associated with the charge of the incident electron polarizes the charge cloud of the atom, in the same way that the Van der Waals interaction between neutral atoms is the result of a mutual polarization effect by which each atom acquires an induced dipole moment. If the dipole moment induced by the approaching electron in the atom is sufficiently strong to bind the incident electron, it will form a negative ion. The polarization of the atom is due to strong correlations between the incident electron and the atomic electrons, therefore the study of negative ions

allows us to gain a better understanding of the limitations of the independent electron model.

The structure of a negative ion is qualitatively different from that of an atom or positive ion. In atoms and positive ions, the relatively strong Coulomb force creates a $1/r$ potential that is able to generate an infinite spectrum of bound states that converge on the ionization limit. Negative ions behave radically differently, their outermost electron experiences a much weaker and short-range potential, leading to a finite number of stationary states (and rare excited states). The weakness of the binding is reflected in the fact that binding energies, or electron affinities (defined as $EA(X) = E_0(X) - E_0(X^-)$, where E_0 is the energy of the ground state), are typically an order of magnitude smaller that the ionization energies of atoms, see table 1.1.

In table 1.1, the ground state term has been written according to Russell-Saunders notation

$$^{2S+1}L_{\mathcal{J}} \tag{1.24}$$

where $\mathcal{J}$ is the total angular momentum quantum number and code letters S, P, D, ... correspond to the values $L = 0, 1, 2, \ldots$. of the total orbital angular momentum quantum number L, where

$$L = |l_1 - l_2|, |l_1 - l_2| + 1, \ldots, l_1 + l_2 \tag{1.25}$$

The same applies upon adding two spins S_1, S_2 and for $\mathcal{J}$:

$$\begin{aligned} S &= |s_1 - s_2|, |s_1 - s_2| + 1, \ldots, s_1 + s_2 \\ \mathcal{J} &= |L - S|, |L - S| + 1, \ldots, L + S \end{aligned} \tag{1.26}$$

1.6.1 Radial Charge Density

Another consequence of the weaker potential is that the *size* of the negative ions are bigger than their neutral colleagues. Again, let's take H^- and cal-

Table 1.1: Experimental electron affinities and ionization potential for some elements from different groups. The EA values are taken from Andersen et al [2], and the Ip from NIST [3].

	Negative ion	Electron affinity	Neutral atom	Ionization potential
	$H^-[1s^2\ {}^1S_0]$	0.754195(20)eV	$H[1s\ {}^2S_{1/2}]$	13.5984eV
Alkali metal	$Li^-[2s^2\ {}^1S_0]$	0.618049(20)eV	$Li[2s\ {}^2S_{1/2}]$	5.3917eV
	$K^-[4s^2\ {}^1S_0]$	0.501459(12)eV	$K[4s\ {}^2S_{1/2}]$	4.3407eV
Alkaline earths	$Ca^-[4s^24p\ {}^2P_{1/2}]$	24.55(0.10)meV	$Ca[4s^2\ {}^1S_0]$	6.1132eV
Group III	$Al^-[3s^23p^2\ {}^3P_0]$	432.83(5)meV	$Al[3s^23p\ {}^2P_{1/2}]$	5.9858ev
Group IV	$C^-[2s^22p^3\ {}^4S_{3/2}]$	1.262119(20)eV	$C[2s^22p^2\ {}^3P_0]$	11.2603eV
Group VI	$O^-[2s^22p^5\ {}^2P_{1/2}]$	1.4611107(17)eV	$O[2s^22p^4\ {}^3P_2]$	13.6181eV
Halogens	$F^-[2s^22p^6\ {}^1S_0]$	3.4011895(25)eV	$F[2s^22p^5\ {}^2P_{3/2}]$	17.4228eV
	$Cl^-[3s^23p^6\ {}^1S_0]$	3.612724(27)eV	$Cl[3s^23p^5\ {}^2P_{3/2}]$	12.9676eV

culate its radial charge distribution. The two-particle radial charge density is given by:

$$\rho(r_1, r_2) = \int\int |\psi(r_1, r_2)|^2 \sin\theta_1 d\theta_1 d\phi_1 \sin\theta_2 d\theta_2 d\phi_2 \tag{1.27}$$

where $0 \leq \theta \leq \pi$ and $0 \leq \phi \leq 2\pi$. Integrating over r_2 we obtain one-particle radial density distribution:

$$D(r_1) = 2\int_0^\infty \rho(r_1, r_2) r_1 r_2 dr_2 \tag{1.28}$$

Searching in text books we find [4] the following *simple* wavefunctions, that will serve us perfectly for the aims of this calculation:

1. The simple product function

$$\psi_a = N\exp\{-Z(r_1 + r_2)\} \tag{1.29}$$

   with Z=0.6875 in atomic units. This wavefunction does not include correlation between the two electrons.

2. The so-called function of Shull and Lowdin [5]

$$\psi_b = N[\exp\{-ar_1 - br_2\} + \exp\{-ar_2 - br_1\}] \tag{1.30}$$

   with a=1.0392 and b=0.2832 in atomic units. This expression includes radial but not angular correction.

3. The wavefunction for the neutral Hydrogen:

$$\psi_c = R_{10} = 2(Z)^{3/2}\exp\{-Zr\} \tag{1.31}$$

   in atomic units.

In the book of Massey [4], neither the values for the normalization constant nor the explicit form of the $D(r)$ are provided, so we will need to calculate them first. To normalize the wave function we need to calculate:

$$1 = \int\int |\psi(r_1, r_2)|^2 r_1 r_2 \sin\theta_1 \sin\theta_2 dr_1 dr_2 d\theta_1 d\theta_2 d\phi_1 d\phi_2 \tag{1.32}$$

The first case leads to $N = Z^3/\pi$, giving a radial density distribution of:

$$D(r_1) = 8Z^3 r_1^2 \exp\{-2Zr_2\} \tag{1.33}$$

In the second case the normalization constant takes the form of $N^2 = \frac{1}{(4\pi)^2}[\frac{1}{(2ab)^3} + \frac{2^3}{(a+b)^6}]^{-1}$, and leads to a density distribution expressed as:

$$D(r_1) = 2(4\pi)^2 N^2 \; r_1^2 \Big[\frac{1}{4b^3} e^{-2ar_1} + \frac{1}{4a^3} e^{-2br_1} + \frac{4}{(a+b)^3} e^{-(a+b)r_1}\Big] \tag{1.34}$$

For the case of the atomic hydrogen in its ground state:

$$D(r) = r^2 |R(r)|^2 = 4r^2 e^{-2r} \tag{1.35}$$

If we plot these three functions we obtain figure 1.1, from where we can clearly see that the introduction of radial correlation increase the spread of the charge with respect to the neutral case, as it tends to keep the electrons relatively further apart.

Another illustrative calculation is to consider the average value of the distance r:

$$\langle r \rangle = \int \psi^\star(r_1, r_2)(r_1 + r_2)\psi(r_1, r_2) d\overrightarrow{r_1} d\overrightarrow{r_2} \tag{1.36}$$

For ψ_a we find that $\langle r \rangle_a = 3/Z = 4.364 a.u.$, for ψ_b is $\langle r \rangle_b = 6.225 a.u.$, and the value of $\langle r \rangle$ for hydrogen atom being just $1.5 a.u.$. These values gives us an idea of the increase in the size of the negative ion (a value of $5.420 a.u.$ is obtained when more accurate models[6] are used) compared with neutral atoms.

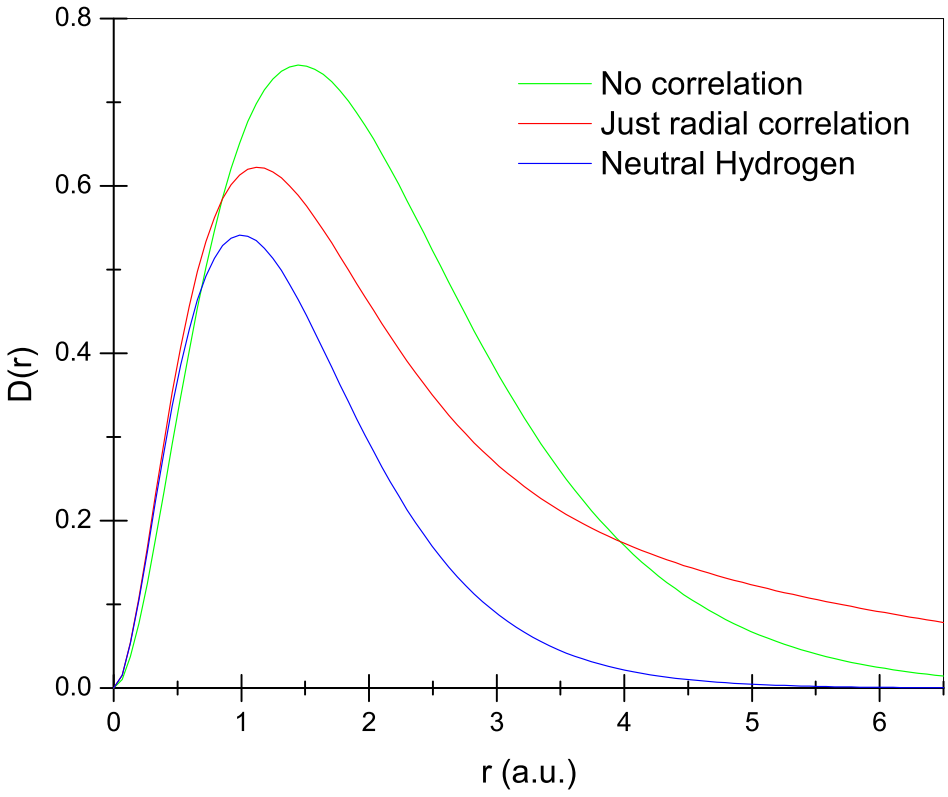

Figure 1.1: Single-particle density distribution D(r) for H^-, calculated using various approximate wave functions (see text).

References

[1] J. J. Sakurai, *Modern Quantum Mechanics*, 3rd ed. (University of Bangalore Press, Menlo Park, CA: Benjamin/Cummings, 1985).

[2] T. Andersen, Phys. Reports **394**, 157 (2004).

[3] National Insitute of Standars and Technology, http://www.nist.gov/.

[4] S. H. Massey, *Negative Ions*, 3rd ed. (Cambridge Universty Press, London, 1972).

[5] H. Shull and O. Lowdin, J. Chem. Phys. **25**, 1035 (1956).

[6] C. L. Pekeris, Phys. Rev. **126**, 1470 (1962).

Chapter 2

Theoretical and Experimental Review

In this chapter, both experimental and theoretical reviews are presented together to reflect how close has been their evolution in the field of the strong fields interaction with atoms and ions. The aim is to introduce the current knowledge of how light, usually in the form of a laser pulse, interacts with an atom (or ion), in the regime of strong fields and focusing in multiphoton processes and rescattering effects.

2.1 Basics

When the interaction of an atom with radiation is considered, three different basic situations are found. First, an atom can make a spontaneous transition from an excited state to a state with lower energy, emitting a photon. Second, when an atom is radiated, the atom can absorb photons from this radiation, making a transition from a lower to higher energy state (this higher energy state can be in the continuum: the atom has been ionized). Finally, atoms can also emit photons under the influence of a radiation field, this is called stimulated emission.

In this thesis the process of interest is the irradiation of atoms with laser light, mainly giving rise to ionization (or photodetachment for negative ions).

A rigorous treatment of this kind of phenomena would require the use of QED, where the electromagnetic field is expressed in terms of its quanta (the photons). But when the photon density exceeds one per cubic wavelength, the quantum description in terms of photons is no longer required to treat the interaction correctly, so the light can be considered as a classical field [1]. For typical values of the laser field used in this thesis ($I \simeq 10^{14} W/cm^2$ and $\lambda = 800nm$) the photon density is

$$\rho = \left(\frac{I}{\hbar c^2/\lambda}\right) \cdot \lambda^3 \approx 10^{10} \text{ photons per cubic wavelength} \tag{2.1}$$

So the semiclassical approximation of describing the atom as a quantum system but the electromagnetic field classically, is clearly well justified.

Multiphoton absorption processes leading to the detachment of an electron from an atom (Multiphoton Ionization, MPI) have been reported since the discovery that lasers could be made to generate moderately intense pulses by Q-switching them (see for example [2]). In a MPI process, the electron absorbs two or more photons, which can be understood as a fast sequential process through virtual states allowed by the uncertainty principle:

$$\Delta E \Delta t \geq \frac{\hbar}{2} \tag{2.2}$$

which allows the electron to have a forbidden energy for a short period of time.

It was quickly realized that ionization was proceeding by a nonlinear multiphoton absorption process which was easily described within the framework of perturbation theory. However, in the last 20 years, the development of ultrashort (femtosecond) pulse lasers has opened up intensity regimes where perturbation theory is no longer valid. In this regime the photon density

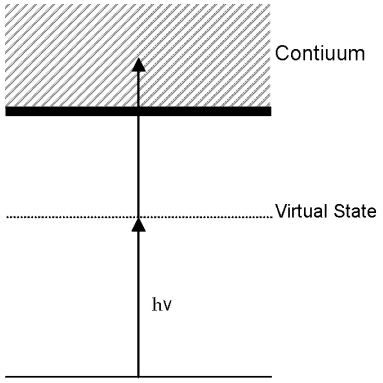

Figure 2.1: Example of a two photon process with a virtual state.

is so high that ionization proceeds via tunnelling of an electron through the barrier created from the superposition of the atomic potential with the macroscopic electric field potential of the laser pulse.

The transition from the multiphoton or perturbative to the tunnelling or nonperturbative regimes has resulted in the discovery of many new phenomena. This transition is usually presented in terms of the value of the Keldysh parameter γ [3] which is the ratio of the frequency of the radiation to the tunnelling rate of the bound electron. These new phenomena include enhancements in multiple ionization yields, energetic electron emission, and the generation of high harmonics to very high order.

In this next section a review of the physics of the multiphoton processes is undertaken.

2.2 Multiphoton Ionization

In early experiments multiphoton ionization (MPI) was accurately modelled by lowest-order perturbation theory (LOPT) [4], where ionization rate (Γ) is proportional to the n^{th} power of the photon flux J, and the process is

described by the generalized n-photon cross section (σ_n):

$$\Gamma_n = \sigma_n J^n \qquad [a.u.] \tag{2.3}$$

where n is the minimum number of photons needed for ionization, and J is

$$J = cF^2/(8\pi w) = I/w \qquad [\text{a.u.}] \tag{2.4}$$

where F is the amplitude of the electric field and w is the energy of one photon. This response is highly nonlinear and has been verified experimentally up to $n = 22$ in the MPI of atomic helium by Nd:YAG laser fields [5].

Despite the relative simple appearance of equation 2.3, σ_n is difficult to calculate since high-order processes are needed to ensure an accurate perturbative description. Further complications occur when near-resonant and resonant behavior is investigated [6]. The perturbative approach breaks down as the intensity of the incident light increases: the atomic states involved can no longer be considered as unperturbed since they shift in a dynamic fashion in pulsed fields due to strong coupling with the laser field (AC-Stark shift).

2.2.1 Above-threshold Ionization

The non-perturbative nature of strong-field MPI particularly manifests itself in the effects related to above-threshold ionization (ATI). ATI is nothing else than a MPI process by more photons than the minimum number required. Its origin lies in the field-induced distortion of the atomic potential. It results from the absorption of photons by the exiting photo-ionized electron while still under the influence of the atomic potential. Again, perturbation theory has been applied obtaining a further generalization of equation 2.3:

$$\Gamma_{n+s} \propto J^{n+s} \tag{2.5}$$

where s is the number of excess photons absorbed. This has been verified experimentally [4]. The equation describing the photoelectron energy is simply

an extension of the Einstein photoeffect formula

$$E = (n + s)\hbar\omega - I_p \qquad [S.I.] \tag{2.6}$$

where I_p is the ionization potential. Figure 2.2.1 shows ATI peaks in a photoelectron energy spectrum spaced by $\hbar\omega$ from Yergeau [7]. It is possible to observe the suppression of first peaks as the energy of the pulse increased. This is an evidence of fundamental breakdown of the perturbative approach, due to the role played by high-order processes when the pulse energy is increased.

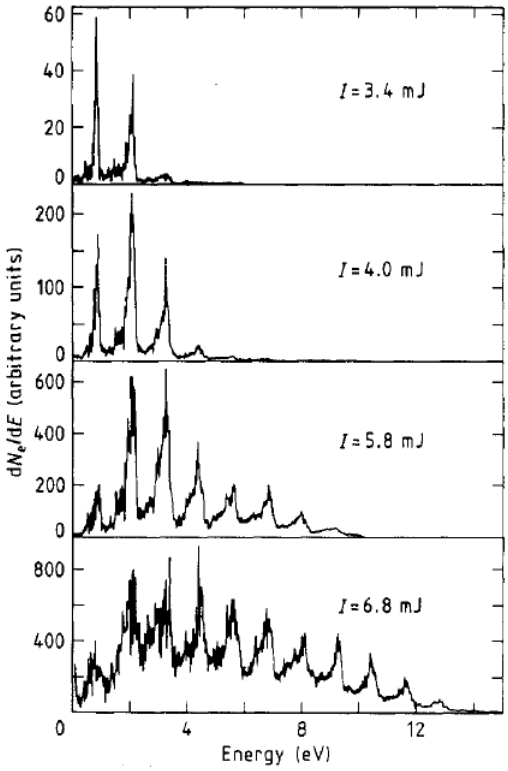

Figure 2.2: Photoelectron energy spectrum showing above-threshold peaks spaced by $\hbar\omega$ from Yergeau [7], showing peak switching as pulse energy is increased form 3.4mJ to 6.8mJ.

The explanation of the peak suppression lies in the AC-Stark shifts of the atomic bound states induced by the laser field. When a free electron is placed in a laser field it possesses, in addition to any translational kinetic

energy, a quiver energy due to the oscillatory motion imparted on it by the field. This quiver energy is the so-called ponderomotive energy [1], U_p, and is given by

$$U_p = \frac{e^2 F^2}{4m\omega^2} \qquad [S.I.] \tag{2.7}$$

where e is the charge of the electron, F the local instantaneous electric field, m the mass of the electron and ω the angular frequency of the laser field. If the intensity is expressed in W/cm^2 and the wavelength λ in nm, then

$$U_p[eV] = 9.33 \cdot 10^{-20} I\Big[\frac{W}{cm^2}\Big]\lambda^2[nm] \tag{2.8}$$

where U_p is in eV. When the laser field is very intense it will also have a noticeable effect on bound electrons. In this case, because Rydberg levels are weakly bound, their induced shifts are very close to the ponderomotive energy, while states nearer the nucleus have a much smaller polarizability and will be harder to influence so the shift of low states can be neglected. This means that the ionization potential increase by approximately U_p, so if the laser field is large enough, it will prohibit ionization through the low-order channels, see figure 2.2.1. In a smoothly varying pulse the channels close to the intensity of the pulse rises (see section 4.3.1 for a further explanation) and they open again as the pulse vanishs, so the corresponding peak in the photoelectron spectrum will not completely vanish.

The interpretation just given above, can lead to a discrepancy where the new photoelectron final energy is now written as

$$E = (n + s)\hbar\omega - (I_p + U_p) \tag{2.9}$$

Earlier it was said that experimentally, equation 2.6 explained the energy of the emitted electrons. The reason for this is that as the electron leaves the laser focus it experiences a force, $-\nabla U_p$, due to the laser inhomogeneity, which is then converted into energy [9]. The energy which the electron gains

[1] A formal derivation of this expression can be found in [8]

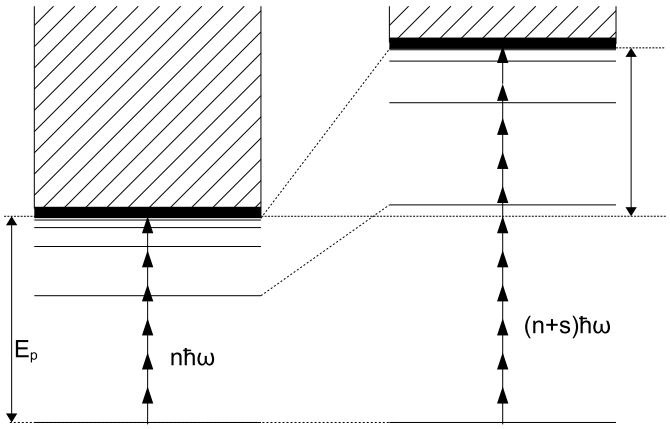

Figure 2.3: Schematics of multiphoton ionization: on the left, at low intensity, n photons are required to promote the electron to the continuum, but at higher intensities, the outer states and the continuum threshold are shifted, increasing the ionization potential by U_p, so that an additional s photons are required for the ionization.

by "sliding" down this potential is exactly equal to U_p, thus cancelling the decrease in energy caused by the increase in the ionization potential. Again, the last argument is valid just in the case that the laser pulse is long enough for the electron to *slide* out of the laser field. The time needed for a liberated electron to leave the laser focus is approximately 10ps depending on its initial energy and the size of the laser focus [10], so the use of subpicosecond pulses turns off the potential, shifting the whole spectrum towards the lower-energy end, see for example [11].

2.2.2 Multiphoton Detachment of Electrons from Negative Ions

The calculation of the generalized n^{th} cross section that appears in equation 2.3 is difficult to calculate in a general case, but some aspects of negative ions make this calculation feasible:

i The external field varies slowly in comparison with the period of electron motion in the system. Therefore, the general adiabatic theory

([12], [3]) is applicable.

ii Due to the initial spread of the charge, the process of multiphoton detachment takes place when the electron is far away from the atomic particle.

Using these assumptions, a simple analytical solution for the detachment problem by a linearly polarized laser field was developed in the 90s by Gribakin et. al. [13]. The theory is valid when the number of photons n is large, but usually gives good results as soon as $n \geq 2$ [13].

The two features mentioned above greatly simplify the multiphoton detachment problem. Owing to (ii), the final state of the electron can be described by the Volkov [14] wave function, which takes into account the external field and neglects the atomic field. Moreover, the Volkov wave function describes explicitly the variation of the electron energy in the laser field. By using these hypotheses, G. Gribakin shows that the differential cross section of n-photon detachment of an electron from a negative ion by a linearly polarized light of frequency ω is [2]

$$\frac{d\sigma_n^{(lm)}}{d\Omega} = \frac{pA^2\omega(2l+1)}{4\pi\sqrt{2n\omega}}\frac{(l-|m|)!}{(l+|m|)!}|P_l^{|m|}(\sqrt{1+p_\perp^2})|^2\Big(\frac{\pi e}{nc\omega^2}\Big)^n \times \frac{\exp(p_\parallel^2/\omega)}{\sqrt{\kappa^2+p_\perp^2}}[1+(-1)^{n+l+m}\cos\Xi] \qquad (2.10)$$

where l is the orbital angular momentum and m is its projection of the initial electron state, κ is determined by the energy of the bound state $E_0 \equiv -\kappa^2/2$, A is the asymptotic parameter of the bound-state radial wavefunction $R(r) \simeq Ar^{-1}e^{-\kappa r}$, $p = \sqrt{2n\omega - \kappa^2}$ is the photoelectron momentum, $p_\parallel = p\cos\theta$ and $p_\perp = p\sin\theta$ are its components parallel and perpendicular to the field, $c \approx 137$ is the speed of light, $e = 2.71\ldots$, $P_l^{|m|}$ is the associated

[2] Atomic units are used from now on unless is explicitly specified otherwise in the form of *equation*[S.I.].

Legendre function, and

$$\Xi = (2n+1)\arctan\frac{p_\parallel}{\sqrt{\kappa^2+p_\perp^2}} + \frac{p_\parallel\sqrt{\kappa^2+p_\perp^2}}{\omega} \tag{2.11}$$

is the phase that determines the oscillatory behavior of the photoelectron angular distribution.

After the detachment from a closed-shell negative ion, the neutral atom is left in either of the two fine-structure states with the total angular momentum $j = l \pm \frac{1}{2}$. In this case the n-photon detachment cross section summed over the projections of the angular momentum is given by

$$\frac{d\sigma_n^{(j)}}{d\Omega} = \frac{2j+1}{2l+1}\sum_{m=-l}^{l}\frac{d\sigma_n^{(lm)}}{d\Omega} \tag{2.12}$$

where different values of κ and binding energies $|E_0|$ should be used for $j = l \pm \frac{1}{2}$, since the two sub-levels have different detachment thresholds. The main contribution to the sum in equation 2.12 comes from $m = 0$, since these orbitals are extended along the direction of the field.

By doing the sum over m (analytically) and integrating over the emission angle of the photoelectron, the result can be written as

$$\sigma_n^{(j)} = (2j+1)\frac{pA^2}{4\pi n}\Big(\frac{\pi e}{nc\omega^2}\Big)^n \exp(p^2/\omega)F_{nl}(p^2/\omega) \tag{2.13}$$

where F_{nl} is a dimensionless function, $\epsilon = p^2/\omega$

$$F_{nl}(\epsilon) = \int_{-1}^{1}\frac{e^{2\epsilon(x^2-1)}}{\sqrt{1-\epsilon x^2/n}}\Big\{P_l\Big(1+\frac{2\epsilon(1-x^2)}{n-\epsilon}\Big)$$
$$+ (-1)^{n+l}\cos\Big[(2n+1)\arctan\Big(\frac{x\sqrt{\epsilon}}{\sqrt{n-\epsilon x^2}}\Big) + 2x\sqrt{\epsilon(n-\epsilon x^2)}\Big]\Big\}dx \tag{2.14}$$

where P_l is the Legendre polynomial.

2.3 Tunnelling Ionization

2.3.1 Keldysh Theory

In a paper published in 1965, Keldysh [3] realized that an alternative to the multiphoton mechanism for ionization could occur under certain conditions. At low intensities compared with the atomic potential, the normal multiphoton excitation process for ionization via virtual intermediate states applies, see figure 2.4a). But if the incident field is strong enough and the frequency low enough so that the electron *feels* a static field, the field is able to distort the atomic potential to such an extent that a potential barrier is formed through which the electron can tunnel, figure 2.4b).

Clearly, as the field strength is increased the barrier becomes smaller and lower until eventually the ground state is no longer bound. For the ground state of hydrogen for low-frequency laser fields this occurs at $1.4{\cdot}10^{14} W/cm^2$. This is known as over-the-barrier ionization (OTBI), figure 2.4c). The critical field is obtained by equating the maximum distortion induced by the field in the atomic potential to the binding energy. The critical field for OTBI leads to a critical intensity

$$I_{OTBI}[W/cm^2] = \frac{\pi^2 c \epsilon^3 I_p^4}{2Z^2 e^6} = 4 \cdot 10^9 \big(I_p[eV]\big)^4 Z^4 \qquad \text{[S.I.]} \qquad (2.15)$$

where Z is the remaining charge state of the ionized atom or ion. For tunnel ionization of neutral F, $I_p = 17.4eV$ and $Z = 1$, so $I_{OTBI} = 3.6{\cdot}10^{14} W/cm^2$.

When the ionization rate is integrated over the laser pulse time, saturation of ionization occurs. This saturation intensity, I_{sat}, is a function of the pulse duration, and for long pulses, it can be lower than the I_{OTBI}. This means that all the target atoms will be ionized before the I_{OTBI} is reached. On the other hand, the signal still increases when the intensity is increased but at a slower rate, as the volume of significant ionization in the laser focus grows as the wings of the focal region are yet to be saturated.

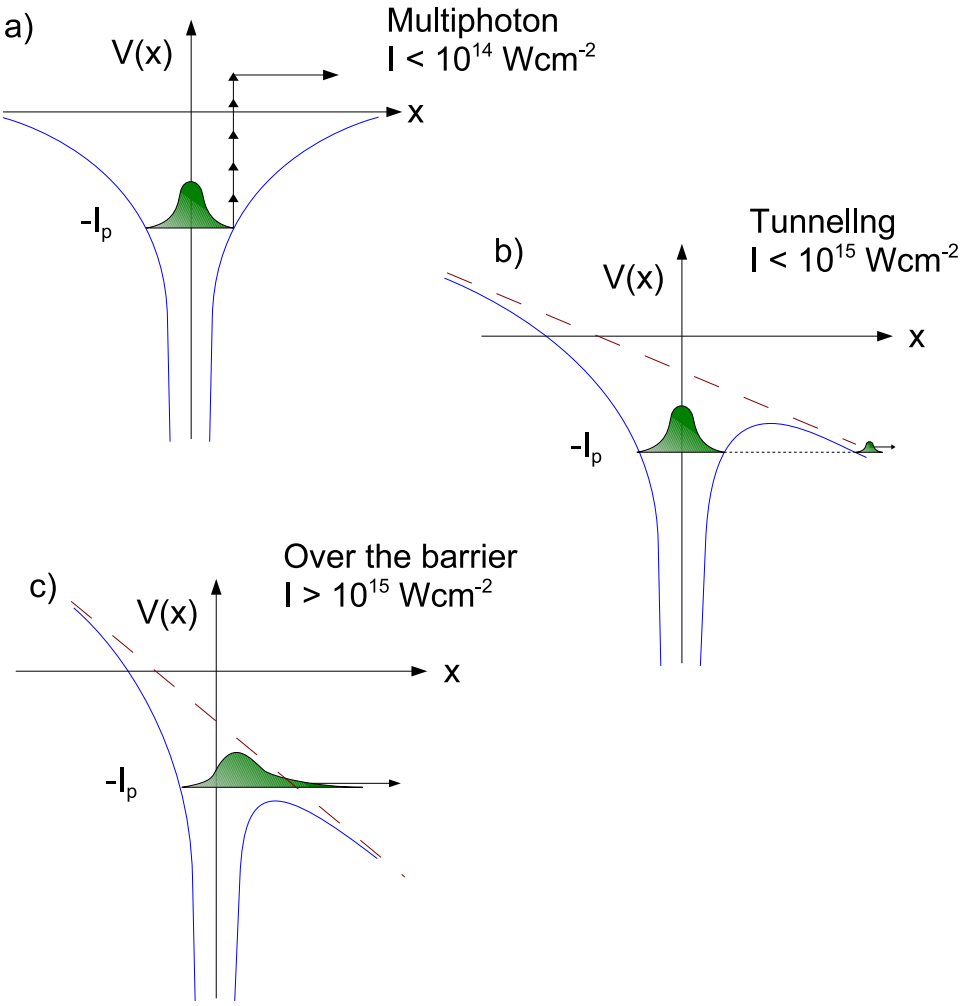

Figure 2.4: Schematic diagram showing the three possible mechanisms for ionization. a)At intensities lower than $\sim 10^{14} W/cm^2$, multiphoton ionization dominates. b)As the intensity is increased the atomic potential is distorted and tunnelling ionization is possible. c)At even higher intensities, the barrier is suppressed to such an extent that the initial wavepacket is free to escape from the atomic potential (over barrier ionization).

2.3.1.1 Keldysh Parameter

As mentioned in the introduction, a governing quantity of above-threshold ionization processes is the Keldysh parameter γ,

$$\gamma = \frac{\omega_{laser}}{\omega_{tunnel}} = \sqrt{\frac{I_p}{2U_p}} \tag{2.16}$$

where I_p is the ionization potential, and U_P is the ponderomotive energy of the electron in atomic units. The Keldysh parameter is said to characterize the degree of adiabaticity of the motion through the barrier. If $\gamma \ll 1$ then tunnelling dynamics will dominate, reducing the calculation of the ionization probability to average the probabilities of ionization in a constant field over a period of the external field. On the other, if $\gamma \gg 1$, then multiphoton dynamics will be most significant.

2.3.2 Tunnel Ionization in an Alternating Electromagnetic Field

It is possible to find a quasiclassical solution of the problem of ionization of an atom by an alternating field only when the following circumstances are valid[3]:

i the cases of not too high frequencies ω and field strength F for which the ionization occurs slowly in comparison with atomic times

ii when the wavelength of the light is much larger that the radius of the atom, so that the electric field can be treated as uniform (dipole approximation).

iii when the speed of the electron is nonrelativistic, so the effect of the magnetic field of the wave can be neglected.

With these conditions, the calculation of the atomic ionization rate in the tunnelling regime reduces to averaging the rate in a constant field over a period of the external field in the low-frequency limit case of an alternating electromagnetic field

$$\omega \ll \omega_t \ ; \ \omega_t = 1/\tau_t \tag{2.17}$$

where τ_t is the tunnelling time.

[3]These conditions apply for section 2.4 as well.

So in the case of an external static electromagnetic field, $\mathscr{E}$, linearly polarized, the probability of ionization per unit time from a state with energy E_0, and quantum numbers n,l,m is described by the expression[15]:

$$w_{stat}(\mathscr{E}) = |C_{nl}|^2 \; E_0 \; f(l,m) \cdot \left(\frac{2\mathscr{E}_0}{\mathscr{E}}\right)^{2n-|m|-1} \exp\left\{-\frac{2\mathscr{E}_0}{3\mathscr{E}}\right\} \tag{2.18}$$

where

$$\mathscr{E}_0 = (2E_0)^{3/2}$$

$$f(l,m) = \frac{(2l+1)(l+|m|)!}{2^{|m|}(|m|)!(l-|m|)!}$$

The expression for the dimensionless constant $|C_{nl}|^2$ is known only for the hydrogen atom [16]:

$$|C_{nl}|^2 = \frac{2^{2n}}{n(n+1)!(n-l-1)!} \tag{2.19}$$

This formula can be adapted for an arbitrary atom by replacing the principal quantum number of the hydrogen atom n by the effective quantum number $n^* = Z(2E)^{-1/2}$ and l by the effective orbital quantum number l^*, which is $l^* = 0$ for $l \ll n$ or $l^* = n^* - 1$ otherwise. Applying the asymptotic Stirling formula to avoid the difficulty of performing factorials on non-integer number, we get [4]

$$|C_{n^*l^*}|^2 = \frac{1}{2\pi n^*}\left(\frac{4e^2}{n^{*2}-l^{*2}}\right)^{n^*}\left(\frac{n^*-l^*}{n^*+l^*}\right)^{l^*+1/2} \tag{2.20}$$

where e=2.718...

Finally, if we average equation 2.18 over a period of the external field, the probability of ionization in a linear polarized field is obtained

$$w_{linear}(\mathscr{E}) = \left(\frac{3\mathscr{E}}{\pi\mathscr{E}_0}\right)^{1/2} w_{stat}(\mathscr{E}) \tag{2.21}$$

where the only change is in the coefficient that multiplies the exponential, which remains unchanged. This means that in the adiabatic case the ionization of an atom occurs mainly at the times when the field reaches its maximum values.

[4]The expression for $|C^2_{n\ l}|^2$ in Ammosovo et. al. [17] contains an inaccuracy which is corrected in [18]

For the case of a circularly polarized light the amplitude that the atom feels is constant, so:

$$w_{circular}(\mathscr{E}) = w_{stat}(\mathscr{E}) \tag{2.22}$$

The equation 2.21 is known in the literature as ADK rate, but it has to be said that it can be found in an earlier paper by Perelomov [15], in which they go further and propose an analytical theory that is valid for any value of γ, as we will see in the next section.

2.4 PPT theory

In the case where $\omega \gg \omega_t$, the adiabatic approximation does not apply, and to find the probability of ionization, w, one must solve the time-dependent Schrödinger equation. In a series of papers Perelomov , Popov and Terent'ev [15][16], studied in detail the interaction of atomic systems with laser light. They solve the problem of ionization of an atomic level (bound by a short-range force) by a linear, circular and elliptically polarized electromagnetic field.

The assumptions that they take during the mathematical deduction are:

i the mean time of ionization is much larger than atomic times.

ii the field is turned on adiabatically.

iii $\omega \ll \omega_0$, where ω_0 is the binding energy of the electron, and

iv the wave function of the final electron can be replaced by the wave function of the bound state for the free atom if $V(r)$ falls off more rapidly than $1/r$ for $r \to \infty$.

Due to the last point, the equations deduced in the next two sections, are valid for the case of photodetachment:

$$A^- + n\hbar\omega \to A + e^-$$

A correction for the Coulomb interaction is explained in section 2.4.3

I will not repeat here the full derivation of the final equation, but I would highlight the main points. They start by considering the motion of a particle in a zero-range potential $V(\mathbf{r}) = \kappa\delta(\mathbf{r})$ where there is just one bound state with energy $\omega_0 = \kappa^2/2$. The Schrödinger equation for an alternating field can be written as:

$$i\frac{\partial}{\partial t}\Psi(\mathbf{r},t) = \{-\nabla^2 - \mathbf{r}\delta(\mathbf{r}) - F(t)\mathbf{r}\}\Psi(\mathbf{r},t) \tag{2.23}$$

where $F(t) = F\cos(\omega t)$. Equation 2.23 can be reduced to an integral equation, where the formal solution can be written in terms of the Green's function formalism. Then they calculate the associated quantum-mechanical current using that:

$$j(\mathbf{r},t) = \frac{i}{2}(\Psi\nabla\Psi^\star - \Psi^\star\nabla\Psi) \tag{2.24}$$

By averaging $j(\mathbf{r},t)$ over a period of the external field and multiplying by two (the flux of electrons goes in both directions from the "atom"), they find the probability of ionization, $w(F,\omega)$.

2.4.1 Case of Linear Polarized Light

Following the steps mentioned above, they arrive to an expression for the ionization in the field of a plane-polarized wave ($\epsilon = 0$), from a level with binding energy E_0, orbital angular momentum l, and projection m in the direction of the field, given by:

$$w(\omega,F)_{linear} = E_0\left(\frac{3}{2\pi}\right)^{1/2}|C_{n^*,l^*}|\ f(l,m)\left(\frac{F\sqrt{1+\gamma^2}}{2F_0}\right)^{|m|+3/2} \times A_m(\omega,\gamma)\ \exp\left\{\frac{-2F_0}{3F}g(\gamma)\right\} \tag{2.25}$$

where:

$$A_m(\omega,\gamma) = \frac{4}{\sqrt{3\pi}}\ \frac{1}{|m|!}\ \frac{\gamma^2}{1+\gamma^2}\sum_{k\geq\nu}^{\infty}\left[e^{-\alpha\cdot(k-\nu)} f_m\left(\sqrt{\beta\cdot(k-\nu)}\ \right)\right]$$

$$f_m(x) = \frac{x^{2|m|+1}}{2}\ \int_0^1 \frac{e^{-x^2 t}t^{|m|}}{\sqrt{1-t}}dt$$

$$\beta(\gamma) = \frac{2\gamma}{\sqrt{1+\gamma^2}}$$

$$\alpha(\gamma) = 2\left[\sinh^{-1}(\gamma) - \frac{\beta}{2}\right]$$

$$g(\gamma) = \frac{3}{2\gamma}\ \left[\left(1+\frac{1}{2\gamma^2}\right)\sinh^{-1}(\gamma) - \frac{\sqrt{1+\gamma^2}}{2\gamma}\right]$$

$$\nu = \frac{E_0}{\omega}\left(1+\frac{1}{2\gamma^2}\right)$$

$$k = \left\langle \frac{E_0}{\omega} + 1 \right\rangle + S$$

Where S=0, 1, 2, 3, ..., and the symbols $\langle\ \rangle$ indicate the integer part of the number inside, the ω is the energy of one photon, $F_0 = (2E_0)^{3/2}$, Z is the charge of the resulting ion or atomic residue and F is the amplitude of the external field.

Let us discuss the physical meaning of the formula 2.25. As already pointed out by Keldysh[3], *the probability of ionization is the sum of the probabilities of many-photon processes*, each of which corresponds to the absorption of a whole number ($n \geq \nu$) of quanta.

The next step is to see how the equation 2.25 behaves for the limits $\gamma \ll 1$ and $\gamma \gg 1$. For the case of high frequencies ($\gamma \gg 1$), we can write $(F/2F_0)(1+\gamma^2)^{1/2} \rightarrow \omega/4\omega_0$ and the function $A_m(\omega,\gamma)$ reduces to the first term of the series. In this frequency range, the coefficient of the exponentials is a rapidly varying function, with singularities at the thresholds for absorption of n quanta, which is a clear indication that the multiphoton process is the dominant in this regime.

In the opposite case $\gamma \ll 1$, the factor $A_m(\omega,\gamma)$ goes to 1 so the multi-

photon nature vanish with it. Note that 2.25 transforms to 2.21, as expected.

2.4.2 Case of Circular Polarized Light

A circular polarized field can be expressed as

$$F(t) = F\Big(\hat{e}_x \cos(\omega t) + \hat{e}_y \sin(\omega t)\Big) \tag{2.26}$$

The difference from the linear case is that now the threshold for ionization (the minimum number of quanta) is $\nu = (\omega_0/\omega)(1 + 1/\gamma^2)$, due to the fact that the mean kinetic energy of the electron in the field of the circularly polarized wave, is twice its mean energy in the field of the plane-polarized wave. Therefore, following an equivalent procedure to the linear case, it is possible to derive the following formula for the total probability of ionization of an s level by a circularly polarized wave

$$w_{circular}(F,\omega) = E_0 \ |C_{n^*,l^*}| \ \frac{F}{2F_0} \ h(\gamma) \ \exp\left\{ -\frac{2F_0}{3F} g_c(\gamma) \right\} \tag{2.27}$$

where

$$g_c(\gamma) = \tfrac{3t_0}{\gamma^2(1-t_0^2)} \left[(1+\gamma^2)(1+\tfrac{t_0^2}{\gamma^2}) \right]^{1/2}$$

$$h(\gamma) = (1+t_0) \left[\tfrac{(1+\gamma^2)(1+t_0^2)}{(1+t_0^2/\gamma^2)(1+t_0^2+2t_0^2/\gamma^2)} \right]^{1/2}$$

$$\tanh^{-1}\left\{ \left(\tfrac{t_0^2+\gamma^2}{1+\gamma^2} \right)^{1/2} \right\} = \tfrac{1}{1-t_0} \left(\tfrac{t_0^2+\gamma^2}{1+\gamma^2} \right)^{1/2}$$

There are always many values of n which contribute to the probability of ionization $w_{circular}(F,\omega)$, therefore the threshold singularities in the coefficient $h(\gamma)$, unlike those in the case of linear polarization, merge together and disappear. In the limit for $\gamma \to 0$, $g_c(\gamma) \to 1 - \gamma^2/15$ and $h(\gamma) \to 1$, so $w_c(F,\omega)$ goes over into $w_{stat}(F)$, as it should do.

2.4.3 Coulomb Correction

In order to deal with the Coulomb interaction, Perelomov and coworkers assume that the Coulomb potential is small when $\kappa r \gg 1$ ($E_0 = \kappa^2/2$), so

its influence on the trajectory of the sub-barrier motion is also small (in determining this trajectory they took into account only the external field $F(t)$). So under this condition, the ionization probability with allowance for the Coulomb correction is

$$w(F,\omega,\epsilon) = \left[\frac{2F_0}{F}C(\gamma,\epsilon)\right]^{2\lambda} w_{s.r}(F,\omega,\epsilon) \tag{2.28}$$

where ϵ is the polarization state, and $w_{s.r}(F,\omega,\epsilon)$ are the short range potential equations, that is to say without coulomb correction (eq. 2.25 for $\epsilon = 0$; eq. 2.27 for $\epsilon = 1$), and

$$C(\gamma,\epsilon) = \tfrac{\tau_0}{2\gamma}\exp\left\{\int_0^{\tau_0}\left[\tfrac{\gamma}{F(\gamma,\epsilon)} - \tfrac{1}{\tau_0-\tau}\right]dt\right\}$$

$$F(\gamma,\epsilon) = \left[(\cosh\tau_0 - \cosh\tau)^2 - \epsilon^2\tau^2\left(\tfrac{\sinh\tau_0}{\tau_0} - \tfrac{\sinh\tau}{\tau}\right)^2\right]^{1/2}$$

$$\sinh^2\tau_0 - \epsilon^2\left(\cosh\tau_0 - \tfrac{\sinh\tau_0}{\tau_0}\right)^2 = \gamma^2$$

where t_0 ($t_0 = \tau_0/\omega$) has the meaning of the total time of electron motion under the barrier. A good parameter for determining if the equation 2.28 is applicable is if

$$n^*\left(\frac{\omega}{2E_0}\right)^2\frac{F_0}{F} \;=\; \frac{Z}{F}\frac{\omega^2}{2E_0} \ll 1 \tag{2.29}$$

where Z is the residual atomic charge, F is the electrical field strength, ω is the laser's frequency and E_0 is the ionization potential.

If we use the last equation for our system [Z=1, Intensity=$10^{10}W/cm^2$, and E_0=17.4228eV (fluorine)], we find that the left hand side of the equation 2.29 has a numerical value of 0.12. That indicates that we are working with enough strong fields for the equation 2.28 be valid.

2.5 Numerical Integration Techniques

At intensities less than $10^{13}W/cm^2$ perturbation theory is adequate to describe the experimental observations. Above these intensities, non-perturbative

behaviour starts to appear, making non-perturbative approaches necessary. The difficulty comes from the fact that analytic solutions do not exist for most systems, and approximations have to be taken. The main neglected effects when modelling this kind of phenomena, are:

i Ponderomotive effects: once ionized the electron wavepacket has still to leave the laser focus. In doing so, it will experience ponderomotive acceleration from the spatial gradient of the intensity.

ii No sample or laser is perfectly homogenous for any realistic pulse duration, so both spatial and temporal averaging have a strong effect.

Despite neglecting these important points, single-atom approaches have been extremely successful in describing experimental results and predicting new effects. Notice that the ponderomotive effects are not significant for ultrashort pulses (femtosecond lasers).
Most semi-analytic non-perturbative approaches work quite well, but become increasingly difficult and unreliable as the laser intensity is increased. The natural alternative to these methods is the direct integration of the Schrödinger equation.

2.5.1 Main Techniques

2.5.1.1 Floquet theory

Use of Floquet theory involves solving the dynamics of the molecule in the strong field as a time-independent eigenvalue problem. This approach assumes that the electric field is turned on abruptly at a time $t = 0$ and is maintained indefinitely. The time dependent Schrödinger equation (TDSE) is solved to produce an infinite set of coupled Floquet equations. The results of this calculation provide what are termed quasi-energy states of the laser-atom/molecule system. This model works well for a moderate intensity laser field with long pulses of the order of hundreds of optical cycles.

2.5.1.2 R-matrix-Floquet approach

Another approach is the R-matrix-Floquet [19] which involves transforming the time-dependent equations into a set of time-independent equations, the so-called Floquet-Fourier transformation, which then can be solved by the well-established R-matrix method, developed at Theoretical and Computational Physics Research Division of QUB.

The R-matrix approach was originally developed to describe electron scattering processes for atoms. Although the theory behind the theoretical determination of scattering cross sections is well known, the description of the interactions between all electrons requires sophisticated computer codes to describe the repulsion between the electrons in detail. The main advantage that the R-matrix-Floquet approach has over other approaches is that it can be applied in principle to any atomic system.

2.5.1.3 Direct solution of TDSE

A natural alternative is the direct integration of the Schrödinger equation, which seems very attractive, given its numerous advantages: no explicit assumptions are made and solutions can, at least in principle, be found in all regimes of intensity and frequency. Besides, there is no restriction on the type of laser pulse shape which used. The only assumptions made are those implicit in solving the standard Schrödinder equation: a non-relativistic, spinless system in which dipole transitions dominate.

In spite of all its advantages, the large and intensive computational codes needed made it unviable to implement for many years. It was just in the lates 80's when the advances on computer technology made possible an extensive use of this technique. Still, the restriction on the size of the temporal steps (used in all integration algorithms) make this a forbidden task, unless some approximation is taken, the main ones being: reducing the problem to a full one-dimensional calculation, and approximate three-dimensional

calculations. Numerous methods exist. A recent discussion about it can be found in Taylor et. al. [20]

2.5.1.4 Classical Monte Carlo simulations

Another way to describe the interaction of atoms with strong laser fields is integrating the Lorentz classical equation for the atomic electron moving in the combined Coulomb and laser fields. The initial task here is to compute the initial classical electron distribution in phase-space prior to the interaction with the laser field. This procedure uses a Monte Carlo simulation and is already well established (e.g. [21]).

2.6 The Recollision Picture.

In the 90's, experiments were performed where enhanced production of doubly charged ions were observed with yields that did not follow a kinetic description based upon sequential rates. In figure 2.5 it is possible to see experimental data where a $160 \pm 30fs$, $780nm$ light pulse was focused into vacuum chamber ($10^{-10}mbar$) filled with He gas, together with theoretical calculations performed with ADK and single active electron calculations. The differences are easily noticed. While still there is a good agreement with ADK and single active electron (SAE) calculations for very high intensities, the observed "shoulder" is not reproduced by any of them, neither qualitatively nor quantitatively, see figure 2.5.

In order to explain this experimental observations, two distinct mechanism were proposed. On the one hand Fittinghoff [23] proposed the "shake-off" mechanism, where one electron is rapidly removed by the laser field and as a consequence, the remaining electron cannot adiabatically readjust to the ionic potential and is instantaneously "shaken off" into the continuum. This mechanism is known to dominated double ionization of helium after

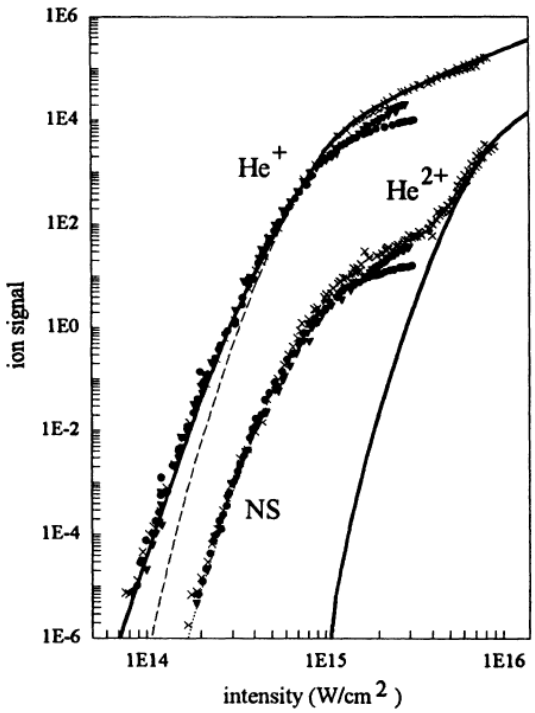

Figure 2.5: Experimentally measured single and double ionization yields in helium. Solid line: SAE model; Dashed line: ADK model (from Walker[22]).

absorption of single photons with energies beyond 1keV. [24].

Corkum et. al. [25]proposed an alternative mechanism based on electron-electron inelastic re-scattering known as a "recollision" model, where the second electron is ionized in a collision when the the first electron hits the parent ion after free propagation in the external laser field. In two milestone papers in the field, R. Moshammer [26] and T. Weber [27] using cold target recoil-ion momentum spectroscopy (COLTRIM) measured the momentum distributions for multiply charge ions (Ne and He, respectively). With that data, they showed that mechanisms based on an instantaneous release of two (or more) electrons (such as "shake-off"), can be ruled out as a dominant contribution to non-sequential double ionization in intense light pulse. Only the kinematics of the rescattering mechanism was found in accordance with the experimental data.

The recollision picture developed by Corkum [25], Kulander [28], Schafer [29] and others builds on earlier "simpleman" picture of a quivering electron. It is essentially a three step model, starting when an electron is liberated from its parent atom. At the usual intensities for tunnel ionization, the Coulomb potential of the ionic core is neglected and the electron is assumed to feel just the electric field of the laser that initially drives the electron away from the ionic core. This movement governed by the Lorentz force is considered the second step. At a later time, the phase of the laser field reverses and the electron is then accelerated back towards the core. In the last step, the electron re-encounters the core where can recombine, returning to its initial ground state by radiating a photon or can lead to a further ionization of the atom by electron impact.

It is possible to calculate the maximum energy that the returning electron can carry. If the tunnelling process is such that the electron is "born" at a distance from the core so that the motion is dominated by the laser field, then the quiver motion may be treated entirely classically. The electron displacement, x, from the core obeys the Newtonian equations of motion, at least in a classical approximation,

$$\begin{aligned} \frac{d^2x}{dt^2} &= \frac{eE_0}{m}\cos(w_0 t) \\ \frac{dx}{dt} &= v = \frac{eE_0}{mw_0}\sin(w_0 t) + v_i \\ x &= -\frac{eE_0}{mw_0^2}\cos(w_0 t) + v_i + x_i \end{aligned} \tag{2.30}$$

where v_i and x_i are the initial velocity and position. If we assume that at the moment of ionization, $t = t_0$, that $v(t = t_0) = x(t = t_0) = 0$, then:

$$\begin{aligned} v(t) &= \frac{eE_0}{mw_0}\big[\sin(w_0 t) - \sin(w_0 t_0)\big] \\ x(t) &= -\frac{eE_0}{mw_0^2}\big[\cos(w_0 t) + w_0 t\sin(w_0 t_0) - \cos(w_0 t_0) - w_0 t_0\sin(w_0 t_0)\big] \end{aligned} \tag{2.31}$$

If we call t_r the time when the electron comes back to the core, the equation $x(t = t_r) = 0$ will give us a relationship between t_0 and t_r. So now we can write the velocity at which the electron impacts the atom (v_r) as a function just of the initial t_0. If we determine the maximum of $v_r(t_0)$, we have found the maximum re-collision kinetic energy. This can be determined numerically to be $3.17U_p$ at a phase $w_0t = 17°$ or $197°$. This calculation, being done in 1D, assumes that the electron interacts with the core in the first return.

2.6.1 Coulomb Focusing

The role of the Coulomb potential in the recollision model can be influential. This is one of the main differences between negative ions and atoms or positive ions. In the first case the initially ionized electron (by tunnelling or by MPI) sees a neutral[5] atom, while in the second case, the electron feels a Coulomb potential.

For small impact parameters, the electron interacts strongly with the ion to collisionally excite or ionize the bound electron during its first return. However, only a small fraction of the trajectories with low initial transverse velocities pass close enough to the nucleus to contribute to double ionization (see figure 2.6b, solid line). On the other hand, electrons with large impact parameters will miss the nucleus at the first return. However, Thomas et al[30] showed that, due to small deflections during each encounter, these trajectories can be focused into the double ionization cross section after multiple returns (see figure 2.6b, dotted line). In quantum-like terms, the part of the wave function that contributes to non-sequential double ion-

[5] *Nearly* neutral atom, remember the dipole moment induced by the extra electron discussed in section 1.6

ization is considerably increased. In another calculation [30], it is shown how the non-sequential ionization rate is increased by a factor of 30 due to higher returns, for intensities in the tunnelling regime, see figure 2.7. The main contribution comes from the region close to the peak of the electric peak, where tunnel ionization is most efficient and electrons are born with low drift velocity so that higher-order returns are possible. Another impor-

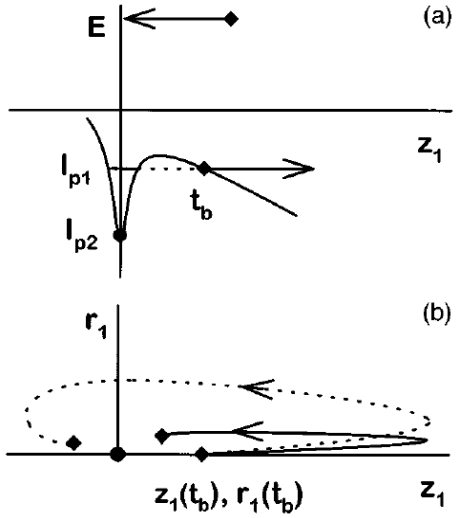

Figure 2.6: Example of evolution of a two-electron atom or ion in a strong laser field. The diamond represents the tunnel ionized electron; the circle corresponds to the bound electron. a)Energy evolution of the first e^-, ionized at time t_b. b)Space evolution of the tunnelled e^-. Solid line: small impact parameters; dotted line: large impact parameters.

tant contribution to non-sequential ionization comes from the process where the returning electron has not enough energy to ionize the bound electron, but still has enough to promote it to an excited state. This excited state would be bound at the moment of the *promotion*, the excited electron can be ionized at the time of maximum barrier suppression.

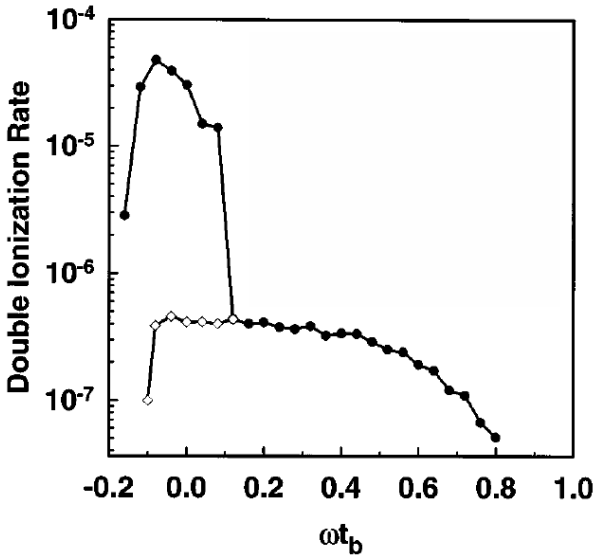

Figure 2.7: Numerically calculated non-sequential ionization rate for double ionization in He vs the phase of the laser field ωt_b at the moment of tunnelling ionization of the first e^-. Open diamonds show the contribution from first recollision ionization only (from [30]).

2.7 Negative Ions

Multi-photon studies have been an stimulating area of the negative-ion studies during the last 15 years. Even though the first two-photon detachment experiment was performed in 1965 [31], it was not untiil before the end of the 1980s and the beginning of the 1990s that multi-photon experiments with negative atomic ions really started. These were strong laser field studies and based on absorption of two or more photons of the same frequency (see for example [32]).

2.7.1 Non-resonant Multi-photon Detachment

Non-resonant multi-photon detachment provide conditions which are very attractive from the theoretical point of view, due to the possibility of performing studies without the influence of excited states and that the emitted electrons would not be under the influence of the Coulomb field. During the first years of these studies the focus was on measurements of total multi-

photon detachment cross sections, but it was often difficult to determine the cross section sufficiently accurately to allow for a clear distinction between existing theories [32].

Three publications appeared within a few weeks in 1991 all reporting the observation of excess photon absorption in either negative F[33], Cl[34], or Au[35]. In all three experiments it was possible to reach the same qualitative conclusion, that non-resonant excess photon absorption is an important process in a negative atomic ion at laser intensities of the order $10^{12} W/cm^2$. In the negative Au ion experiment, two 1.165eV photons from a Nd:YAG laser were sufficient to exceed the detachment threshold with about 20meV. The first order excess-photon process (three photon absorption), and the second order excess-photon process (four photon absorption) were estimated to represent 5% and 0.6%, respectively, of the total electron yield at an irradiation intensity of $3 \cdot 10^{12} W/cm^2$.

In the F^- experiment the angular distributions of excess-electron detached electrons were measured. Figure 2.8 shows the angular distribution of four-photon detached electrons from F^- ion at the wavelength of 1064nm. Three photons are sufficient to detach the F^-, so the shape of the angular distribution gives a precise signature of excess-photon detachment, providing a precise challenge for theoriticians[36], trying to reproduce the experimental results.

2.7.2 Resonant Multi-photon Detachment

The exploration of resonant multi-photon detachment as an experimental method to study negative ions was pioneered by Haugen and co-workers ([37], [38], [39]). Resonant phenomena can occur in negative ions in several ways. The first experiments took advantage of the resonances located above the detachment limit, such as the doubly excited states in the heavier negative ions of the alkalis ([40],[41]). Excess photon detachment from

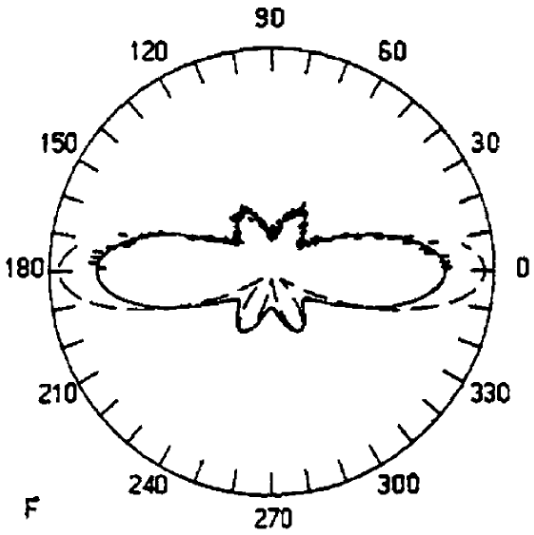

Figure 2.8: Angular distribution of four-photon detached electrons from F^-, at $\lambda = 1064nm$. Three is the minimum number of photons for photodetachment. The qualitative correspondence with the plane-wave approximation (dashed line) is a precise signature of excess-photon detachment.

the ground state of the Cs^- ion is strongly enhanced when the first photon reaches an energy corresponding to the $Cs^-(6p_{1/2}7s)$ state, where the cross section for single-photon detachment reaches a minimum, caused by interference between the excited Cs^- state and the continuum [38]. This minimum facilitates absorption of additional photons by suppressing the depletion of the ground state during the rise time of the laser pulse. Absorption of an additional photon by the negative ion will lead to population of an excited Cs atom state, which subsequently can be ionized by absorption of one additional photon. The $Cs^- \rightarrow Cs^+$ double ionization process was due to sequential electron removal.

Recently, in our laboratory [42] double ionization of atomic negative ions (Al^-, Ag^-, I^-, C^-) in an intense laser field ($I \sim 10^{14} W/cm^2$) was studied. The yields of positive ions as a function of intensity were not consistent with sequential electron removal. Although the laser pulses applied were very long

by modern standards, and tend to produce sequential ionization in atoms, the positive ion yields from the negative ions did not depend predictably on the ionization potentials. A possible explanation would be the existence of an alternative mechanism enhancing double ionization at low laser intensity. This mechanism may involve resonant enhancement via double or multiply excited states.

Excess-photon absorption via an autodetaching state was further developed, combining low laser intensities and resonant ionization spectroscopy (RIS) [36] to obtain spectroscopic information about autodetaching states. The high sensitivity of the RIS detection method allows the observation of the resonant excess photon absorption process at much lower laser intensities (four or five orders of magnitude less) than applied in the experiment described above. Thus, it is possible to avoid the influence of saturation effects due to depletion of the negative-ion target, an effect which otherwise would influence both the position and the width of the excess photon absorption signal even at very low rates. By means of this technique, spectroscopic information was obtained for autodetaching states in negative ions of Sr and Ba [36].

Other techniques exist involving three [43] or even four [44] different wavelengths. In three frequencies experiments, the first nanosecond pulse is used to explore the detachment cross section. The second is a probe pulse, with a small time delay ($\sim 10ns$) used to probe the remaining population of the ground state levels of the negative ion to the neutral atom. The population of the neutral atom can then be measured separately using the RIS technique, with the third laser.

Another different situation occurs when the resonant multi-photon de-

tachment takes place below the detachment limit. Several ions exhibit fine structure in their ground state with both the fine structure levels being located below the detachment limit. Using this method it is possible to obtain structural information about the negative ions [45].

2.7.3 The Recollision Model for Negative Ions

In negative ions the rescattering mechanism is governed by different parameters as described in section 2.6. A proper description of the spatial distribution of the wave packet is defined by the wave function of the initial state. In negative ions, the initial size of the wave packet is larger, as shown in section 1.6.1, resulting in a smaller spread of the electron density distribution at the moment when the electron returns back to the core. On another hand, the scattering amplitude is smaller due the short-range character of the core potential and the absence of the coulomb focusing.

In a recent work, Kiyan [46] and co workers have studied the angular distributions of photo-electrons coming from the interaction of a 250fs laser pulse ($\lambda = 2.15\mu m$) with a 3keV H^- beam. In this work, they show that the angular distribution and the energy spectrum are well described by the multiphoton theory developed by Gribakin et. al. [13], see figure 2.9. In this theory there is interference in the outgoing wave-packet, but the rescattering is not included.

The same group performed a similar experiment [47], but this time using a 138fs laser pulse ($\lambda = 1.8\mu m$) on a 3keV F^- beam ($\sim 150nA$ and a background pressure of $2{\cdot}10^{-10}mbar$). They tried to fit their experimental energy distribution of photoelectrons emitted along the laser polarization axis to calculations with [48] and without [13] the rescattering effect taken into account, see figure 2.10. We can see how the theory without rescattering fails to predict the production of high energy electrons, even when it describes it very well for low energies. The theory that takes into account the rescatter-

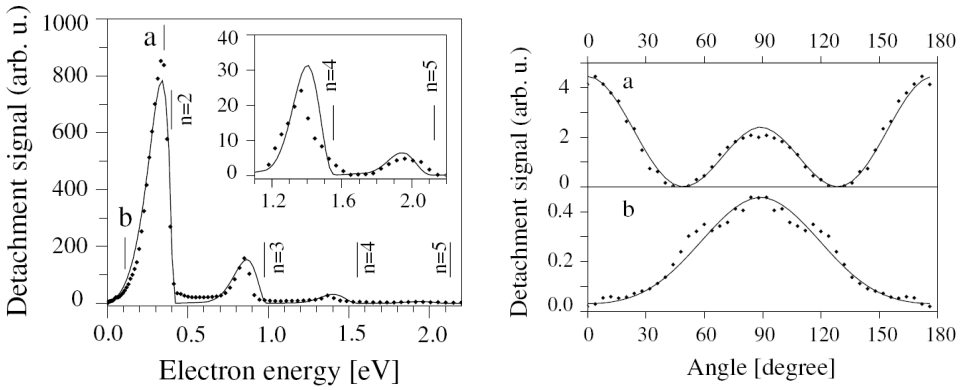

Figure 2.9: Dots: experimental data; solid curve: theoretical results. Left: Energy spectrum integrated over the angle θ. Right: Angular distributions of photo-electrons in the lowest two-photon detachment channel at energies labelled a and b in the left diagram. a)$I = 1.3 \cdot 10^{11} W/cm^2$; b)$I = 6.5 \cdot 10^{11} W/cm^2$. Experimental and theoretical results are normalized to each other.

ing, predicts an enhancement of the electrons in the high energy region, but remains nearly two orders of magnitude lower than the measured electron yield. Clearly the role of the rescattering in negative ions remains unclear.

2.8 Ion Beam Sources

2.8.1 Sources of Positive Ions

2.8.1.1 Penning Type

This type of ion sources operates on the principle of a Penning discharge. The ions are produced by initially introducing neutral gas via a fine control needle valve (see figure 2.11), to a typical fill pressure of $\sim 10^{-6} mbar$. Application of a potential difference across the hollow cylindrical anode and cathode results in an ionizing discharge ($\sim 1mA$) whereby electrons may be stripped from the neutral gas. These electrons are then subjected to the forces within the electric field and are therefore accelerated back and forth along the length of the anode. As a result of this movement, the electrons may collide with the

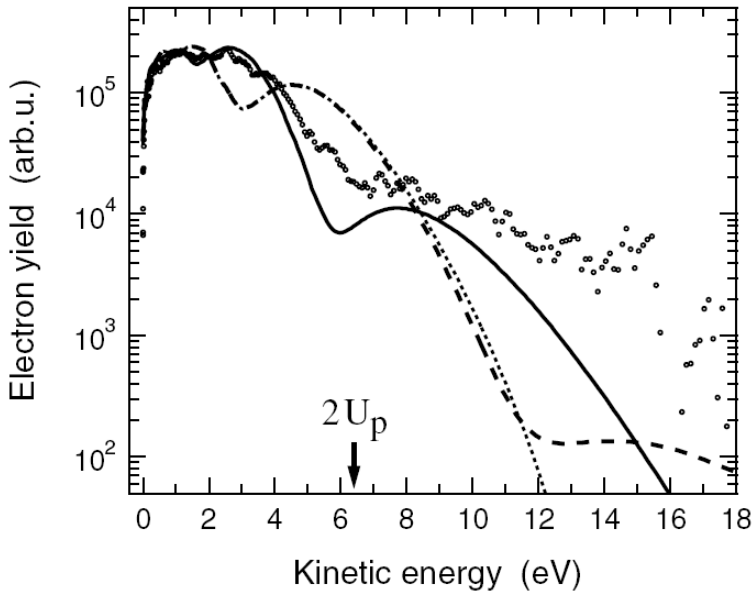

Figure 2.10: Energy distribution of photoelectrons emitted along the laser polarization axis. Dots: experimental data; solid line: calculations for $l = 1$ (without rescattering); dashed line: calculations for $l = 0$ without taking into account rescattering; dotted line: calculations for $l = 0$ taking into account rescattering.

neutral gas resulting in a further ionization (electron impact ionization). The probability of ionisation is enhanced by the presence of an axial magnetic field($\sim 0.1T$), which causes the ionised electrons to follow a helical path, hence increasing the likehood of collision and subsequent ionisation.

2.8.1.2 ECR Ion Source

Energetic electrons rotate in a magnetic field, B, with a frequency defined by the relation $w = eB/m$. In a box immersed in an arbitrary magnetic field there can exist a surface where the above relationship holds. If radio frequency power of this frequency is injected into the box, plasma electrons crossing this surface will, in general, be heated and can be used for ionisation of the plasma. The plasma density can therefore increase up to a value which is believed to be limited when the plasma frequency, which is a function of the density, exceeds the RF frequency. With adequate confinement of the

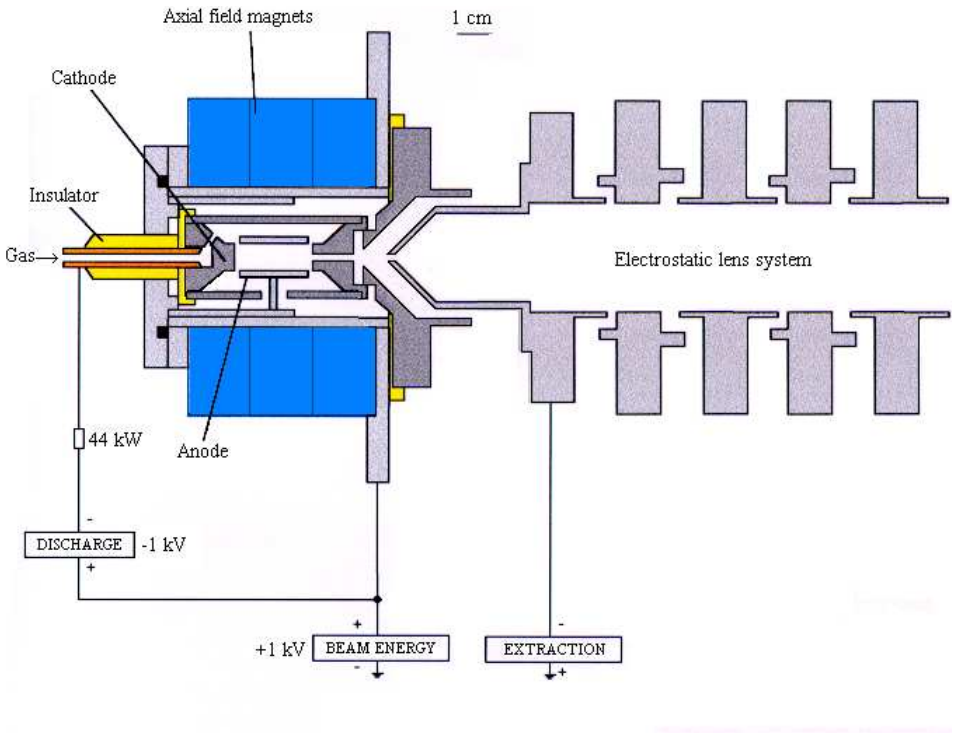

Figure 2.11: Schematic of a typical Penning discharge source and adjacent extraction lenses. (From P. McKenna [49])

plasma and the use of microwave frequencies, high electron temperatures can be attained enabling multi-charged ion production.

The Electron Cyclotron Resonance Ion Source(ECRIS) [50] makes use of this effect using microwave frequencies. Longitudinal confinement is achieved by Helmholtz coils configured to give a minimum B field configuration and radial confinement by powerful permanent magnet multipoles. Plasma densities greater than $10^{12} cm^{-3}$ can be attained. Normally an ECRIS gives a better performance when used in the pulsed mode as opposed to dc operation. It is possible to adjust a pulsed source in such a way that when the RF heating power is turned off, a large peak of highly charged ions appears. This effect, known as "afterglow" is believed to be due to a rapid loss of plasma electrons and the deconfinement of positive ions [51].

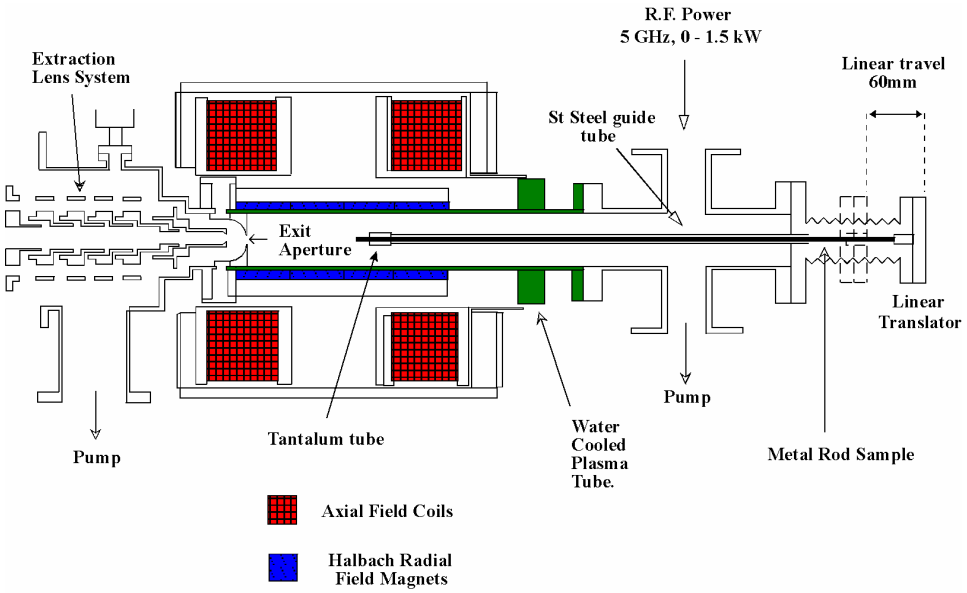

Figure 2.12: Schematic of a ECR ion source, including oven for metal ion production. (From P. McKenna [49])

2.8.2 Sources of Negative Ions

The technology of the negative ions sources started to develope at later times than the positive counterparts. Negative ion sources were developed for the use of negative ions beams in the injection heating of tokomak plasmas and in accelerator technology. In tandem accelerators, negative ions are used to multiply the energy of the accelerated particles. Negative ions are produced at the low energy end of the machine and accelerated to a positively charged, high voltage terminal in the center of the machine. In this terminal a gas target of thin foil is used to strip two or more electrons from the negative ions. The resulting positive ions are accelerated to ground potential. Their final energy is then $E = (q + 1)V$, where q is the charge on the positive ion leaving the high voltage terminal and V is the voltage on the terminal.

Sources which could produce ion beams with intensities ranging from 100nA to 1mA [52] [53] [54] were built. This goal was achieved for many elements by means of sputter ion sources.

2.8.2.1 Sputtering Sources

The various types of sputter sources have the common feature that the negative ions are formed on a low work function solid surface[52]. The typical element used for this task is caesium. A large range of solid surfaces sputtered by positive caesium ions will emit a significant fraction of negative ions. Addition of neutral caesium to the surface strongly enhances the yield of negative ions since this depresses the work function of the surface. The presence of caesium on the surface of the sputtering cathode is regulated by adsorption-desorption processes and by the bombardment with the positive caesium ions, used as sputtering projectiles. As the caesium on the surface will be sputtered mostly as positive ions, a large fraction of the sputtered caesium will be driven back to the surface by the cathode potential drop. This mechanism tends to stabilize the caesium coverage and limits the caesium consumption of the source. The design of the sputtering cathode, which is placed in a discharge opposite the outlet of the ion source, can be very important to ensure a highly efficient beam formation by focusing the negatively charged, sputtered ions onto the outlet opening.

2.8.2.2 Charge exchange method

The sputter source technology is, however, unsuited for production of negative ions with very low binding energies. For such ions the classical method of exchange process, which transforms a positive-ion beam to a negative-ion beam by passage through a gas or metal vapour cell, is still to be preferred. The competing electron-capture and electron-loss processes suffered by energetic atomic ions in collisions with a gas or a metal vapour target will lead to a statistical distribution of the charge states of the ions in the emergent beam. At sufficiently high target thickness, equilibrium between the com-

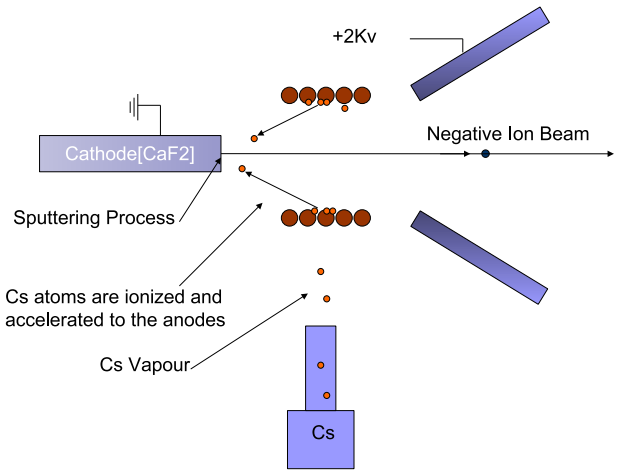

Figure 2.13: Diagram of the different steps that leads to a negative ion beam in a sputering Ion Source.

peting processes will be attained and the resulting equilibrium charge state distribution will be independent of the target thickness.

The formation of the negative beam by charge-exchange technique is usually a two-step process in which the projectile ion captures an electron, leading to the formation of an excited state or the ground state of the fast neutral beam, followed by a second capture process resulting in the formation of the negative ion. There are several factors to take into account to optimize the negative-ion formation[55], such as the projectile-target combination leading to as low-energy defect as possible in the two separate electron capture processes. This favours target atoms with low ionization potentials, such as the alkalis. The fully resonant process can, however, not be obtained since the lowest ionization potential for a metal (Cs) is larger than even the largest EA value. Thus the yield of negative ions formed by charge exchange is generally only of the order of 0.1-1%, which is sufficient for most studies dealing with the weakly bound negative ions.

2.8.2.3 Direct extraction

Direct extraction of a negative-ion from a Penning-type ion source[56] or a plasma ion source[57] is possible by reversing the polarity for extraction. The plasma ion source developed by Almén and Nielsen [57] for production of positive-ions beams can also handle less volatile elements such as metals by heating these sufficiently

2.9 High-Intensity Lasers

Studies of photon-ion interactions have been strongly linked with the development of photon sources, especially lasers. Sources that are able to deliver high photon flux at a narrow bandwidth have had a critical importance on the history of negative ions due to the low density targets achieved in these type of studies.

The way used to obtain high intensities is by squeezing the largest amount of energy that one can generate into the shortest period of time possible. Typically, the laser oscillator produces a very short pulse duration (nanosecond) and creates a pulse train, while the amplifier increases the energy of the output.

2.9.1 Oscillators

More than a decade ago, most MPI experiments were carried out using Q-switched lasers[58] which produce pulses of a few nanoseconds. However, the pulses produced had poor temporal behaviour with many uncontrolled and unpredictable intensity spikes. It is for that reason that the use of mode-locked lasers has become the standard in MPI experiments. In these type of lasers, the pulses are produced by "locking" a large number of laser cavity modes to a particular phase. This can be achieved by active (opto-acoustic modulators) or passive (saturable absorbers) means. Mode-locking lasers,

using a Ti:Sapphire crystal as the active medium, are commonly used due to the advantage over other systems of having the largest gain bandwidth (235mm FWHM) of all laser media. Another advantage is that it does not need an external element as a saturable absorber to mode lock but takes advantage of its internal nonlinear refractive index.

The axial modes of the Ti:Sapphire oscillator are spaced by the frequency of the pulse round trip. The highest pulse energies are achieved when all longitudinal modes periodically add up constructively: the modes are locked. The greater the number of modes that are involved, the shorter the pulses will be. The oscillators are 'self mode locked' thanks to a Kerr lens effect in the laser crystal [59]. Due to the non-linear response of the crystal, the effective refractive index varies with the laser intensity. As a consequence of this behaviour, it is possible to build the oscillator in such a way that the round trip losses become smaller as the intensity increases, which makes the oscillator most stable when all the axial modes lock together to give the highest peak intensities.

The limitation in generating short pulses comes from the dispersion and not from the gain bandwidth of the laser crystal. If at a particular time, all frequencies are in phase, the dispersion makes them all slightly dephased at the next round trip. The pulse width is then determined by the equilibrium between the self-mode-locking mechanism, which tends to shorten the pulse, and the dispersion, which tends to lengthen the pulse.

In order to get shorter pulses, the dispersion has to be compensated, and as shorter pulses implies a broad frequency spectrum, the compensation has to be over quite a range of wavelengths around the central one. Nowadays the best compensation is achieved with chirped mirrors [60]. Commercially available oscillators based on standard chirped mirrors offer pulses as short as 10fs.

2.9.2 Amplifiers

For most intense-field applications the initial pulse energy (∼1nJ) is insufficient and amplification is required. The amplification stage is based on the chirped pulse amplification (CPA) technique[61], where the short pulse is first stretched in time by a dispersive system such as a pair of diffraction gratings so that a chirped pulse is generated with the red end of the spectrum preceding the blue end. This reduces the peak intensity of the pulse greatly so it may be safely amplified. The pulse is then usually amplified to about 1mJ (∼six orders of magnitude) at a repetition rate of 1kHz and subsequently recompressed in a delay line with inverse dispersion. In order to achieve the amplification, the pulse has to pass several times through the Ti:sapphire crystal, usually pumped by the second harmonic of a Nd:YAG laser.

Two types of amplifier configurations are normally used, the regenerative amplifier and the multi-pass amplifier [62]. In the regenerative amplifier, the loading of the seed pulse in a linear cavity and the ejection of the amplified pulse are controlled by fast switching of the polarization with a Pockells cell in combination with thin polarizers. The advantage of this method is that the large number of passes (∼50) around the cavity allow for a low gain per pass, suppressing the build up of amplified spontaneous emission. While this configuration is preferable for relatively long pulses (∼50fs), it is not suitable for very short pulses, due to the higher order dispersion terms which make the recovery for the short pulses at the recompression stage difficult.
In the multi-pass amplifier the gain achieved is very high. The initial pulse is passed through the amplifying crystal with four curved mirrors. After a few cycles through the multi-pass amplifier, the beam passes through a Pockells cell, which picks one of the pulses. The selected pulse is re-injected in the amplifier for the final amplification. With this configuration it is easier to

compensate for the broadening that is introduced by higher-order-dispersion terms but now, another problem arises, the gain broadening. This effect is due to difference in gain for different wavelengths, leading to a lower limit of ∼20fs.

2.9.3 Measurement of Pulse Lengths.

Autocorrelation can be considered the classical way of estimating the length of an ultra short pulse. A simple implementation of this technique can be achieved with the setup in figure 2.14. The input pulse passes through a Michelson-type delay arrangement and the combined pulses are focused inside a light-emitting diode (LED), which exhibits a nonlinear power-dependent response [63]. The pulses from each arm must to be spatially collinear and temporally overlapped. The real-time monitoring of the autocorrelation function can be accomplished by mounting one of the mirrors on an audio loudspeaker with is made to scan at ∼20Hz, which varies the optical delay in the interferometer. When the path lengths for the two pulses are equal, the pulse will exactly coincide at the crystal and the amount of signal from the two photon absorption will be maximum, as the speaker changes the delay, signal will drop. When using this setup, the choice of the diode material is important. The bandgap must be sufficiently large to prevent direct absorption of the pulse photons.

For the measurements of pulse lengths below 50fs, autocorrelation is usually unsatisfactory. Recently, two methods of fully characterizing ultra-short pulses have emerged, namely frequency-resolved optical grating (FROG) and spectral phase interferometry for direct electric-field reconstruction (SPIDER). FROG is an autocorrelation technique in which the frequencies in the second harmonic pulse are resolved with a spectrometer [64], while SPIDER is a single shot technique and works with a non-iterative algorithm [65].

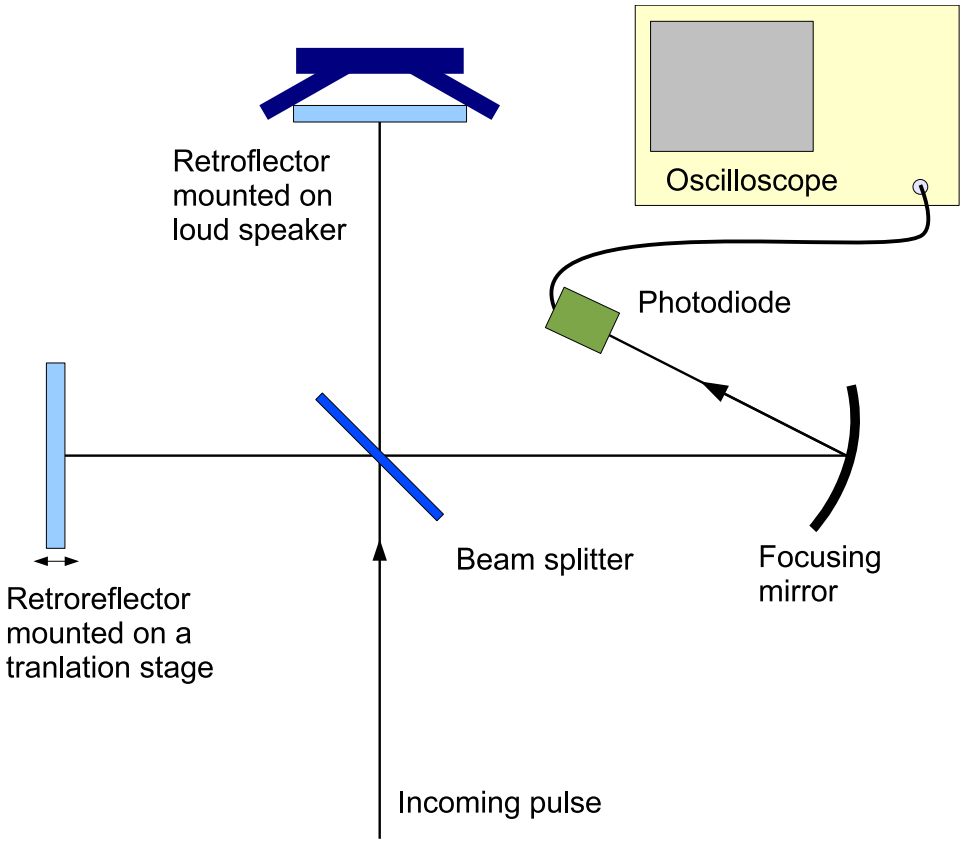

Figure 2.14: The configuration of a photodiode based autocorrelator.

2.9.4 Focusing to High Intensities

The final intensity produced by a laser pulse is determined by how the pulse is focused. If a Gaussian beam is assumed, the waist radius, ω_0, for which the laser intensity has dropped by a factor of e^2 with respect to the intensity at the center of the focus, is given by

$$\omega_0 = \frac{2\lambda f}{\pi D} \tag{2.32}$$

where D is the beam radius before focusing, λ is the wavelength of the laser and f is the focal length of the focusing element.

Along the axis of the laser beam, the length of the focus is indicated by the Rayleigh range, z_0. It is defined as the distance along the axis of the beam

at which the intensity drops by a factor of 2, and takes the form

$$z_0 = \frac{\pi\omega_0^2}{\lambda} \tag{2.33}$$

If we assume that the laser intensity $I(I_0, r, z, t)$ of a focused beam can be express as a Gaussian spatial profile with a squared hyperbolic-secant time envelope, then we can write [66]:

$$\begin{aligned} I(I_0, r, z, t) &= \left[\tfrac{I_0}{1+(z/z_0)^2}\right] \exp\left(-\tfrac{2r^2}{w_0^2[1+(z/z_0)^2]}\right) \cdot \operatorname{sech}^2(at) \\ &= I_0 \cdot f(r, z) \cdot g(t) \end{aligned}$$

where $a = 1.763/\tau$ so that $\operatorname{sech}^2(\frac{a}{\tau/2}) = 0.5$ and τ is the temporal FWHM of the laser pulse. A plot of $I(I_0 = 1, r, z, t = 0)$ can be found in figure 2.15. As can be seen from the contour plot, the intensity volume for lower intensities is much larger, so much, that some times the contribution to the total ion yield from lower intensities can compete with the contribution from the higher regions of the focus. In order to find the relation between the peak intensity that a pulse would create and the laser parameters, we need to integrate over all the space at z=0. This calculation will give us the energy per laser pulse:

$$\begin{aligned} Energy_{pulse} &= \int I(I_0, x, y, z = 0, t) dx dy dt = \int I(I_0, r, z = 0, t) \cdot r \cdot dr d\theta dt \\ &= 2\pi \int_0^{+\infty} \left\{ r \int_{-\infty}^{+\infty} I(I_0, r, t) dt \right\} dr = 4\pi \int_0^{+\infty} \left\{ r \int_0^{+\infty} I(I_0, r, t) dt \right\} dr \\ &= 4\pi \int_0^{+\infty} \left\{ r \int_0^{+\infty} I_0 f(r) g(t) dt \right\} dr = 4\pi I_0 \int_0^{+\infty} r \ f(r) dr \int_0^{+\infty} g(t) dt \end{aligned}$$

then:

$$\begin{aligned} \int_0^{+\infty} r \ f(r) dr &= \left(\tfrac{w_0}{2}\right)^2 \\ \int_0^{+\infty} g(t) dt &= \tfrac{1}{a} \end{aligned}$$

Finally:

$$\begin{aligned} E_{pulse} &= \tfrac{\pi w_0^2}{a} I_0 \\ \Rightarrow I_0 &= \tfrac{1.763}{\tau \pi w_0^2} E_{pulse} \end{aligned} \tag{2.34}$$

where now we have the peak intensity I_0 expressed as a function of known (or measurable) parameters of the laser.

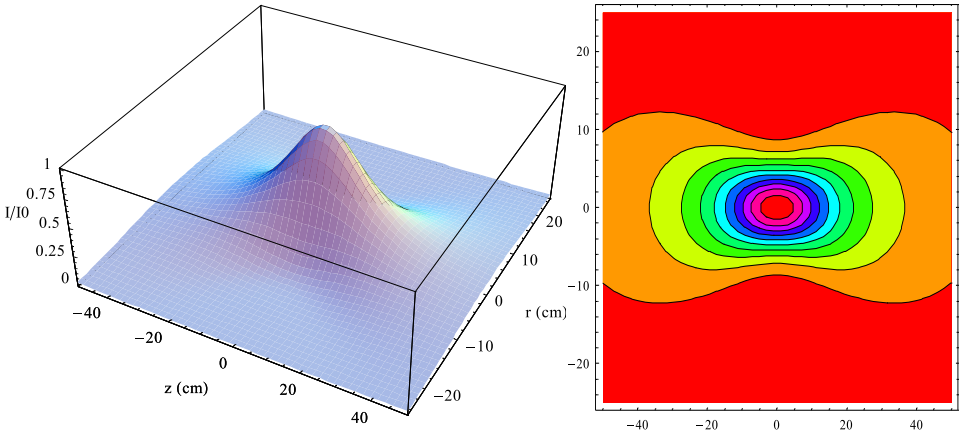

Figure 2.15: 3D and contour plot of $\frac{1}{1+(z/z_0)^2}\exp\left(-\frac{2r^2}{w_0^2[1+(z/z_0)^2]}\right)$, with $w_0 = 4.24\cdot 10^{-6}m$ and $z_0 = 7.07\cdot 10^{-5}m$. Note the change in the scale between r and z axis.

2.10 Conclusion

Advances in laser technology have produced unexpected results in intense laser interaction with atoms and ions. Several models appeared, trying to explain the unexpected non-sequential rates, but it was not until experiments capable of measuring the ion recoil momentum became possible that recollision clearly was identified as the main mechanism of the observed enhancement.

Despite the impressive progress made to date in the understanding of how atoms behave in intense fields, it has not been shown experimentally if any of these phenomena occur in negative ions. The search for strong field effects in "soft" negative ions is based on much more than simple curiosity. There are expected to be a number of significant differences in the behavior of negative ions in strong fields. The short range potential and lower binding energy means the electron's initial wave packet is much larger, thus altering

the rescattering amplitude. The electron is also not subject to a Coulomb field as it propagates in the laser field.

References

[1] J. J. Sakurai, *Advance Quantum Mechanics* (Reading, Mass., Addison-Wesley Pub. Co., ADDRESS, YEAR).

[2] R. G. Meyerand and A. F. Haught, Phys. Rev. Lett. **11**, 401 (1963).

[3] L. V. Keldysh, Soviet Phys. JETP **20**, 1307 (1965).

[4] F. Fabre, G. Petite, P. Agostini, and M. Clememt, J. Phys B: At. Mol. Opt. Phys. **15**, 1353 (1982).

[5] L. A. Lompr G. Mainfray, C. Manus, and J. Thebault, Phys. Rev. Lett. **70**, 766 (1993).

[6] P. Lambropoulus, Adv. At. Mol. Phys. **12**, 87 (1976).

[7] F. Yergeau, G. Petite, and P. Agostini, J. Phys. B: At. Mol. Opt. Phys. **19**, 1699 (1986).

[8] T. B. Kibble, Phys. Rev. **150**, 7060 (1966).

[9] P. H. Bucksbaum, R. R. Freeman, M. Bashanksy, and T. J. McIlrath, J. Opt. Soc. Am. B **4**, 760 (1987).

[10] R. R. Freeman and P. H. Bucksbaum, J. Phys B: At. Mol. Opt. Phys. **24**, 325 (1991).

[11] R. R. Freeman *et al.*, Phys. Rev. Lett. **59**, 1092 (1987).

[12] L. D. Landau and E. M. Lifshitz, *Quantum Mechanics. Non-relativistic Theory* (Pergamon, Oxford, 1965).

[13] G. F. Gribakin and M. Y. Kuchiev, Phys. Rev. A **55**, 3760 (1996).

[14] D. M. Volkov, Z. Phys. **94**, 250 (1935).

[15] A. M. Perelomove, V. S. Popov, and M. V. Terent'ev, Sov. Phys. JETP. **23**, 924 (1965).

[16] A. M. Perelomove and V. S. Popov, Sov. Phys. JETP. **25**, 336 (1967).

[17] M. V. Ammosov, N. B. Delone, and V. P. Krainov, Sov. Phys. JETP. **64**, 1191 (1986).

[18] I. F. A., D. J. E., and C. S. L., J. Phys. B: At. Mol. Opt. Phys. **25**, 4005 (1992).

[19] P. G. Burke, P. Francken, and C. J. Joachain, J. Phys. B: At. Mol. Opt. **24**, 761 (1991).

[20] K. T. Taylor *et al.*, J. Elecron Spectroscopy and Related Phenomena **144**, 1191 (2005).

[21] R. Abrines and I. C. Percival, Proc. Phys. Soc. **88**, 861 (1996).

[22] B. Walker *et al.*, Phys. Rev. Lett. **73**, 1227 (1994).

[23] D. N. Fittinghoff, P. R. Bolton, B. Chang, and K. C. Kulander, Phys. Rev. Lett. **69**, 2646 (1992).

[24] V. Schmidt, *Electron Spectrometry of Atoms using Synchrotron Radiation* (Cambridge University Press, Cambridge, England, 1977).

[25] P. B. Corkum, Phys. Rev. Lett. **713**, 1994 (1993).

[26] R. Moshammer *et al.*, Phys. Rev. Lett **84**, 447 (2000).

[27] T. Weber *et al.*, Phys. Rev. Lett. **84**, 443 (2000).

[28] K. C. Kulander and K. J. Schafer, Proc. Int. Conf. Multi Photon Processes VI, ed D K Evans (Singapore: World Scientific) (1993).

[29] K. J. Schafer, B. Yang, L. DiMauro, and K. C. Kulander, Phys. Rev. Lett. **70**, 1599 (1993).

[30] T. Brabe, M. Y. Ivanov, and P. B. Corkum, Phys. Rev. A **54**, R2551 (1996).

[31] J. L. Hall, E. J. Robinson, and L. M. Branscomb, Phys. Rev. Lett **14**, 1013 (1985).

[32] C. Blondel, Phys. Scr. T **58**, 31 (1995).

[33] C. Blondel, M. Crance, C. Delsart, and A. Giraud, J. Phys. B **24**, 3575 (1991).

[34] M. D. Davidson, H. G. MWuller, and H. B. van Linden van den Heuwell, Phys. Rev. Lett **67**, 1712 (1991).

[35] H. Stapelfeldt, P. Balling, C. Brink, and H. K. Haugen, Phys. Rev. Lett. **67**, 1731 (1991).

[36] C. Pan and A. F. Starace, Phys. Rev. A **44**, 324 (1991).

[37] H. K. Haugen, AIP Conf. Proc. **295**, 105 (1994).

[38] H. Stapelfeldt and H. K. Haugen, Phys. Rev. Lett. **68**, 2638 (1992).

[39] H. Stapelfeldt *et al.*, Phys. Rev. A **50**, 1618 (1994).

[40] T. A. Patterson *et al.*, Phys. Rev. Lett. **32**, 189 (1974).

[41] J. Slater, F. H. Read, S. E. Nowick, and W. C. Lineberger, Phys. Rev. A **17**, 201 (1978).

[42] J. P. Greenwood *et al.*, J. Phys. B: At. Mol. Opt. Phys. **36**, L235 (2003).

[43] P. Kristensen *et al.*, Phys. Rev. Lett. **78**, 2329 (1997).

[44] V. V. Petrunin, M. Harbst, and T. Andersen, Phys. Rev. A **63**, 030701 (2001).

[45] P. Kristensen *et al.*, Phys. Rev. Lett. **71**, 3435 (1993).

[46] R. Reichle, H. Helm, and I. Y. Kiyan, Phys. Rev. A **87**, 243001 (2001).

[47] I. Y. Kiyan and H. Helm, Phys. Rev. Lett. **90**, 183001 (2003).

[48] R. Kopold and W. Becker, J. Phys. B: At. Mol. Opt. Phys. **32**, L419 (1999).

[49] P. McKenna, Ph.D. thesis, University of Belfast, 2000.

[50] R. Geller, Status of the Multiply Charged Heavy-ion Source MINIMAFIOS, Rev. Sci. Inst. **56**, 1505 (1985).

[51] G. Melin, Rev. Sci. Inst. **61**, 236 (1990).

[52] R. Middleton, IEEE Trans. Nucl. Sci. **NS-23**, 1098 (1976).

[53] P. Tykeson, H. H. Andersen, and J. Heinemeier, IEEE Trans. Nucl. Sci. **NS-23**, 1104 (1976).

[54] R. Middleton, *A Negative-Ion Cookbook* (Department of Physics, University of Pennsylvania, Philadelphia, 1989).

[55] P. Tykeson, *The Productionof Heavy Negative IonBeams through Charge Exchange Processes* (Symposium of Northeastern Accelerator Personnel, Oak Ridge, Tennessee, 1978).

[56] E. Heinicke, K. Bethge, and K. Baumann, Nucl. Instr. and Meth. **58**, 125 (1968).

[57] O. Almén and K. O. Nielsen, Nucl. Instr. and Meth. **1**, 302 (1957).

[58] G. Mainfray and C. Manus, Rep. Prog. Phys. **54**, 1333 (1991).

[59] D. E. Spence, P. N. Kean, and W. Sibbett, Opt. Lett. **16**, 42 (1991).

[60] A. Stingl, C. Spielmann, F. Krausz, and R. Szipocs, Opt. Lett. **19**, 204 (1994).

[61] D. Strickland and G. Mourou, Opt. Commun. **56**, 219 (1985).

[62] J. Kawanaka, K. Yamakawa, H. Nishioka, and K. Ueda, Opt. Lett. **28**, 2121 (2003).

[63] D. T. Reid *et al.*, Opt. Lett. **22**, 233 (1997).

[64] T. M. Shuman *et al.*, Opt. Express **5**, 134 (1999).

[65] R. Trebino *et al.*, Rev. Sci. Instrum. **68**, 3277 (1997).

[66] B. Chang, P. R. Bolton, , and D. N. Fittinghoff, Phys. Rev. A **47**, 4193 (1993).

Chapter 3

The experimental Apparatus

3.1 Introduction

The basic experimental approach to study the multiphoton ionization in strong laser fields has been outlined in chapter 2 and involves focusing high energy pulses from state-of-the-art laser systems (intensities in the range $10^{13}W/cm^2$ to$10^{17}W/cm^2$) into gas targets or ion beams inside a vacuum chamber. The ionized products are resolved in a suitable configuration of deflectors and a channeltron.

3.1.1 LabView

During the design of the system, it was decided that it was going to be a set-up with a high degree of computerization. For this purpose, four National Instruments data acquisition cards were purchased. The function of these cards is to act as a bridge between the computer software and the system. This communication implies the control of different power supplies, which deliver current and voltages to different parts of the apparatus, move stepper motors, or control and monitoring of the vacuum system, as well as reading the TTL pulses sent by the channeltron, or the signal of an electrometer. All the software for such a broad scope of applications was developed with

the help of the commercial programming language LabView. A good way to describe LabView could be: "LabView is a graphical programming language that uses icons instead of lines of text to create applications. In contrast to text-based programming languages, where instructions determine program execution, LabView uses dataflow programming, where the flow of data determines execution. In LabView, you build interface is built by using a set of tools and objects. The user interface is known as the front panel. You then add code using graphical representations of functions to control the front panel objects. The block diagram contains this code. In some ways, the block diagram resembles a flowchart."(Paragraph taken from the LabView's "User Manual"). The intensive use of LabView will be clear in the following sections, except on the laser system which belongs to an external laser facility.

3.2 The Laser System

The laser system used during the experiment was located in the Max Plank Institute for nuclear physics in Heidelberg. The laser pulses generated were centred at a wavelength of 800nm and had a pulse duration of 25fs. They were generated by a Ti:sapphire Kerr-lens mode locked oscillator (see section 2.9.1) and amplified to an energy of 250mJ at a 3kHz repetition rate. The passage of the beam through the vacuum window was calculated to lengthen the pulse to 30fs.

The laser beam was shaped by a 12mm iris aperture and was focused by an on-axis spherical mirror of focal length 100mm, giving a maximum power of 0.60W. Using equation 2.32 and 2.33 we obtain $\omega_0 = \frac{2\lambda f}{\pi D} = 4.24\mu m$ and $z_0 = \frac{\pi\omega_0^2}{\lambda} = 70.7\mu m$. For this configuration, the peak intensity calculated using 2.34, gives a value of $I_0 = 2 \cdot 10^{16} W/cm^2$.

The radiation was converted from linear to circular polarization by insertion of a quarter wave plate into the output beam and the intensity was controlled by the rotation of a half wave plate placed in front of a linear polarizer.

3.3 Target Ion Beam Preparation

A review of the different ways to obtain positive and negative ion beams was given in section 2.8. In our experimental set-up the negative ions were produced by a caesium sputtering ion source.

3.3.1 Ion Source

The Peabody Scientific PS-120 Caesium Sputter source [1], low-energy version is versatile and compact, capable of producing a broad selection of negative ions. The low energy version can produce ions accelerated up to 10keV.

The source, shown in figure 3.1b, consists of an oven and a main chamber, the main chamber containing an ionizer and a target cathode. The ionizer is essentially a filament of which there are two variations, either a spherical or helical heated ionizer. The difference between them is just the pattern with which they sputter the cathode, the spherical ionizer producing a uniform sputtering, while the helical focuses the sputtering to a point. The ionizer and chamber are biased at the same voltage while the cathode is insulated to enable it to be negatively biased relative to the rest of the chamber. The process of creating the negative ion beam starts when the liquid caesium contained in the reservoir is evaporated in an oven 3.1a, then the caesium vapor drifts into the main chamber where it has two functions. The first function is to form a thin layer on the cathode surface, lowering the work function of the cathode, which consists of a moveable, water-cooled cylinder

with a large hole facing the anode. This hole is filled with a certain mixture depending on which ion the source should produce. The second function of the caesium vapor is to be surface ionized upon contact with the ionizer, creating Cs^+. The target cathode having been biased at a negative voltage, attracts the positive caesium ions towards it. All neutral states of the fragments from the mixture are sputtered by Cs ions. A relatively large amount of negative ions are emitted since the fragments easily catch an electron when they pass the Cs layer on the way out from the cathode. The negative ions are accelerated by the same field as the positive Cs ions but in the opposite direction. When they have left the source, they can be post-accelerated up to 10keV.

The control of the ion source is done through a LabView code. The front panel, in typical operating conditions is shown in figure 3.2

3.3.2 Beam Transport

A schematic representation of the experimental arrangement is shown in figure 3.3. After a first einzel lens, the beam goes through two more einzel lenses and vertical and horizontal deflection plates. The lens and deflection system are mounted using stainless steel rods with isolation and all the connections are made to a high voltage rated vacuum feedthrough using shielded Kapton wire.

The beam is focused into the entrance of a 30^o analysing magnet. The transverse magnetic field provides momentum analysis. Water cooling of the magnet plus a fan placed in front is necessary to avoid overheating (maximum current in the magnet: 1A). Just after the magnet, there are a pair of 2mm apertures 50mm apart. They help to ensure that only the desired ion species is transported down the beam line as well as to collimate the beam, reducing its dispersion. They also present an excellent point where

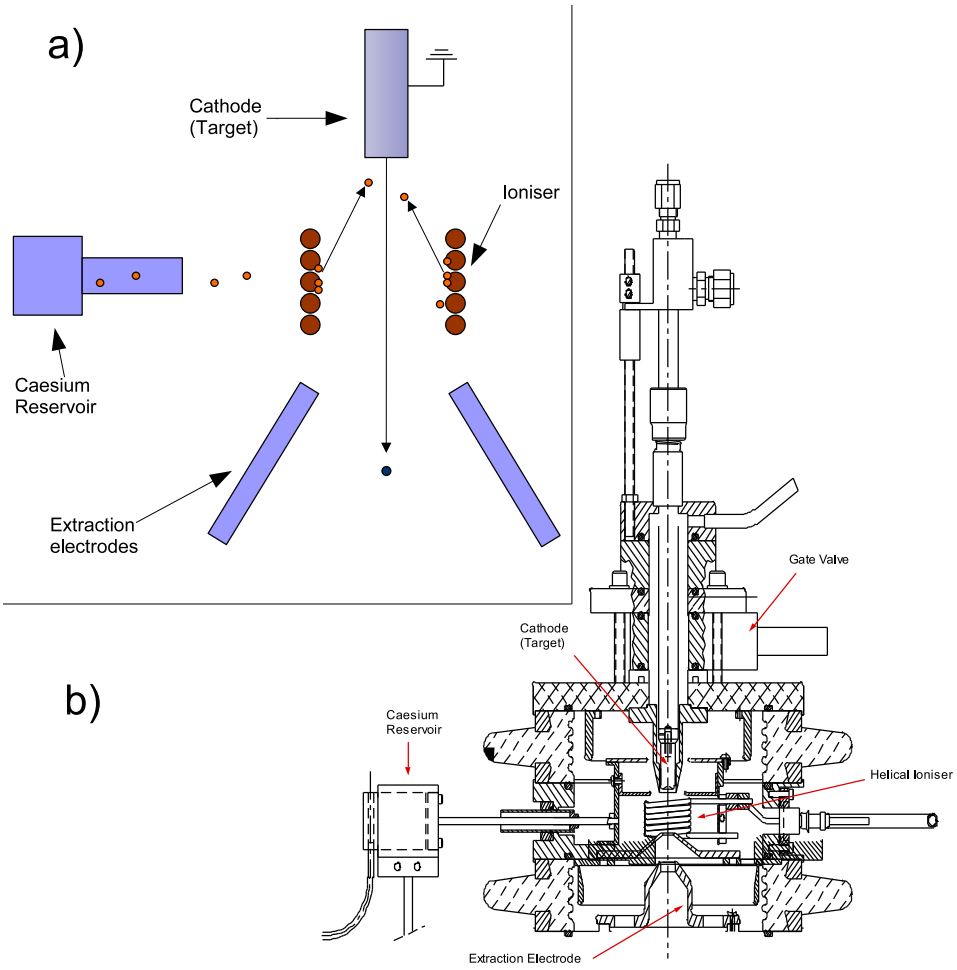

Figure 3.1: Peabody Scientific PS-120 Caesium Sputter source: a)Schematic diagram b)Technical drawing

to measure the beam current.

After the aperture, the beam arrives to another set of horizontal and vertical deflectors as well as horizontal and vertical translators and an einzel lens. The control of these deflectors are integrated in the same code that controls the ion source, see figure 3.2.

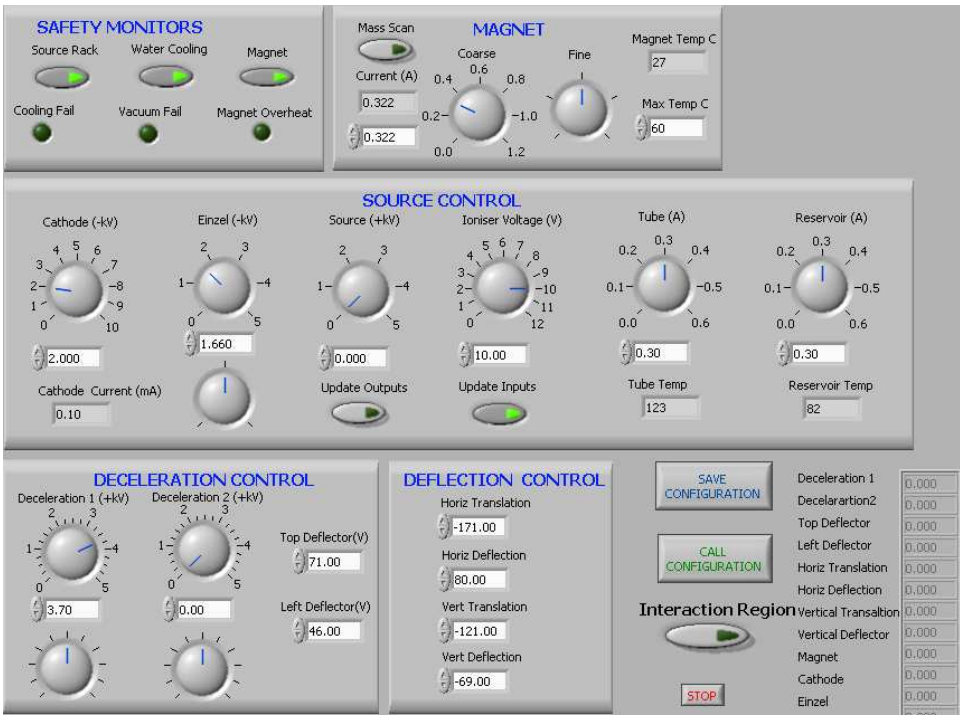

Figure 3.2: Front panel of the LabView code that controls the operation of the Caesium sputtering source

3.4 Interaction Chamber

The interaction chamber consists of a 6-way cross vacuum chamber. The main objective of this chamber is to allow the study of the interaction of a pulsed high intensity laser beam with the negative ion beam under study. In order to achieve this objective, the two beams are overlapped at 90^o.

The laser waist was $15\mu m$ while the negative ion beam was usually of the order of 0.5mm. To facilitate overlap of the beams, a 4-cross slit was incorporated. It was mounted onto a linear motion drive and can determine the position of the ion beam with a precision of 0.05mm. A diagram of the 4-cross slit can be seen in figure 3.4. The slit b), with dimension $2mm \times 10mm$, was used to determine the profile of the ion beam by moving the slit a cross the ion beam, while recording the intensity on the Faraday cup. This measurement gives the full width at half maximum (FWHM) and the centre

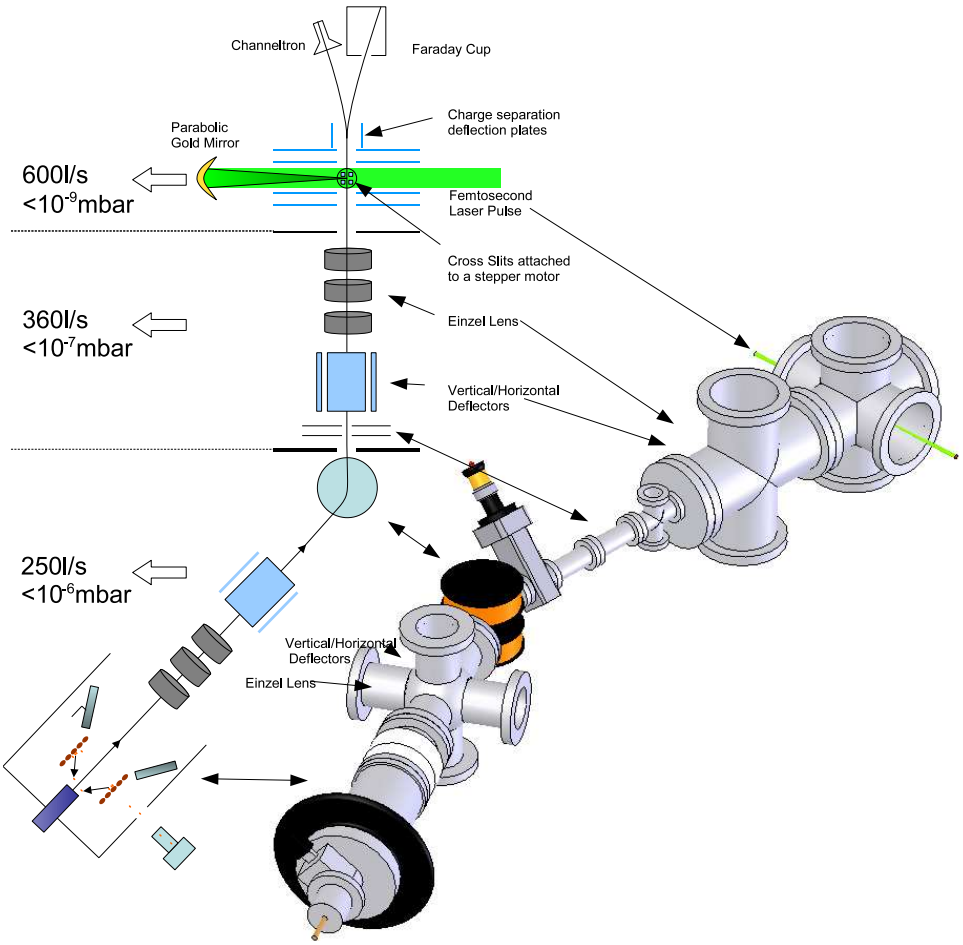

Figure 3.3: Representation of the main parts of the experimental setup.

position of the beam. By adjusting the different deflectors along the beam line, the ion beam was forced to pass through the 4-way hole in the mount, see figure 3.4(Side View), that was positioned at exactly the axis of the chamber. For the spatial positioning of the laser, we "played" mainly with three elements of the laser beam line in charge to bring the laser from the optical table to the interaction chamber: two 45^0 mirrors and a parabolic gold mirror of 100mm of focal length. By adjusting these mirrors, the laser beam was correctly positioned. Once inside the vacuum, the laser was reflected and focused by a parabolic gold mirror, which was mounted onto a mechanical drive support so that the focus could be moved along the perpendicular ion

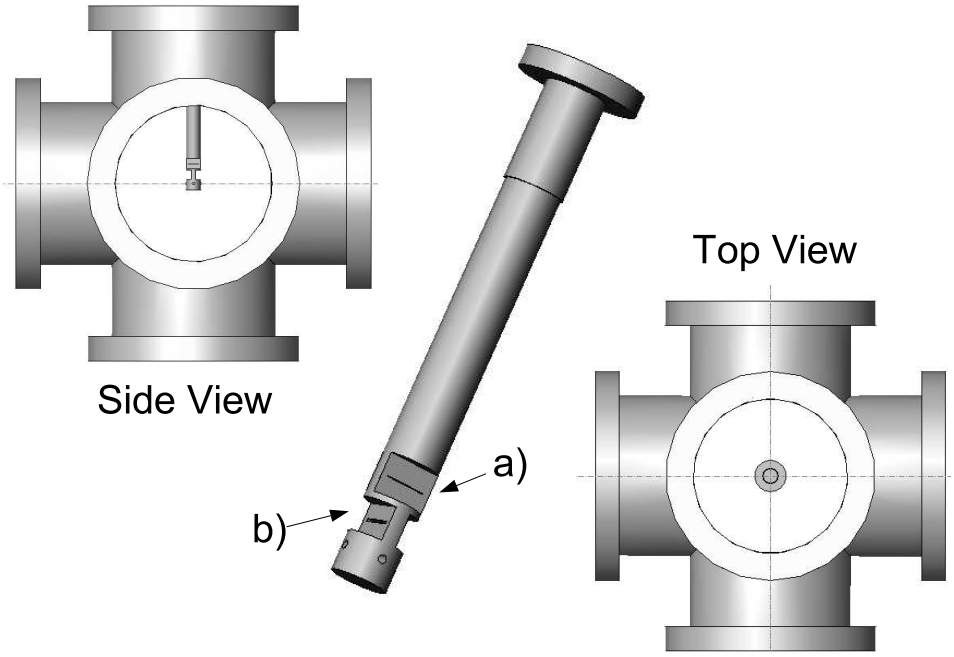

Figure 3.4: Diagram of the 4-Way Slit used to position the laser and ion beam.

beam axis.

To be sure that this first undesired interaction will not perturb the final data, the intensity of the laser prior to focusing can be estimated using:

$$I = \frac{E_{pulse}}{\tau\pi(D/2)^2} \tag{3.1}$$

hence, if $D = 12mm$, pulse length $\tau = 30fs$, and energy per pulse $E_{pulse} = 200\mu J$, the intensity of the laser beam previous focusing is $\simeq 6 \cdot 10^7 W/cm^2$. This intensity is in the MPI regime, so it is possible to calculate the crossection. Taking into account that the ponderomotive energy is negligible at these intensities ($U_p(\lambda = 800nm, I = 6 \cdot 10^7 W/cm^2) = 3.6 \cdot 10^{-6} eV$), three photons are needed to detach an electron from F^-, (EA=3.4eV). The crossection calculated using equation 2.2.2 give us $\sigma_3 = 3.57 \cdot 10^{-82} cm^6/s^2$. A rate of $\Gamma_n = \sigma_n (I/w)^n = 4.5 \cdot 10^{-3} s^{-1}$ is obtained. Multiplying by the pulse length (30fs) give us $1.35 \cdot 10^{-16}$counts/laser pulse. So clearly, this first interaction between the two beams does not introduce any significant error

in the final measurement.

A Faraday cup was used to measure the negative ion beam intensity. The positive ion products were separated from the main beam using deflection plates and were detected using a ceramic channel electron multiplier (CEM) from AmpTek, model MD-502.

3.5 Vacuum Arrangement

The entire vacuum system has been based on standard conflat flanges and fittings where possible. This modular design allows fast and easy modifications to be made to the set-up when necessary. The vacuum system is divided into two sections by a MCD "E-6V-1500M" mechanic vacuum gate. This gate allows to open to air one side (for modification or repairing) while keeping the other under vacuum.

In the first section, an Edwards Active Pirani Gauge situated in the manifold system measure the pressure in the $100 - 1 \cdot 10^{-3} mbar$ regime. It's function is to indicate when the pressure is low enough ($< 10^{-2} mbar$) to start safely the 250l/s Edwards Turbomolecular Pump "EXT250". Once the turbo pump is at full speed, the pressure is monitored by an Edwards Active Ion Gauge, with a range of $5 \cdot 10^{-3} mbar - 2 \cdot 10^{-11} mbar$. The initial low vacuum is achieved using an Edwards "18 Two Stages" rotary pump. An oil mist filter is attached to the rotary pump to prevent any possible oil diffusion into the system, see figure 3.5 .

The second section can be divided in two parts. The deflection system is pumped by a 360l/s pump while in the interaction chamber the vacuum is achieved by a combination of a 600l/s Leybold pump and a 250l/s. In this section, the initial vacuum is achieved by another Edwards "18 Two Stages" rotary pump, see figure 3.6 .

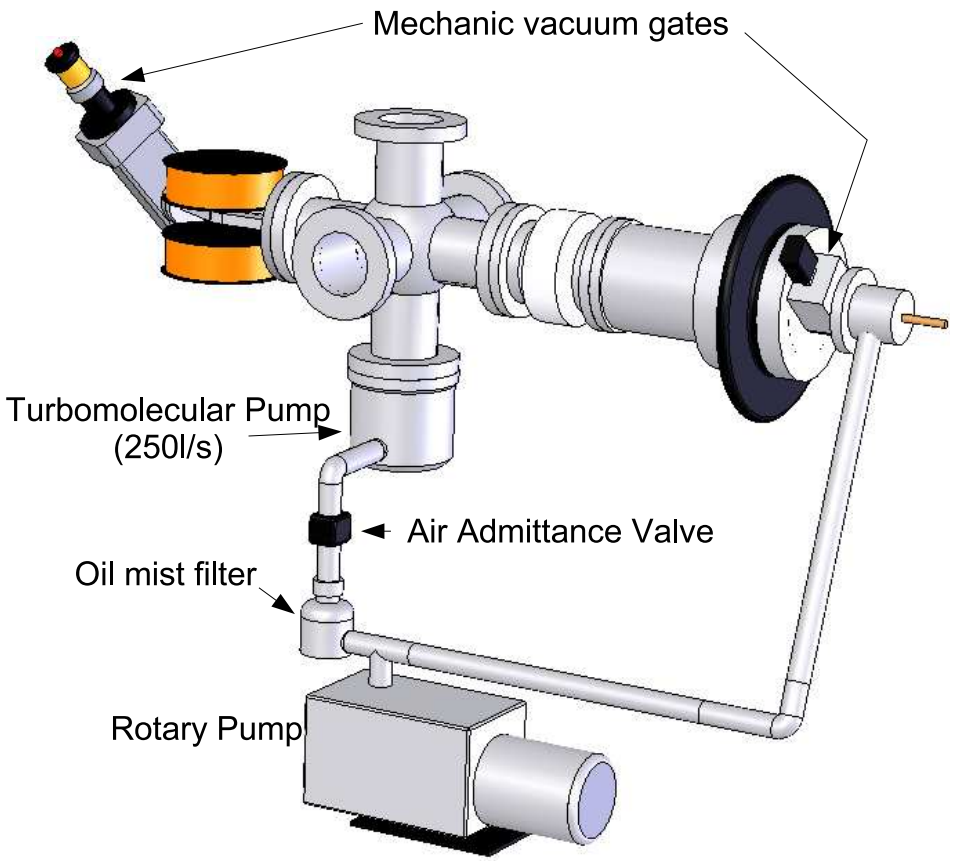

Figure 3.5: Vacuum arrangements for the Ion Source section.

In order to achieve a better vacuum in the interaction region, the second sections were baked for a period of 48 hours at temperatures of the order of 150^oC. This was achieved using a resistively heated wire in direct contact with the chambers which were then wrapped with aluminum paper. Typically the base pressure at the interaction region falls below $1 \cdot 10^{-9} mbar$.

Several electronic Edwards IPVA10EK Air Admittance Valves are distributed through the system to seal the system in case of an abnormal situation.

All the different pressure gauges, turbopumps and safe valves are monitored using a home-made LabView code. This PC-control approach allows a trigger system to be easily set up.

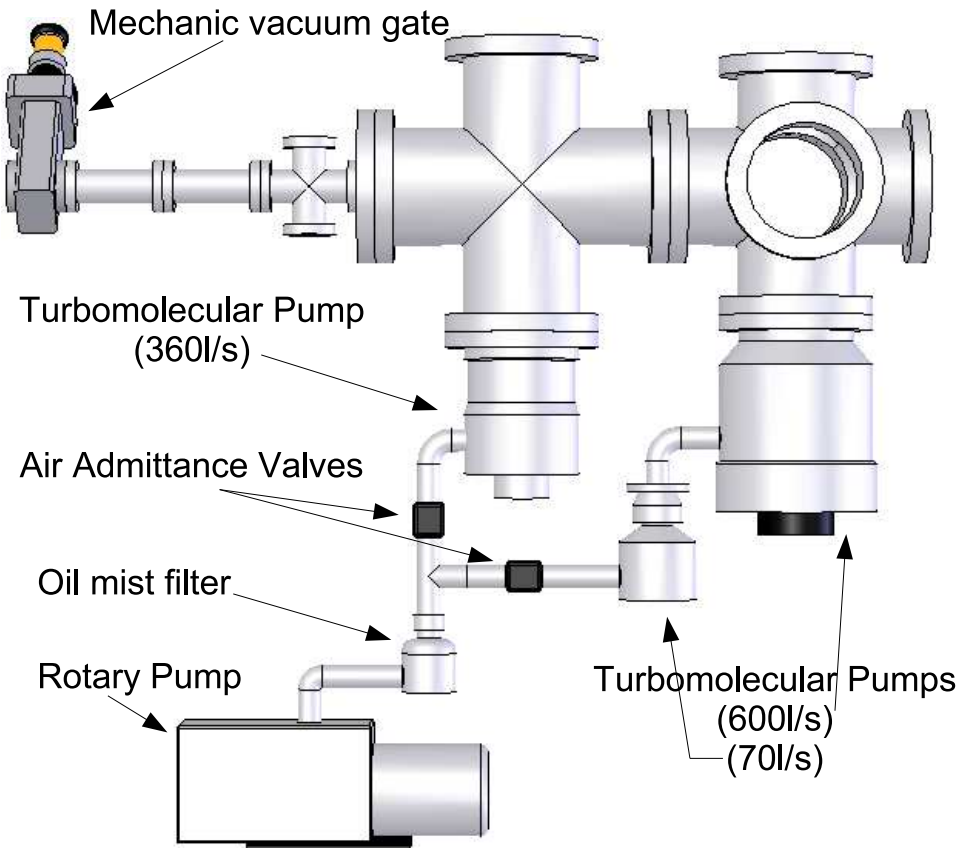

Figure 3.6: Vacuum arrangements for the Interaction section.

3.6 Signal Extraction

The interaction point is situated among a set-up of plates that allows the use of a "voltage labelling" technique. In this configuration, the centre of the interaction region is biased thus the energy of the ion beam is reduced by E_{bias}. As the initial negative ions are created with an energy $-S$, where S is the potential applied to the cathode, the energy of the ions in the bias region will be $-S' = -S + E_{bias}$. So, if we consider the following reaction of a cluster of anions caused by the laser field:

$$X_n^- \rightarrow X_i^{+q} \tag{3.2}$$

we can calculate[1] the expression for the energy and the time of arrival at the channeltron for the positively charged ions, X_i^{+q}:

$$\begin{aligned} E_3 &= \tfrac{q}{2}(I - D) \\ t_4 &= d_4\sqrt{\tfrac{m_u}{2e}}\sqrt{\frac{m}{-S+E_{bias}+\frac{ngE_{bias}}{i}}} \\ \tan\theta &\approx \tfrac{qDd_3}{2E_3d_6} \end{aligned} \tag{3.3}$$

Equations 3.3 are only an estimation but outline the main advantages of this technique. First, by adjusting the voltage on the deflector plates, it is possible to discriminate the ion X_i^q created inside the biased region from the X_i^q created outside and obviously also from the other states charged ions, $X_i^{q'}; q' \neq q$ as the deviation angle θ (which depends on the deflection voltage, D and the charge state, q) would be different. The second advantage from this technique is that the time of flight from the interaction spot to the channeltron for the X_i^q created inside the biased region, is different than for the rest, allowing us to discrimate it in time. The electronic box of the channeltron sends a TTL pulse (+5V; 220ns wide) every time a particle hits the detector. That puts a restriction on our detection scheme: if two charged particles arrive at the channeltron with a difference in time of less than 220ns separation, the second one will not be counted. For this reason, the noise rate was kept well below this limit. The TTL pulse sent by the charge amplifier of the channeltron detector was directed to a counter on one of the computer cards. Using a laser trigger pulse, the LabView software was written so that the counts were only accepted, or counted, if they were inside a specified time window.

An example of the values of the deflection voltage and the time windows used to measure the product of a 1.5keV I^- beam are listed in table 3.1.

This combination of specific time window plus deflection voltage, allows the reduction of the background counts significantly (as low as 1 count every

[1] See appendix, A.3.

Ion	Time Window	$V_{Deflection}$
I^+	$4.1 - 4.3\mu s$	670V
I^{+2}	$4.1 - 4.2\mu s$	350V
I^{+3}	$4.0 - 4.2\mu s$	240V

Table 3.1: Example of values used to measure positive ions on the channeltron

two minutes).

References

[1] R. R. Corderman, P. C. Engelking, W. C. Lineberger, Appl. Phys. Lett. **36**, 1470 (1962).

Chapter 4

Experimental Results

In the present chapter, the experimental work, which was carried out at the Max Plank Institute (Heidelberg, Germany) as a result of a collaboration with the research group of Professor J. Ullrich, will be presented. From a two months run at Heidelberg, the first evidence for an enhancement of double ionization on F^- negative ions was obtained. In order to do so, a particularly sensitive test for the existence of rescattering was performed, which consisted of the comparison between ion yields obtained using linearly and circularly polarized light. In a circularly polarized field, the electron tends to orbit the core rather than recollide, causing a dramatic suppression of ion yields in double ionization [1].

4.1 Optimization techniques

4.1.1 Mass Scan

The sputter source generates a great variety of products, from which the desired ion needs to be mass selected. In order to achieve that, a 30° bending magnet was placed in the beam line. By changing the current delivered to the magnet, the m/q ratio [1] was selected. The intensity at the Faraday cup

[1] See appendix A.2 for a demonstration of this relation.

as a function of the magnet current was selected and the optimum current for the desired species was found. Figure 4.1 shows measured mass scan curves. Each graph shows the cathode used for the generation of negative ion desired for the experiment, the energy of extraction as well as the main ions and charge states present.

4.1.2 Overlap

To overlap the beams, the focal position was systematically varied until signal was obtained. Once the optimal height was determined, the lens was translated and the ratio for detection of C+ was measured. In figure 4.2a), it is possible to see how there is a relative minimum at the centre and two maximums at the sides. This agrees with the 'peanut-shaped' focal volume described in section 2.9.4. The intensity is higher in the middle but the focal volume is small. For lower intensities the increase in volume makes the total counts higher. By looking at the generation of C^{2+}, it is possible to confirm the position of the focus as the required intensity for ionization of C^{+} is higher.

To optimize the deflection of the ions into the detector, the ion yield as a function of the deflection voltage has to be measured. For a $2keV$ beam of F^{-}, interacting with the maximum intensity available ($I_0 \approx 10^{16} W/cm^2$) we obtained figure 4.3. Now we know accurately which voltage we need to use.

The final step is to determine, experimentally, the time window. This was achieved by recording the signal at different time intervals to build up a time of flight (TOF) spectrum. An example of a TOF spectrum recorded by our acquisition system can be found in figure 4.4, where the ion yield from a Xe gas at a pressure of $4.5 \cdot 10^{-8} mbar$ was recorded for one hour. Up to Xe^{6+} was observed.

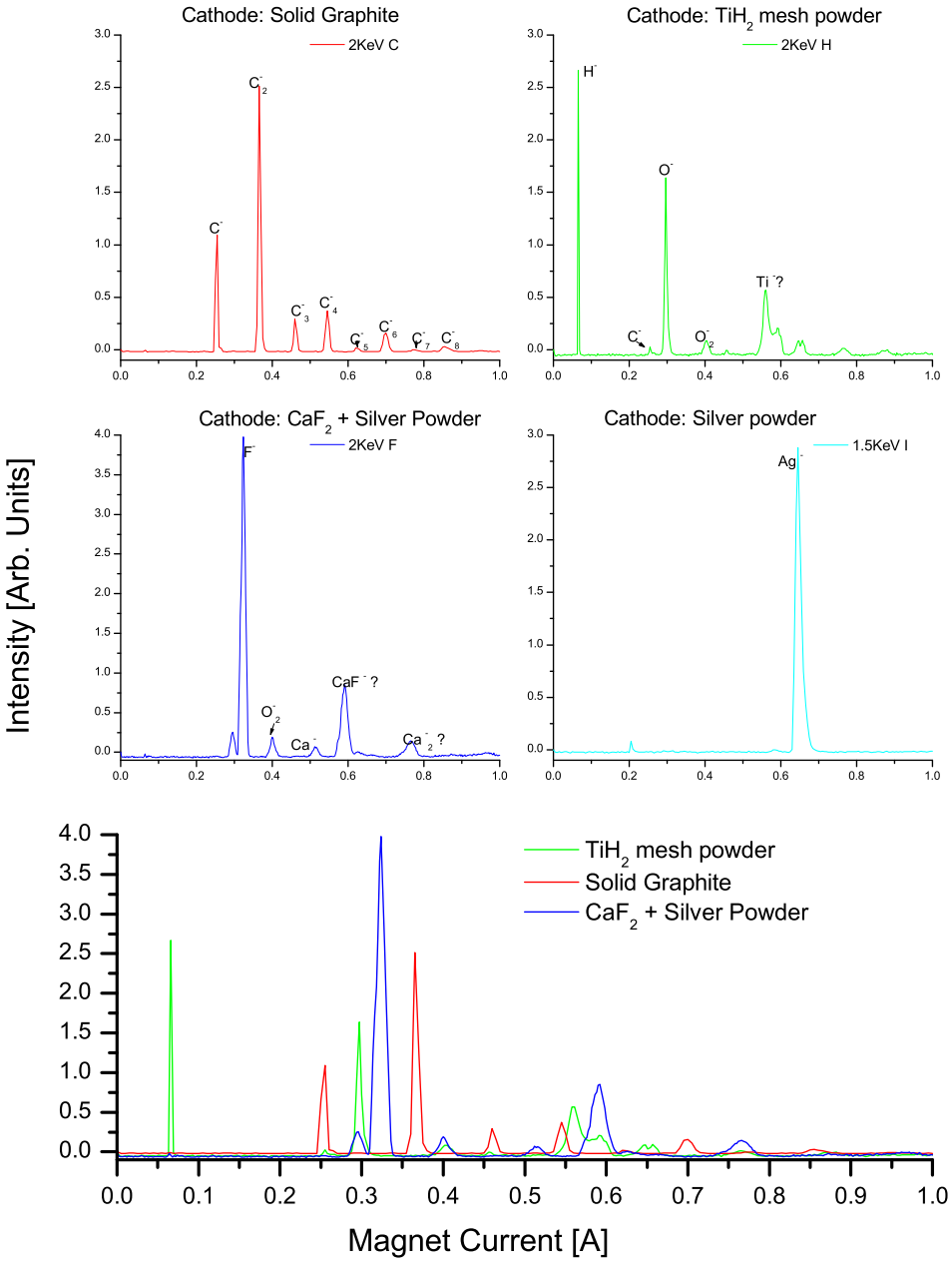

Figure 4.1: Several scans performed with the magnet. The cathode used, the desired negative ion and the beam energy are specified for each graph.

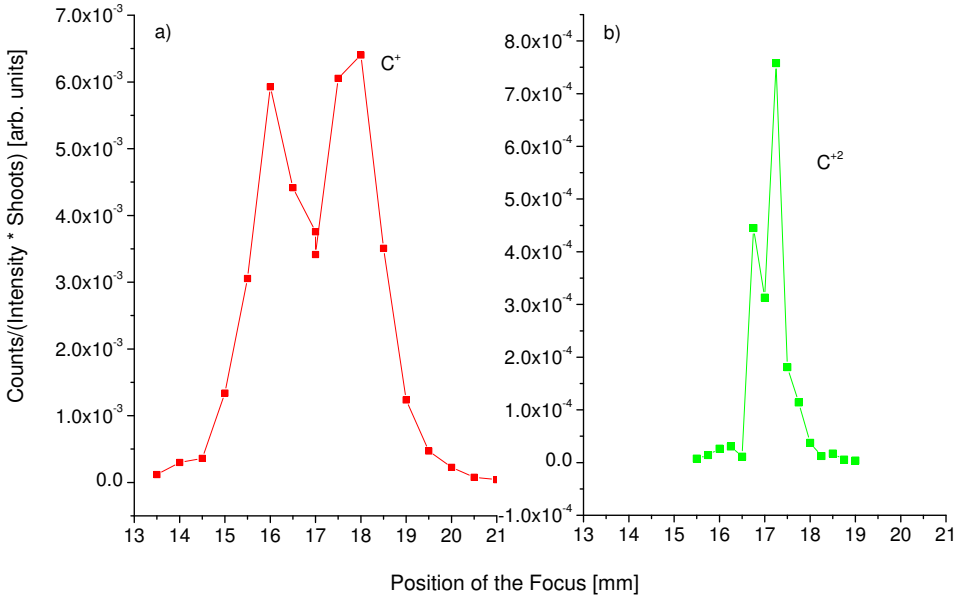

Figure 4.2: Example of the determination of the focus position. Ion Yield from C^- beam at full intensity of: a) C^+ b) C^{2+}.

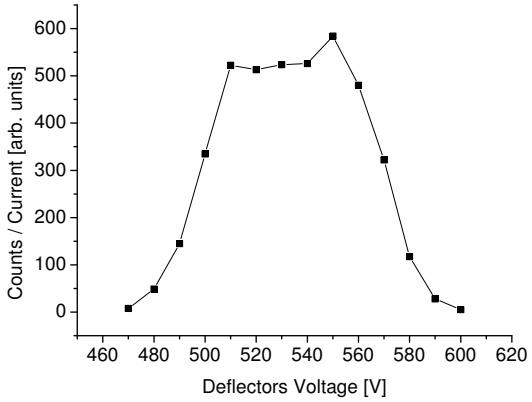

Figure 4.3: Ion yield of F^+ from a 2keV beam at $I_0 \approx 10^{16} W/cm^2$ as a function of the deflection voltage.

4.2 F^- Ion Beam Target: Measurements

The main experimental difficulty in studying recollision in negative ions stems from the fact that neutralization will occur before the intensity of the pulse becomes sufficiently high for excitation or ionization of the core.

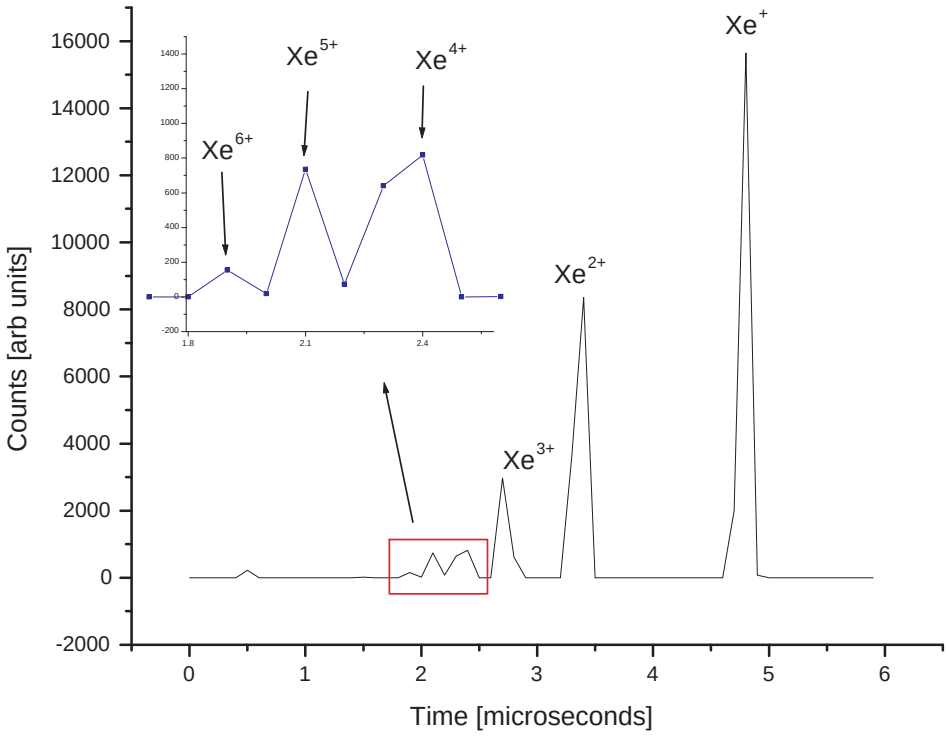

Figure 4.4: Time of flight spectrum from Xe gas.

Therefore, a high electron affinity is desirable in order to increase the survival of the negative ion population during the rising of the laser pulse. The extra electron needed for the formation of a negative ion of F leads to a closed shell configuration[2], making F^- electron affinity relatively high ($EA_{F^-} = 3.4eV$, see table 1.1).

To produce the negative fluorine ion beam, a calcium fluoride cathode was used (CaF_2, melting point 1300° C). The initial beam was accelerated to 2keV. Typical currents were between 25nA and 40nA. The interaction region (see section 3.6) was biased to -400V, and a scan on the deflection voltages determine an optimum applied voltage of 530V, see figure 4.3. The time window used was $2.8 - 3.0\mu s$. In order to reduce the intensity of the

[2]This argument is valid for all the halogens.

laser beam, an iris in the optical path with a diameter of 10mm was introduced.

The possible drift on power of the laser was checked before and after each measurement. For circular polarization measurements, a $\lambda/4$ waveplate was inserted. The laser was stable during the time it took to perform the experiment, approximately 20 hours.

To be sure that no more than one ion was going to the channeltron from a single shot, the $\frac{counts}{number\ of\ shoots}$ was monitored so that it was well below 0.5. The reason for that is due to limitation on the channeltron, see section 3.6.

As changes in overlap of the two beams could have occurred during the course of a scan due to slight fluctuation in the position and shape of the ion beam, the reproducibility of the measurements over the full range of intensities was checked over the course of the data acquisition. At high intensities, saturation in the sequential removal of the two electrons was demonstrated as the ion yield increases in proportion to $I^{1.5}$ due to the expansion of the focal volume [2]. The acquired data is plotted in figure 4.5 with the error bars shown representing the statistical error in the result at a 68% confidence interval.

4.3 F^- Ion Beam Target: Discussion

4.3.1 Survival

The survival of the negative population during the rising of the laser pulse is a potential limitation. By using a short pulse duration, a rapid transition to high intensities was provide, increasing the survival of the negative ions. Using the theoretical cross sections for single detachment described in section 2.2.2, we have calculated the expected population of negative ions as a function of time during the laser pulse. To calculate the population we have

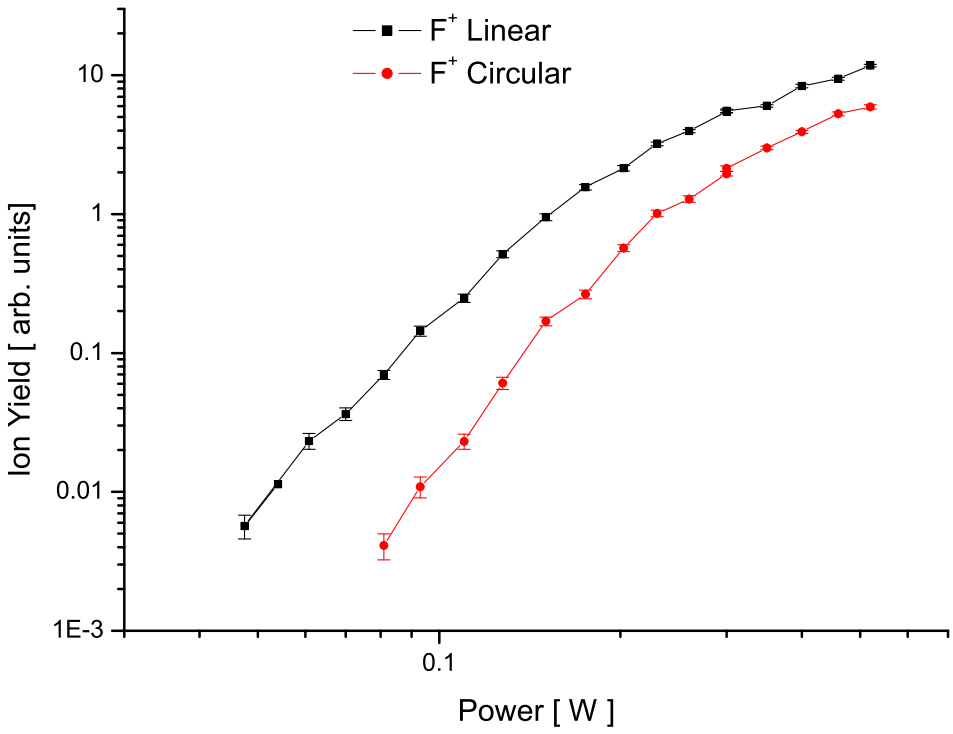

Figure 4.5: F^+ ion yield from the process $F^- + n \cdot h\nu \rightarrow F^+ + 2e$.

used:

$$\begin{aligned} \tfrac{dP_{F^-}}{dt} &= \Gamma_n(I_0,t)\ P_{F^-} \\ P_{F^-}(I_0,t) &= \exp\Big[-\textstyle\int_{-\infty}^{t}\Gamma_n(I_0,t')dt'\Big] \\ P_{F^-}(I_0,t=-\infty) &= 1 \end{aligned} \tag{4.1}$$

where Γ_n is given by equation 2.10 [3]:

$$\Gamma_n(I_0,t) = \sigma_n\big(I/w\big)^n \tag{4.2}$$

Where I is the intensity of the laser and is described by equation 2.34 and w is the energy per photon, but for the present calculation, the time dependence needs to be included,

$$I = I_0(r,z)\mathrm{sech}^2(at) \tag{4.3}$$

[3]The calculated values for Γ_n were computed using a home made Fortran code. The values obtained from our code were checked to match the values in ref [5].

where $a = \frac{1.763}{\tau}$. For the rest of the present section I will refer to I_0 instead of $I_0(r, z)$. So, with the equations 4.2 and 4.3 the peak intensity as a function of the time and the population can be written as:

$$I_0 = \omega \left[\frac{\ln(1/P_{F^-})}{\sigma_n f(n,t)} \right]^{1/n} \qquad (4.4)$$
$$f(n,t) = \int_{-\infty}^{t} sech^{2n}(at')dt'$$

In our case ($\lambda = 800nm \quad ; \quad \omega = 1.5480eV \quad ; \quad EA = 3.399eV$), a minimum of 3 photons are needed when U_p is zero (there is still no laser $\rightarrow t = -\infty$), but when the laser pulse starts to rise, the increase of the value of U_p increases the number of photons needed for detachment, this is known as "closing channels". Table 4.1 shows our calculated value of U_p and the time at which the channel is opened (in the sense that the previous channel closes) using equation 4.5.

$$E_{electron} = 0 \Rightarrow n\hbar\omega = (EA + U_p)$$
$$\ldots$$
$$cosh(at) = \sqrt{\frac{9.33 \cdot 10^{-20} \lambda^2 I_0}{n\hbar\omega - EA}} \qquad (4.5)$$
$$cosh(at) = x \rightarrow at = \ln(x + \sqrt{x^2 - 1})$$

n	ω [eV]	U_p [eV]	t [s]
2	3.0996	–	–
3	4.6494	–	$-2.415 \cdot 10^{-14}$
4	6.1992	2.80	$-1.576 \cdot 10^{-14}$
5	7.7490	4.34	$-9.820 \cdot 10^{-15}$

Table 4.1: Peak Intensity $I_0 = 10^{14} W/cm^2$

The first excited state threshold for atomic fluorine is $E_{F^*} = 12.70eV$, if we have a 30fs laser pulse with a peak intensity of $I_0 = 10^{14} W/cm^2$,

knowing that the maximum recollision energy is $3.17U_p(t)$, we find that the inequality $3.17U_p(t) \geq E_{F^*}$ is true for $t \geq -1.10627 \cdot 10^{-14}s$. We assume that $t = 0$ corresponds to the peak intensity. Figure 4.6 shows the number of photons required for photodetachment as a function of time for several peak intensities.

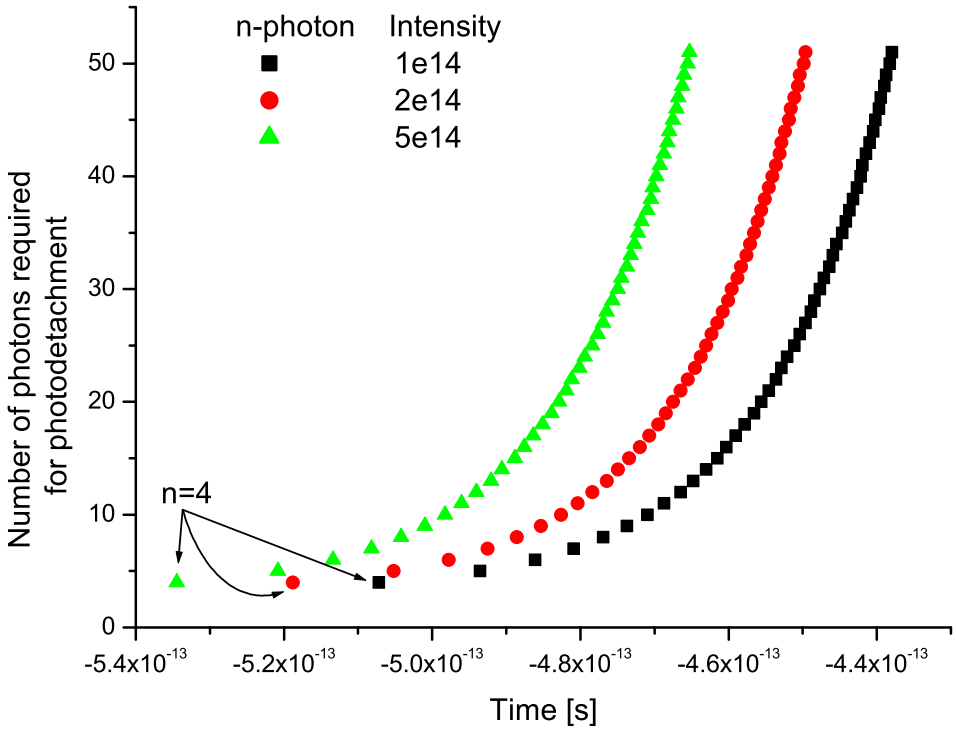

Figure 4.6: The dots represents the minimum number of photons required for photodetachment, so the first dot is when the 3photon channels close, and the 4^{th} open, the second dot is when the 5^{th} open and so on.

To calculate the population of F^- using multiphoton theory, we need to justify that we are actually in the multiphoton regime. This is given by the Keldysh parameter γ. If we calculate how γ changes during a laser pulse for a peak intensity $I_0 = 10^{14}W/cm^2$ we find figure 4.7, clearly the value of γ remains $\gg 1$. The F^- population has been calculated as a function of time for a fix peak intensity value equal to $10^{14}W/cm^2$. In this calculation has been included only the closing of the n=3 channel, due that the opening

of n=5 happen when the population is already zero. This seems to indicate that the population of F^- at the time when $3.17U_p(t) \geq E_{F^*}$ is low. However, even at lower intensities, when a quantum description of the process is undertaken, excitation or ionization can still proceed if the phases of the core electron and the returning wave packet are favourable. Given that the electron can also initially absorb extra photons through excess photon detachment, double detachment can be produced from recollision at intensities lower than the classical threshold. Theoretical evidence for this can be seen in H^- for which recollision excitation of the neutral H is significant despite the classical recollision energy being a factor of 3 too low [3]. In another study, the time dependent Schrödinger equation was solved directly for Li^-. The intensity at which these calculations were made corresponds to a maximum classical return energy which is at least an order of magnitude lower than that needed for excitation. Yet, the authors were able to infer from their results an enhancement in double ionization by recollision, from the observation of an increased rate with a single cycle pulse compared with a double half cycle pulse [4].

4.3.2 Ion Yield Calculations

To determine if there are any re-scattering effects in our result, the contribution from sequential ionization must be extracted. To calculate this we have followed the scheme of Chang et. al.[6]. The rate equations for sequential ionization under collisionless conditions can be written as

$$\begin{aligned}
\tfrac{dp_0}{dt} &= -\Gamma_0\ p_0 \\
\tfrac{dp_1}{dt} &= -\Gamma_1\ p_1 + \Gamma_0\ p_0 \\
\tfrac{dp_2}{dt} &= -\Gamma_2\ p_2 + \Gamma_1\ p_1 \\
&\cdots \\
\tfrac{dp_n}{dt} &= +\Gamma_{n-1}\ p_{n-1}
\end{aligned} \tag{4.6}$$

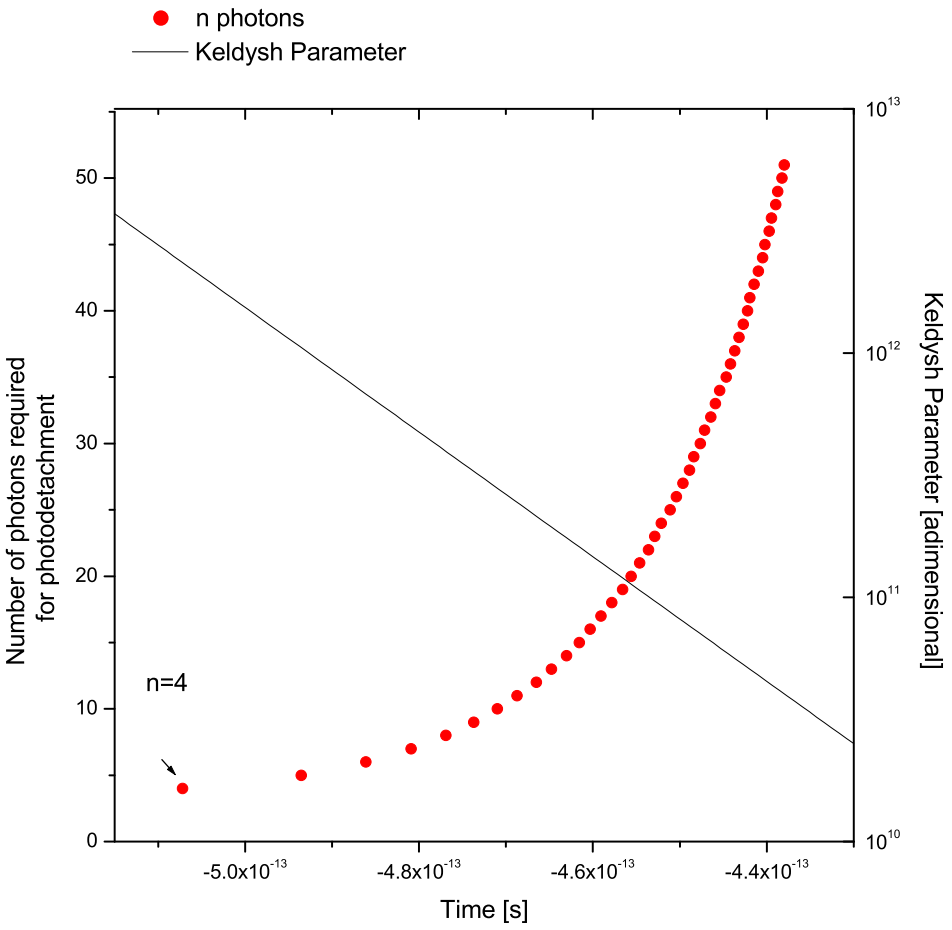

Figure 4.7: Same as figure 4.6, but now including the value of the Keldysh parameter.

where p_k represents the probability that the atom is k times ionized. The rate coefficients Γ_k depend implicitly on both space and time.

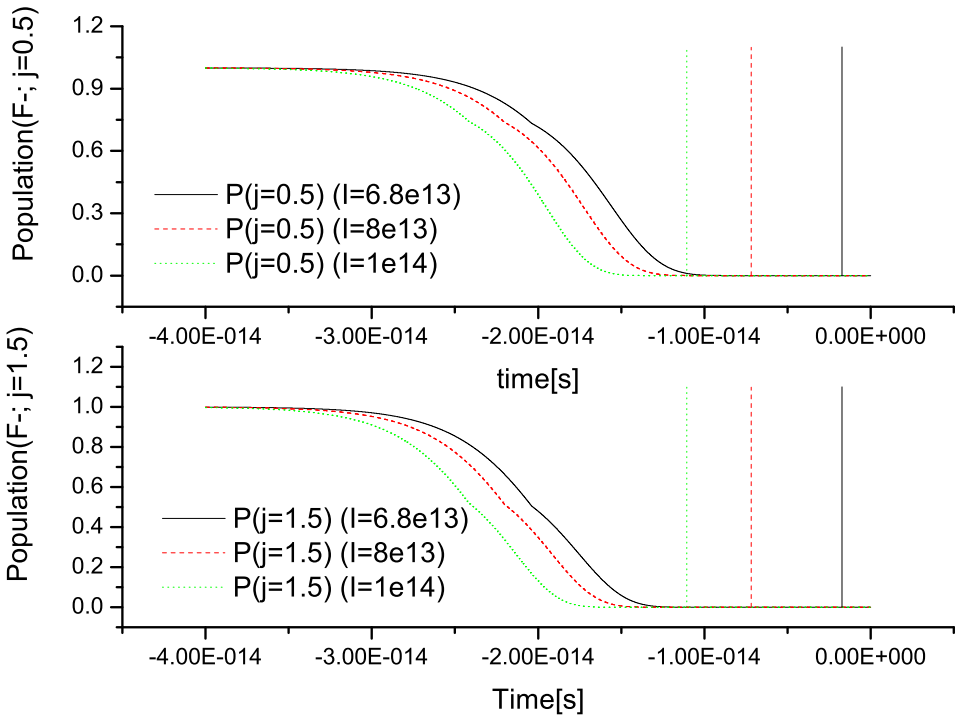

Figure 4.8: Population of F^- as a function of time for several peak intensities for $j = 1/2, j = 3/2$. Solid line: $I_0 = 6.8 \cdot 10^{13} W/cm^2$; Dashed line: $I_0 = 8 \cdot 10^{13} W/cm^2$; Dots: $I_0 = 10^{14} W/cm^2$.; The vertical lines correspond to the time at which $3.17 U_p(t) = E_{F*}$

The formal solution of equation 4.6 at a fixed point in space is

$$\begin{aligned} p_0(t) &= \exp[-\Phi_0(t)] \\ p_1(t) &= \exp[-\Phi_1(t)] \int_{-\infty}^{t} \exp[\Phi_1(s)] \Gamma_0(s) p_0(s) ds \\ p_2(t) &= \exp[-\Phi_2(t)] \int_{-\infty}^{t} \exp[\Phi_2(s)] \Gamma_1(s) p_1(s) ds \\ &\ldots \\ p_{n-1}(t) &= \exp[-\Phi_{n-1}(t)] \int_{-\infty}^{t} \exp[\Phi_{n-1}(s)] \Gamma_{n-2}(s) p_{n-2}(s) ds \\ p_n(t) &= \int_{-\infty}^{t} \Gamma_{n-1}(s) p_{n-1}(s) ds \end{aligned} \tag{4.7}$$

where $\Phi_k(t)$ is the running integral of Γ_k

$$\Phi_k(t) = \int_{-\infty}^{t} \Gamma_k(t') dt' \tag{4.8}$$

To write the set of equations 4.7, it is assumed that $p_0(t = -\infty) = 1$ and

$p_k(t=-\infty)=0$ for $k\neq 0$.

To determine the ion yield, we need to calculate equation 4.7 for $t=+\infty$. Integrating over isointensity shells greatly simplifies the integration:

$$\begin{aligned} N_k &= \rho \int_{-z_{min}}^{+z_{max}} \int_{-y_{min}}^{+y_{max}} \int_{-x_{min}}^{+x_{max}} p(x,y,z)dxdydz = \\ &= \rho \int_0^{V_{max}} p(V)dV = \rho \int_{I_{max}}^{I_{min}} \frac{dV}{dI}\cdot p_k(I)\cdot dI \end{aligned} \tag{4.9}$$

where ρ is the beam density that has been considered constant, which is a good assumption given that the size of the laser focus was much less than that of the ion beam, and $\frac{dV}{dI}$ is just the equation that describes a isointenisty shell.

For a laser beam described by

$$I(I_0,r,z,t)=\Big[\frac{I_0}{1+(z/z_0)^2}\Big]\exp\Big(-\frac{2r^2}{\omega_0^2[1+(z/z_0)^2]}\Big)\cdot Sech^2(at) \tag{4.10}$$

the volume [7] inside an isointensity boundary defined by I is:

$$V=V_0[\frac{2}{9}\xi^3+\frac{4}{3}\xi-\frac{4}{3}\arctan(\xi)] \tag{4.11}$$

where

$$\xi=[\frac{I_0}{I}-1]^{1/2} \quad ; \quad V_0=\frac{\pi^2 w_0^4}{\lambda} \tag{4.12}$$

Now, we just need to differentiate the equation 4.11:

$$\frac{dV}{dI}=-\frac{V_0}{6}\frac{\xi}{I}[5+\xi^2] \tag{4.13}$$

As $\frac{dV}{dI}<0$, this reflects the fact that the volume enclosed decreases when the intensity increase. Introducing equation 4.13 into 4.9 we finally obtain:

$$N_k=\rho\frac{V_0}{6}\int_{I_{min}}^{I_0}\frac{\xi}{I}[5+\xi^2]p_k(I)dI \tag{4.14}$$

After all these equations, the only thing left to calculate is the integral in equation 4.14. For this purpose a Fortran code was written[4]. The code

[4]The code can be found in appendix B.1

uses the tunnelling theory (ADK, see section 2.3.1) for the ionization of an electron with a orbital quantum number $l = 1$. The initial ion beam is considered that populates the states of $m = 0$ and $m = 1$ equally. These two cases are computed separately and added at the end ($F^+ = \frac{1}{3}F^+(m = 0) + \frac{2}{3}F^+(m = 1)$). The result of these calculations are shown in figure 4.9. In the saturation region, it is known that the ion yield is still increasing due

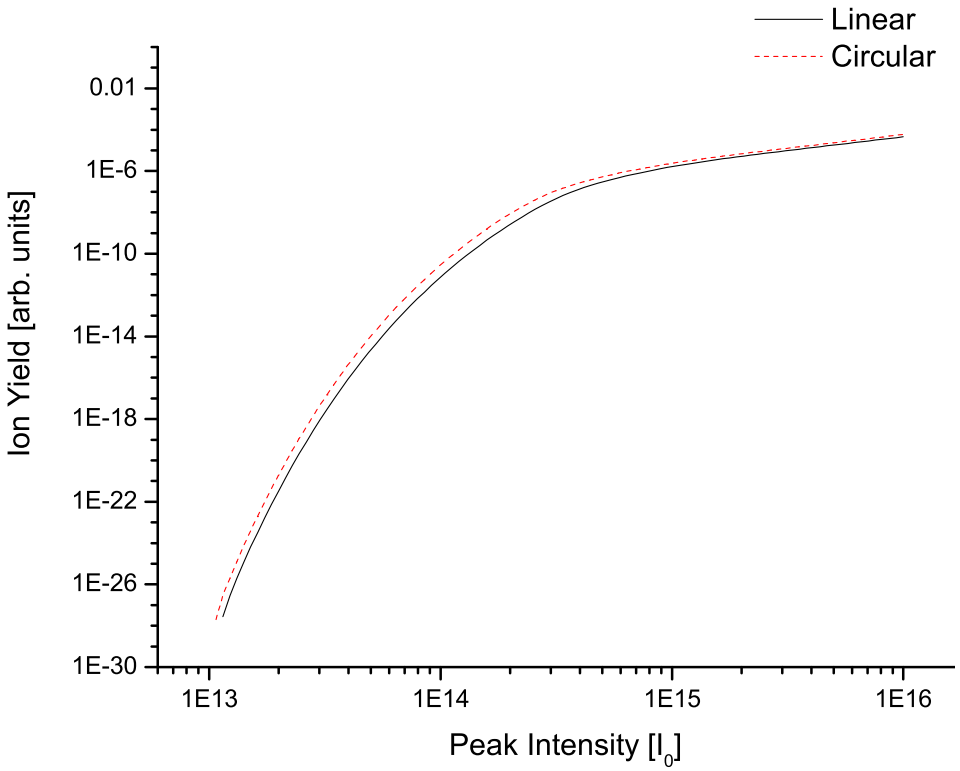

Figure 4.9: Ion Yield calculated using ADK theory for atomic fluorine. Solid line: Linear polarized light; Dashed: Circular polarized light.

to the expansion of the focal volume. In this region we can consider that $p_k(I) = 1$ in equation 4.9. If we perform the integral of $N_k \propto \int_{I_{min}}^{I_0} \frac{\xi}{I}[5+\xi^2]dI$ using the software *Mathematica*, it gives us

$$N_k \propto \left[\frac{\sqrt{-1+\frac{a}{x}}\left(4+\frac{a}{x}\right)\left(\frac{-2\,a}{3\,x^{3/2}}-\frac{22}{3\sqrt{x}}\right)x^{3/2}}{a+4\,x} + \frac{8\sqrt{-1+\frac{a}{x}}\left(4+\frac{a}{x}\right)x^{3/2}\,\arctan\left(\frac{\sqrt{a-x}\sqrt{x}}{-a+x}\right)}{\sqrt{a-x}\,(a+4\,x)} \right]_0^{I_0} \tag{4.15}$$

(where $a = I_0$; $x = I$), which is easily simplified to

$$\begin{aligned} N_k &\propto \left[\tfrac{2}{3}(I_0 - 11)\sqrt{I_0 - x} - 8\arctan\sqrt{\tfrac{x}{I_0 - x}}\right]_0^{I_0} \\ &= \tfrac{2}{3}I_0^{3/2} + \tfrac{22}{3}I_0^{1/2} - 4\pi \\ &\Rightarrow N_k \propto I_0^{3/2} \end{aligned} \tag{4.16}$$

As our experimental data tends to $\propto I^{3/2}$ at high intensities, this gives confidence that the density of our ion beam is constant over the laser volume.

4.3.3 Intensity Shift

The first thing that one notices when performing the calculation of the process $F^0 \rightarrow F^+$ using ADK theory is the fact that the ion yield for the circular case exceeds that for the linear. This is just a reflection of the fact that the electric field in the circular case is always "on" during a cycle. In the saturation region the intensity is so high that any atom inside the volume is ionized, so both curves should come together after saturation. If the electric field strength for the circular polarization is multiplied by a factor of 1.31, the two theoretical curves display excellent agreement in the saturation region, see figure 4.10. To be able to compare the experimental data with the theoretical calculations, the experimental curves also need to be shifted. Knowing that a factor of 1.31 is needed for the theoretical curves, we can deduce the necessary shift for our data:

$$\begin{gathered} I = \langle S \rangle = \tfrac{\langle E^2 \rangle}{\mu_0 c} \\ E_{Linear} = E_0 \cos(\omega t) \rightarrow \langle E^2 \rangle_L = \tfrac{E_0^2}{2} \\ E_{Circular} = E_0[\cos(\omega t)\hat{x} + \sin(\omega t)\hat{y}] \rightarrow \langle E^2 \rangle_C = E_0^2 \\ \Rightarrow I_L = \tfrac{I_C}{2} \\ N_L^{Theory}(I) = N_C^{Theory}(I \cdot 1.31) \\ N_L^{Exp}(I_L) = N_C^{Exp}(I_L \cdot 1.31) = N_C^{Exp}(\tfrac{I_C}{2} \cdot 1.31) \end{gathered} \tag{4.17}$$

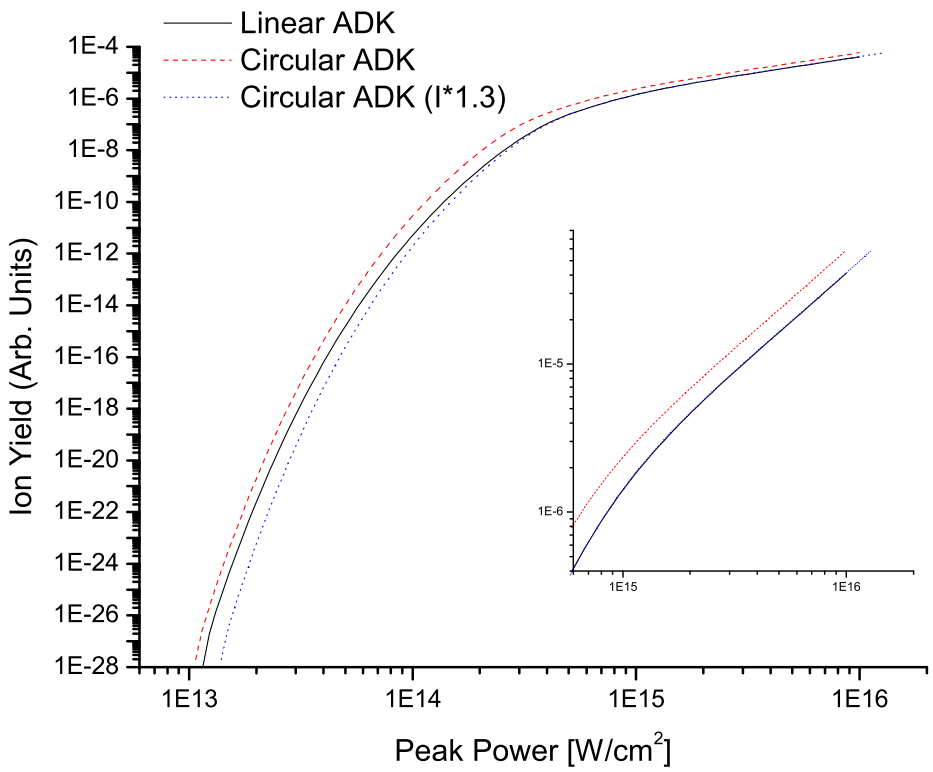

Figure 4.10: Ion Yield calculated using ADK theory for atomic Fluorine. The inset is to show more clearly the match between the Linear and the Circular once they are shifted.

where S is the Poynting vector and $\langle S \rangle$ means the average value of S. Equations 4.17 tell us that we need a factor of 0.655. The result of applying this factor is shown in figure 4.11. In order to compare the theoretical curves with the experimental results, the absolute intensity scale has been additionally shifted to provide the best fit to the ADK curves. This adjustment lies within the uncertainty in our experimentally measured intensity. Clearly, the introduction of this factor facilitates the comparison between both curves. As been shown before, in the saturation region the ion yield increases in proportion to $I^{1.5}$ due to the expansion of the focal volume if the approximation of constant density is valid. By taking the last eight points for the linear polarized light and doing a linear regression we found that the yield is proportional to 1.51 in a logarithmic scale ($\propto I^{1.5}$), justifying, our assump-

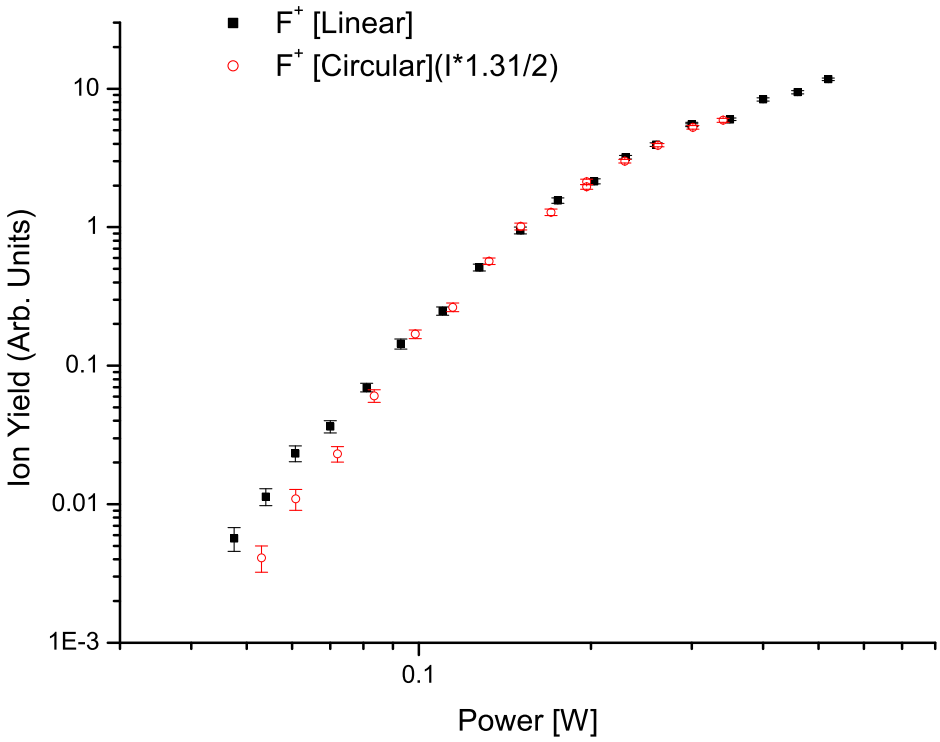

Figure 4.11: Experimental data shifted for better comparison.

tion.

The evidence of an enhancement on the production yield for the linear case in front the circular case can be clearly seen. A circularly polarized laser beam is a coherent superposition of photons with definite helicity, e.g., +1, so in absorption of every photon, the projection of the electron orbital momentum onto the beam propagation direction increases by +1. Since the tunnelling ionization according to PPT theory corresponds to absorption of a great number of photons, the continuum electron will have very large orbital momentum projection and hence a large orbital momentum. As a result, the centrifugal repulsion will not allow the free electron to come close to the residual ion. Therefore, the interaction of the free electron with the bound electrons may be neglected and the circular case should have no re-scattering

with the core. The observed enhancement for the linear case provides clear evidence for a re-scattering contribution to the channel ionization of F^- [8], see figure 4.12

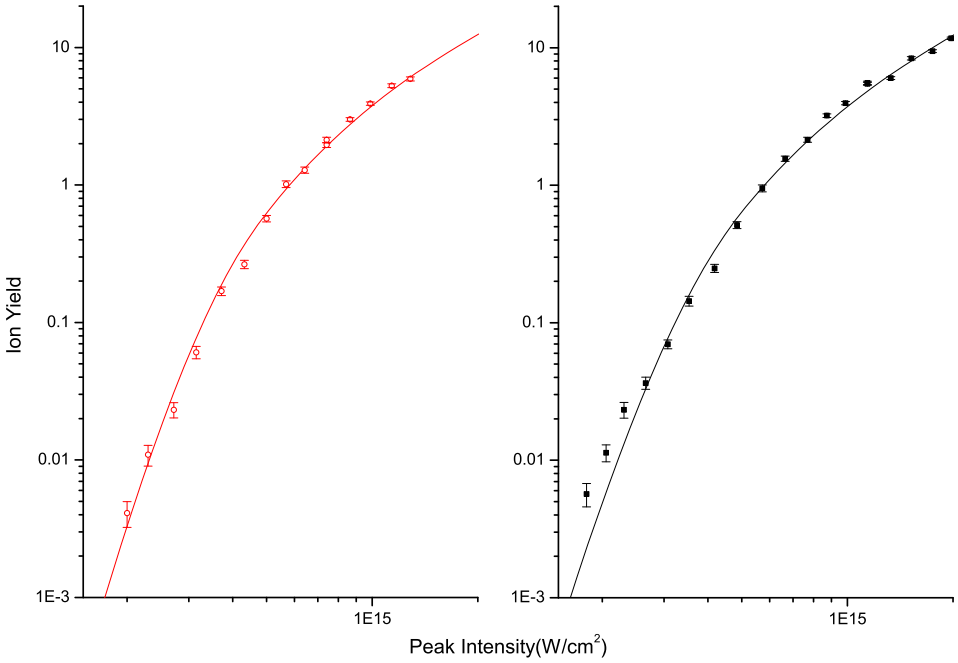

Figure 4.12: Experimental data together with the ADK fit.

4.4 Conclusions

The importance of rescattering in strong field interactions with negative ions has been an open question for some time now due considerations which suggest that, compared with atoms, this mechanism would be suppressed. These include the short survival time of negative ions in intense pulse and the absence of Coulomb focusing. Recent theoretical work has shown that rescattering will occur if an intact negative ion can be exposed to a sufficiently strong field ([9], [10], [3], [11], [4]).

The work presented in this thesis provides convincing evidence for a direct double detachment process which is consistent with the rescattering

mechanism. Recent quantum analysis of plateau structures in strong-field processes for short-range potentials and numerical results for the ATD spectrum of F^- has shown a support for the interpretation of our results in terms of the rescattering mechanism [12].

4.5 Future Experiments

There are relatively few groups working with negative ions and their interaction with intense laser fields, therefore a lot of work remains to be done. The availability of ultra-short pulses ($\approx 5fs$) provide and ideal opportunity for immersing a negative ion in a strong field before an electron is detached. Studies of the effect of the carrier-envelope phase of such pulses is currently undergoing study in the ionization of atoms [13]. This has been maturated by the efforts being made to produce attosecond pulses by the HHG process. Similar work for negative ions would be an important contribution to the understanding of these processes. Theoretical work [14] has predicted that is experimentally feasible the observation of HHG in negative ions. This type of experiment would help to understand better, for example, the role of the Coulomb potential in the production of HHG.

References

[1] G. D. Gillen, M. A.Walker, and L. D. vanWoerkom, Phys. Rev. A **64**, 043413 (2001).

[2] M. R. Cervenan and N. R. Isenor, Opt. Commun. **13**, 175 (1975).

[3] V. N. Ostrovsky, J. Phys. B: At. Mol. Opt. Phys. **36**, 2647 (2003).

[4] G. L. Kamta and A. F. Starace, Phys. Rev. A **68**, 043413 (2003).

[5] G. F. Gribakin and M. Y. Kuchiev, Phys. Rev. A **55**, 3760 (1996).

[6] B. Chang, P. R. Bolton, and D. N. Fittinghoff, Phys. Rev. A **47**, 4193 (1993).

[7] M. D. Perry, O. L. Landen, A. Szoke, and E. M. Campbell, Phys. Rev. A **37**, 417 (1988).

[8] J. Pedregosa-Gutierrez *et al.*, Phys. Rev. Lett. **93**, 223001 (2004).

[9] D. B. Milosevic, A. Gazibegovic, and W. Becker, Phys. Rev. A **68**, 05070R (2003).

[10] M. Frolov, N. L. Manakov, E. A.Pronin, and A. F. Starace, J. Phys. B: At. Mol. Opt. Phys. **36**, L419 (2003).

[11] M. V. Frolov, N. L. Manakov, E. A. Pronin, and A. F. Starace, Phys. Rev. Lett. **91**, 053003 (2003).

[12] M. V. Frolov, A. V. Flegel, N. L. Manakov, and A. F. Starace, J. Phys. B: At. Mol. Opt. Phys. **38**, L375L382 (2005).

[13] X. Liu *et al.*, Phys. Rev. Lett. **93**, 263001 (2004).

[14] V. N. Ostrovsky and J. B. Greenwood, J. Phys. B: At. Mol. Opt. Phys. **38**, 1867 (2005).

Part II

Linear Electrostatic Ion Beam Trap

Preface

The search for methods of selectively breaking molecular bonds has been a prevailing concern in the quest for control of chemical reactions. Photochemistry has shown that certain reactions can be strongly influenced by molecular excitation using light of specific wavelengths. However, the selectivity of these methods to form specific radical species is limited as the absorbed photon energy is usually quickly redistributed throughout the molecule.

Femtosecond laser technology, now provides excitation timescales which are of the same magnitude or shorter than vibrational motion in molecules. When this is coupled with recent advances in the control of wavelength, phase, intensity and polarization of the light during a femtosecond laser pulse, the multi-dimensional potential energy landscape of molecules can be shaped so that bonds can be selectively broken. This has been elegantly demonstrated by experiments using evolutionary feedback algorithms to optimise the laser pulse parameters for a particular molecular fragmentation or chemical product[1].

Despite these advances, there are still many fundamental questions of how intense, ultrashort laser pulses enhance or suppress molecular dissociation and ionization. This is due to the fact that there are many dynamical processes in even the simplest molecules. It has proved experimentally challenging to disentangle these mechanisms as they are highly dependent on the initial in the design, construction, software development and testing of a linear electrostatic ion beam trap with the ultimate goal of trapping molecular ions long enough for them to reach their ground vibrational state; in particular, with the initial objective of providing definitive experimental data on the ultrashort, intense field dissociation of HD^+ through vibrational

cooling of the ions in an electrostatic trap prior to application of the laser.

Chapter 5

Linear Electrostatic Ion Beam Trap

5.1 Introduction

The physics of trapped ions has evolved considerably from the invention of the first ion trap about 50 years ago [2]. Today, schemes for trapping and observing ions are still being developed. These techniques have led to a broad range of results in various fields of physics, such as atomic, molecular, optical and nuclear physics, nonlinear dynamics, single component plasmas, mass spectrometry, biophysics, quantum computation and others. Ion traps are designed to store ions for as long time as possible and in such a way that the particles are well localized in space.

The reason of the existence for an ion trap are several. A fundamental reason is based in Heisenberg's uncertainty principle: to increase an energy resolution measurement, it has to be done for longer times ($\Delta t \Delta E > \frac{\hbar}{2}$). Other possibilities are the measurement of lifetimes of metastables states of an atom, or of a radioactive isotope. Also, storing a molecule for a long time will allow the cooling of internal degrees of freedom (such as electronic, vibrational or rotational excitations of molecules). On the other hand, it is pos-

sible to influence the trapped particles with a well-controlled perturbation, so that effects of a given perturbation can be monitored under well-defined conditions.

It is possible to divide the world of particle storage devices into two different groups: those where ions are localized in space, and their kinetic energy is in the sub-keV regime (Paul, Penning, Kingdon traps and their variants), and those where particles move at very high velocity and circulate in a circular vacuum tube (storage rings). In the sub-keV regime, the ions are confined in a small region of space using a combination of electrostatic and magnetostatic or time-dependent fields. The trajectories of the ions are usually complex functions of these fields although the motion is, in general, well understood. On the other hand, the second type of ion traps use a combination of magnetic steering and focusing fields that generates a beam with a well-defined kinetic energy and direction in space, allowing for highly efficient detection techniques of the reaction products.

In the following, I will concentrate just on a recently developed linear electrostatic ion beam trap. Several experiments have already been performed using linear electrostatic traps. For example, the first experimental evidence for the presence of electronic metastable states in small carbon clusters were obtained by using these type of traps [3], as well as the measurement of several metastable lifetimes, such as $He^-(1s2s2p^4P_{5/2}\ ;\ 343 \pm 10\mu s)$ [4], and of $Be^-(2s2p^2\ ^4P_{3/2}\ ;\ 47.07 \pm 0.12\mu s$, a factor of 40 better in accuracy than the previous result determined in a heavy-ion storage ring). Experiments of electron-impact detachment of internally cold C_n^- and Al_n^- clusters [5] or measurements of the kinetic-energy release after dissociative charge transfer of vibrationally cold HeH^+ [6] are more examples.
For a recent review of circular and linear electrostatic ion beam traps see [7].

5.2 Concept

It is well known that the motion of charged particles in an electrostatic field is similar to the propagation of light in a medium where the index of refraction is proportional to the square root of the electric potential. Such an analogy is often used for description of ion beam transport. Based on such an analogy, several traps have been recently developed ([8],[9]). In the absence of a better name, the acronym of LEIBT (Linear Electrostatic Ion Beam Trap) will be use in this thesis. A LEIBT is based on the same principle as the equivalent "photon storage" device which is known as an optical resonator, see figure 5.1a). In an optical resonator, a beam of photons can be trapped between two spherical mirrors if (for a symmetrical mirror system):

$$L/4 < f < \infty \tag{5.1}$$

where L is the distance between the two mirrors, and $f = (Radius/2)$ is the focal length. The implementation directly from an optical resonator has been done [10]. Other groups ([8], [9]) have taken the classic analogy a step further, by decomposing each spherical mirror into a lens and a planar mirror, see figure 5.1 b). By doing this, a more straightforward implementation of the photonic model to the ion optics case can be achieved. A schematic design can be seen in figure 5.1 c).

5.3 Ion beam Dynamics inside a LEIBT

The first experimental evidence of trapping ions in a LEIBT can be found in two different papers from the same year (1997): in [11] where they trapped DNA and in [9], where a beam of Ar^+ with a kinetic energy of 4.2keV

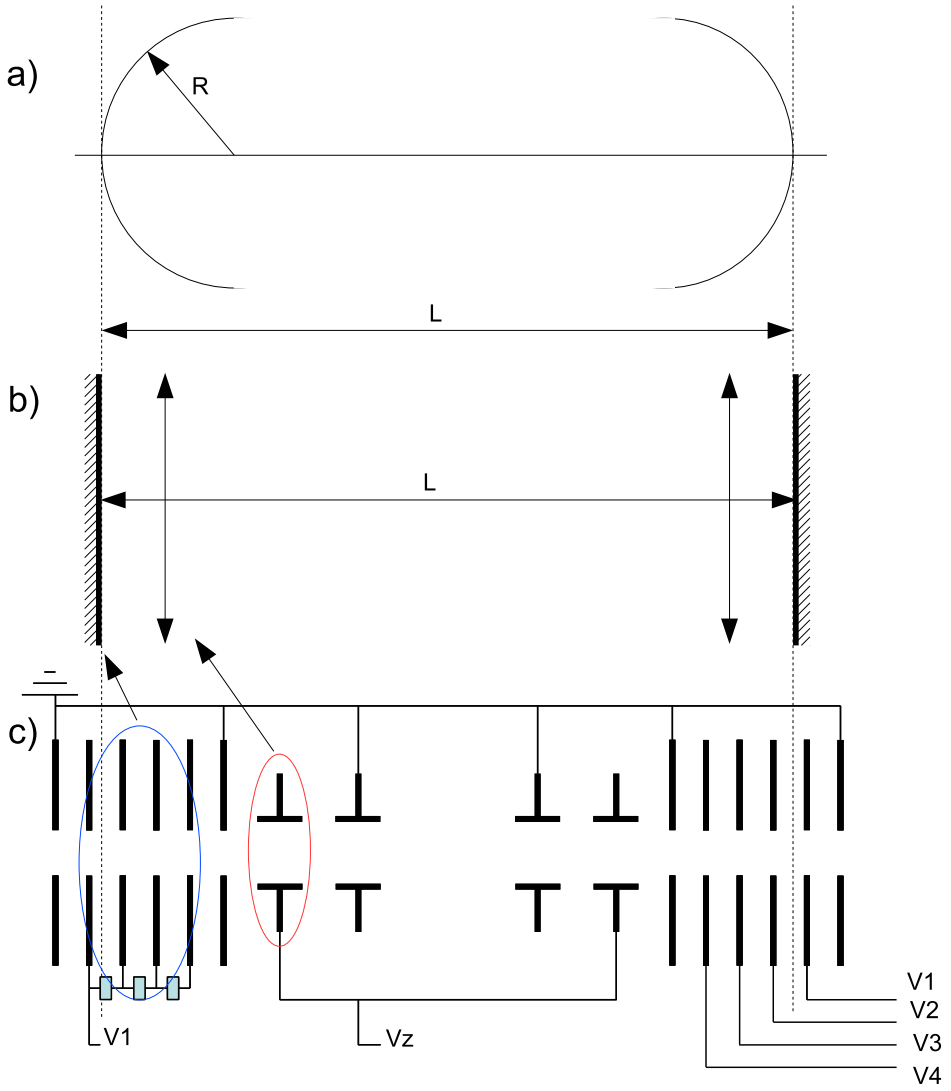

Figure 5.1: Transition from optical resonator to ion beam trap. a)Optical resonator; b)Decomposition in simple elements; c)Scheme of a linear ion beam trap.

was used[1]. In [9], bunches of ions with a temporal extension of $1 - 100\mu s$ were created with the help of an electrostatic chopper situated before the 45° bending magnet. The injection into the trap was realized by grounding

[1]I will take [9] as a reference point rather than [11] as their motivations for the development of the ion trap are closer to our own research interests.

the entrance set of potentials, while leaving the exit high. This reflected the bunch and before the ions returned to the entrance side, the potentials of the electrodes were rapidly ($\sim 100ns$) raised so that the ion bunch was confined between the two electrostatic mirrors. The set-up of [9] allows the monitoring of the evolution of the bunch by using a microchannel-plate (MCP) detector and a cylindrical pickup electrode located in the center of the trap. From the data obtained from these two detectors it was possible to obtain the trapping efficiency ϵ, defined as the ratio between the number of ions initially trapped N_t and the number of ions injected, N_I.

The signal (number of ions) counted by the MCP in a time interval δt can be written as:

$$S(t) = \alpha N(t)\delta t \tag{5.2}$$

where α is a constant of proportionality that accounts for the neutralization process, the MCP efficiency, and the geometrical acceptance of the detector, and $N(t)$ is the number of trapped ions at time t. So it is possible to define a relative efficiency ϵ_r as:

$$\epsilon_r = \alpha\epsilon = \alpha\frac{N(t=0)}{N_I} = \frac{S(t=0)}{\triangle t N_I} \tag{5.3}$$

The value for $S(t=0)$ was found by extrapolation of the decay curve and the number of injected ions could be obtained from the signal induced in the pickup ring. Figure 5.2, shows the value of ϵ_r as a function of V_z. This graph shows that two different islands of stability exist.

The two trapping regions observed in the figure 5.2 have some important differences. The obvious one is the efficiency with which the ions are trapped. But a more subtle difference exists in the behavior of the ion bunch inside the trap. In the first island, the bunch spreads with time ($L(t_2) > L(t_1); t_2 \gg t_1$), while in the second island the size of the bunch remains stable under certain circumstances ($L(t_2) \sim L(t_1); t_2 \gg t_1$). So, from now on, we will call them *diffusion* and *synchronization* regions.

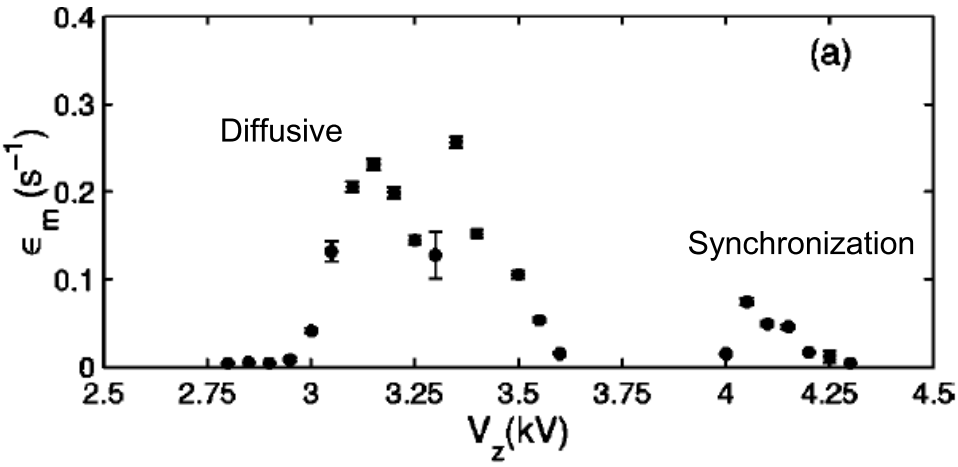

Figure 5.2: Measured relative trapping efficiency ϵ_r versus V_z. From [9](Ar^+,4.2keV)

5.3.1 Diffusion

There are several reasons why a trapped ion bunch will spread. First, the ions will de-phase due to the intrinsic spread of period times which exist because the trapped ions move on trajectories with slightly different oscillation times. The period is characteristic of the trap configuration and the injection conditions (the exact trajectory that the ion follows in the trap). Second, the ions have an initial energy spread as they emerge from the ion source thus creating a wider range of oscillation times. Third, the trapped ions are subjected to *external* perturbations due to scattering on the residual gas and noise on the applied electrode potentials. Finally, the Coulomb repulsion between the ions leads to an *internal* perturbation of their motion and hence affects the diffusion pattern.

With neither external nor internal perturbations, the ions in these trapping region are characterized by a distribution of oscillation times with constant mean and width, hence the trapped ions behave as if they were a closed system where each ion preserves its initial oscillation time. This "coherent" model provided a excellent fit to the experimental data obtained in [12], see

figure 5.3.

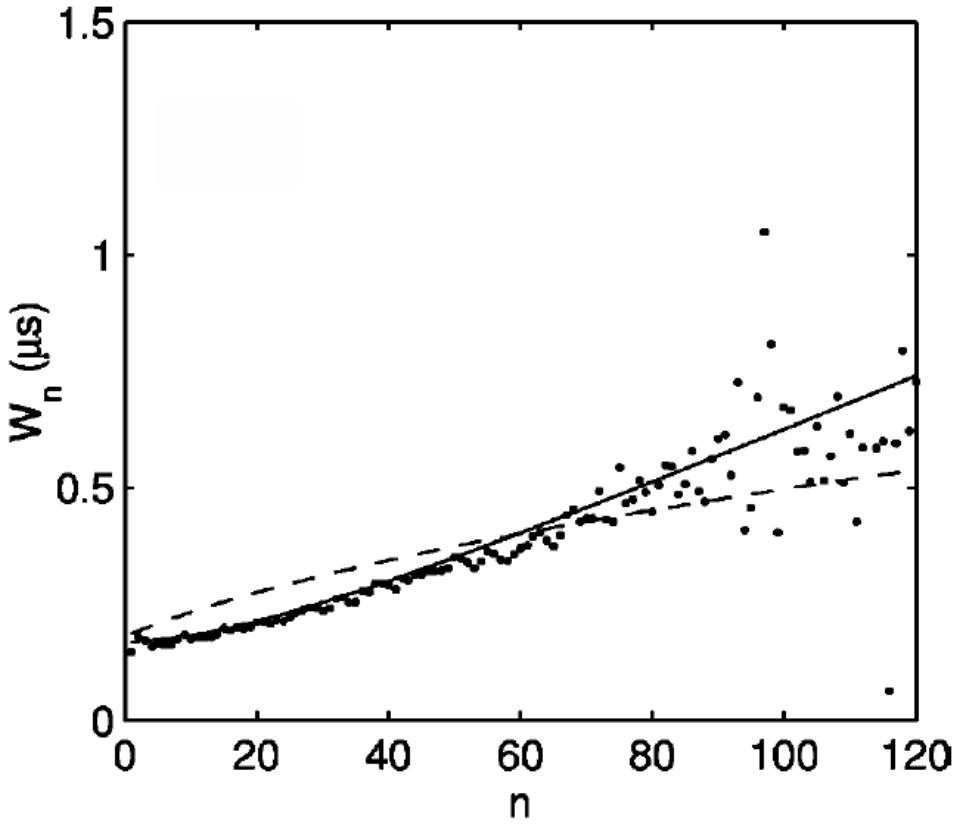

Figure 5.3: Evolution of a bunch of 4.2keV Ar^+ with initial width of $\sim$ 170ns in the diffusive mode as a function of the number of oscillations n. The dots represent the bunch with W_n. Solid line: fit to the data using the coherent model; Dotted line: fit assuming that the ions interact with external perturbations. The dotte From [12]

5.3.2 Synchronization

There is a region where the width of the ion-bunch does not experience diffusion. In this regime, the bunch spreads during the initial oscillations but after that the width stabilizes. There is a intermediate region where some large jumps have been observed, but beyond this region, the width remains essentially constant, although the number of ions in the bunch decreases exponentially with time, see figure 5.4.

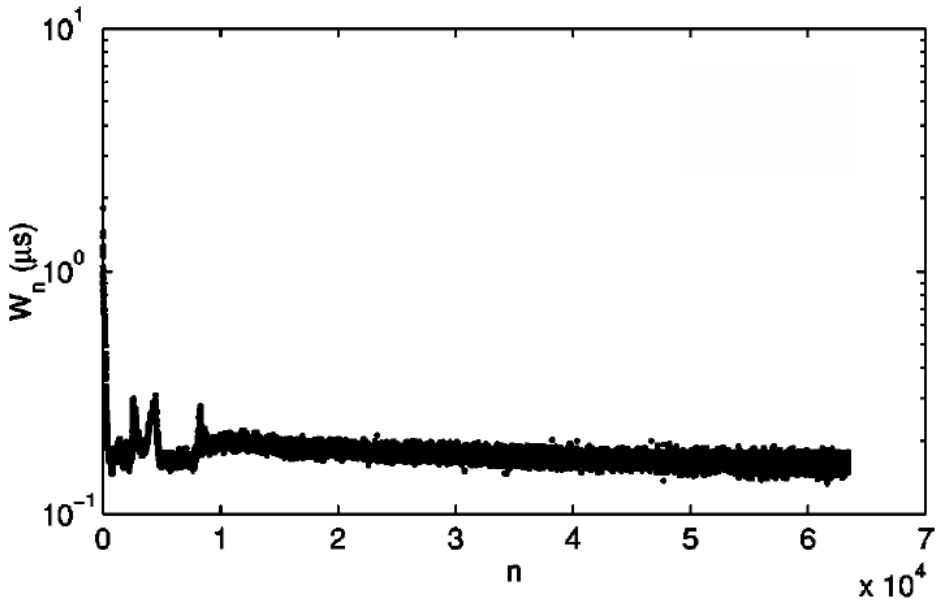

Figure 5.4: Example of the evolution of the bunch width of 4.2keV Ar^+ with initial width of $\sim 0.9\mu s$ as a function of the number of oscillations n in the synchronization mode. From [12]

5.4 Synchronization: Theoretical Models

The first study of the self-bunching observations in a LEIBT was done by H. B. Pedersen [12], who shows that this stability can not be explained by interactions that are stochastic in nature, such as residual gas collisions or noise on the mirror electrodes in the trap. In order to explain the unexpected synchronization effect observed when a bunch of ions oscillates between two mirrors in an electrostatic ion beam trap, several models were developed.

5.4.1 Mean Field Approximation

In this model, developed by Pederson et. al.[12], the motion of a test ion of mass M amu and charge q, and a sphere of radius R uniformly filled with N identical ions are moving together in a potential described by equation 5.4.1

$$U(z) = \begin{cases} 0 & \text{if } |z| \leq L \\ \alpha_w(|z| - L) & \text{if } |z| > L \end{cases}$$

where $2L$, is the length of the field-free region and α_w is the slope of the potential walls, see figure 5.5.

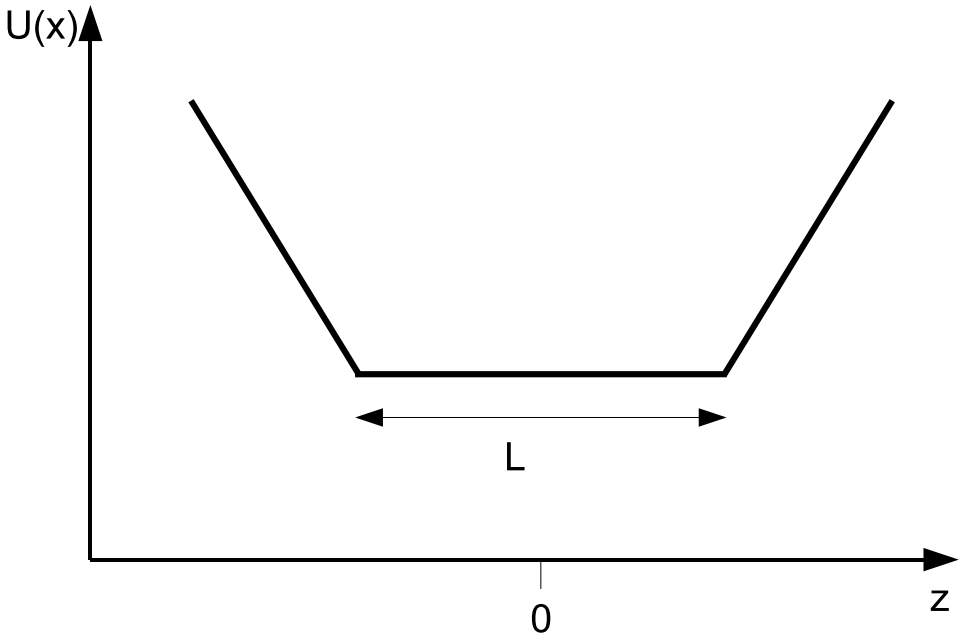

Figure 5.5: The one-dimensional potential.

In such a potential, the oscillation period for fast particles is longer than for slow particles if $\alpha_w < 2E/(qL)$. The explanation is that the fast particles "climb" higher on the potential wall, and the extra time spent in this region is larger than the time difference between slow and fast particles in the field-free region. A convenient parameter to characterize the motion of a single ion in this potential is the logarithmic derivative of the oscillation time T with respect to the ion energy E:

$$\beta = \frac{1}{T}\frac{dT}{dE} \tag{5.4}$$

and is related to the slope of the potential walls by:

$$\beta = \frac{1}{2E}\frac{1 - L(q/E)(\alpha_w/2)}{1 + L(q/E)(\alpha_w/2)} \tag{5.5}$$

The advantage is that while the slope α_w is bounded between $\infty > \alpha_w > 0$, β takes values in the interval $-1 \leq 2E\beta \leq 1$. All the properties of the single ion motion can be expressed through β, like the oscillation time:

$$T(\beta) = \sqrt{\frac{M}{2E}} \frac{4L}{1 - 2E\beta} \tag{5.6}$$

where M is the ion mass. Another important feature is that a small change in the energy is transformed directly to a change in oscillation time:

$$\triangle T = \triangle E \left| \frac{dT}{dE} \right| = \triangle E |\beta| T(\beta) \tag{5.7}$$

The objective of this model is to understand the behavior of a single ion in the field created by all the other ions which are represented by a charged sphere. The force between the ion and the sphere is given by (assuming $q = |e|$):

$$F_m(\triangle z) = \frac{e^2}{4\pi\epsilon_0} \frac{N}{R^2} \begin{cases} \frac{\triangle z}{R} & \text{if } |\triangle z| \leq L \\ (\frac{R}{\triangle z})^2 & \text{if } |\triangle z| > L \end{cases}$$

where $\triangle z$ is the separation between the test ion and the center of the sphere. In the real 3D potential, the ions are compressed radially by the focal lens and longitudinal by the electrostatic mirrors. In order to take into account this behavior, the radius of the sphere is a function of its velocity:

$$R = R_{min} + (R_0 - R_{min}) \frac{v}{v_0} \tag{5.8}$$

where R_{min} is the minimum possible radius, R_0 the radius of the sphere in the field-free region, v the velocity of the sphere, and v_0 its initial velocity. The Newtonian equations were solved for the case of the experimental parameters in [12]. The results are shown in figure 5.6, where $2E \cdot \beta = 0.5$ and the initial kinetic energy difference ($\triangle E_0 = 10eV$) were kept constant and the value of N was changed, effectively changing the density in the ion beam. With $N = 10^3$, the test ion and the sphere increase their separation

with time, as you expect in the diffusive mode. But when the intensity is increased to $N = 10^4$, a highly correlated behavior is found. There exists a maximum separation between both, a phenomenon which has been observed experimentally. When the ions density is even higher, their relative motion becomes more complex, where they lock in a complicate pattern, but their separation remain bounded.

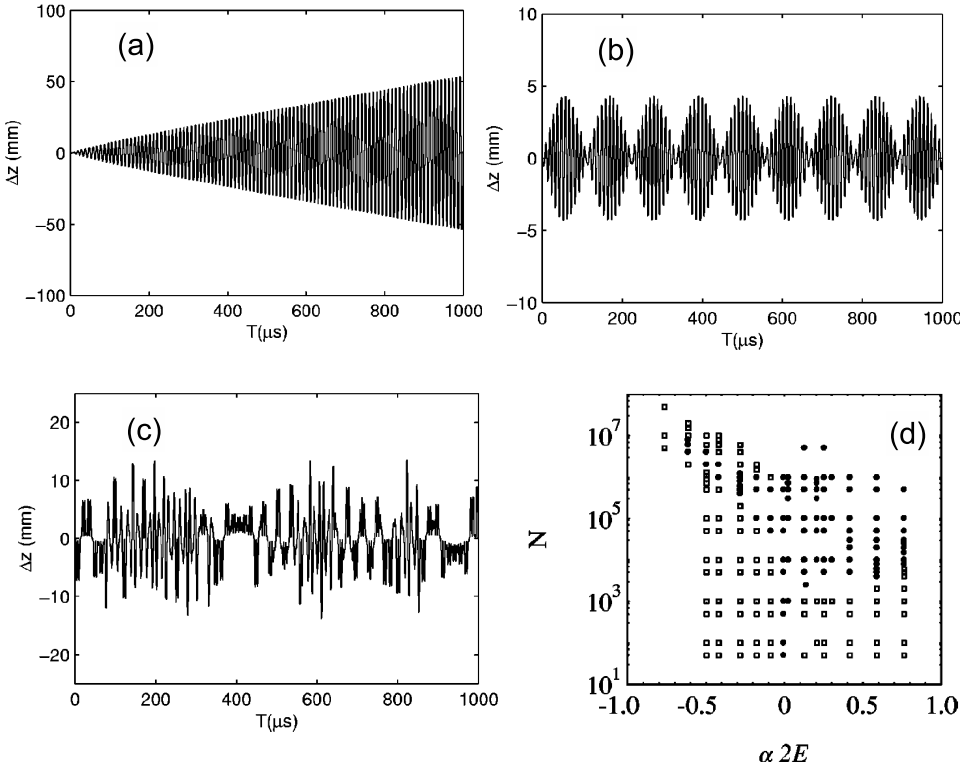

Figure 5.6: The first three graphs are plots of the separation $\triangle z$ as a function of time, T for different N, where $2E \cdot \beta = 0.5$ and $\triangle E_0 = 10eV$ are keep constant: a)$N = 10^3$, b)$N = 10^4$, c)$N = 10^6$. The fourth graph, d) is a plot of the number of ions N vs $2E \cdot \beta$, where open square represents points where diffusion was observed, and filled circles represent points where synchronization was found.

A systematic calculation of the diffusive or non-diffusive behavior for various values of β and N, for a fixed value of $\triangle E_0 = 10eV$ leads to figure 5.6d). Diffusion is strongly suppressed for $\beta = 0$, corresponding to $\frac{dT}{dE} = 0$, meaning that the period oscillation T of the particles is independent of

small variation of their kinetic energies E. Synchronization is predominant for $\beta > 0$ corresponding to the case where the fastest particles have a longer period.

This study shows that synchronization occurs due to the coulomb interaction of the ions inside the bunch under certain conditions. The condition $\beta > 0$ was found to favour the synchronization. In this situation, the fastest particles will be in the rear of the bunch (longer oscillations periods), but when the slow particles are starting to "come down" the potential, the fastest particles push the slow ones. A consequence of this is that the energy of the ions in the bunch is kept constant within certain limits, keeping the size of the bunch controlled. But for this mechanism to work, a minimum density is required. An analytical expression to calculate this minimum density was obtained using the negative effective mass approach.

5.4.2 Negative Effective Mass

The conclusions obtained in the last section were the result of a series of numerical calculations. And for that reason it was not possible to give an explicit expression for the condition for synchronization. Strasser et. al. [13] realized that the synchronization effect could be explained as a negative effective mass instability [14]. Using this theory it is possible to derive simple necessary conditions for the existence of the bunching phenomenon. The full demonstration involves mapping matrices which propagate the system in the phase space producing a Poincaré map at the center of the trap to follow the particle motion. They found that the lower limit for the density ρ, in order to obtain synchronization, can be written as:

$$\rho > \frac{4\eta\epsilon_0 p_0^2}{mqR_0^2} \tag{5.9}$$

where R_0 is the radius of a homogeneously charged sphere, q is the charge of a single ion in the bunch, ϵ_0 is the vacuum permittivity and η is

$$\eta = \frac{|P_0|}{T}\frac{dT}{d|P_0|} \tag{5.10}$$

where P_0 is the initial center-of-mass momentum and T is the half-oscillation time.

They also demonstrated the same the condition observed by Pederson et. al. [12]:

$$\frac{dT}{d|P_0|} > 0 \tag{5.11}$$

We conclude this section by mentioning that the so-called negative mass instability was first introduced in 1959 by Nielsen, Sessler and Symon [15] for relativistic circular accelerator or storage rings. This effect has been observed only in accelerators working at relativistic energies. However, unlike the large accelerators where the negative mass instability is a nuisance, it leads to an interesting application in the case of LEIBTs.

References

[1] T. Brixner and G. Gerber, ChemPhysChem. **4**, 418 (2003).

[2] W. Paul, in *Nobel Lecture, Physics 19811990*, edited by ed G Ekspong (Singapore: World Scientific, ADDRESS, 1993).

[3] A. Naaman *et al.*, J. Chem. Phys **113**, 4662 (2000).

[4] A. Wolf *et al.*, Phys, Rev. A **59**, 267 (1999).

[5] A. Diner *et al.*, Phys, Rev. Lett. **93**, 063402 (2004).

[6] D. Strasser *et al.*, Phys, Rev. A **61**, 060705 (2000).

[7] L. H. Andersen, O. Heber, and D. Zajfman, J. Phys. B: At. Mol. Opt. Phys. **37**, R57 (2004).

[8] H. F. Krause, C. R. Vane, and S. Datz, in *Proc. 16th Int. Conf. On Application of Accelerators in Research and Industry*, edited by ed J L Duggan and I. L. Morgan (AIP Conf. vol 576, New York: AIP, 2001).

[9] M. Dahan *et al.*, Rev. Sci. Instrum. **69**, 76 (1998).

[10] H. T. Schmidt, H. Cederquist, J. Jensen, and A. Fardi, Nuc. Instr. Meth. Phys. Res. B **173**, 523 (2001).

[11] W. H. Benner, Anal. Chem. **69**, 4162 (1997).

[12] H.B. Pedersen, D. Strasser, O. Heber, M.L. Rappaport, and D. Zajfman, Phys. Rev. A **65**, 042704 (2002).

[13] D. Strasser, O. Heber, S. Goldberg, and D. Zajfam, J. Phys. B: At. Mol. Opt. Phys. **36**, 953 (2003).

[14] U. Smilansky, in *Mesoscopic Quantum Physics*, edited by ed E. Akkermans, G. Montambaux, J. L. Pichard, and J. Zinn-Justin (Les Houches Sessions, Amsternam: Elsevier, 1994).

[15] C. E. Nielsen, A. M. Sessleer, and K. R. Symon, High Energy Accelerators and Instrumentation(CERN, Genova) (1959).

Chapter 6

QUB electrostatic ion trap: Simulations

In order to increase the lifetime and its trapping efficiency, a full simulation of the LEIBT was done using the charged particle optics modelling software SIMION3D7.0.

6.1 SIMION3D7.0

SIMION3D7.0 is a native Win32 ion optics simulation program that models ion optics problems 2D symmetrical and/or 3D asymmetrical electrostatic and/or magnetic potential arrays. Complex systems or even entire instruments can be modelled. The program can both solve the Laplace equation for a specific potential configuration in space and propagate ions on the computed potential grid. The program uses a fourth-order Runge-Kutta method to solve the Newtonian equation of motion.

A major advantage of SIMION versus other similar software is that it allows you to label different parts of your geometry in such a way that after the initial refining, you can change the values of the voltage of every part independently and the field lines are recalculated nearly in real time. An-

other key feature is the existence of .PRG files through which it is possible to fully control the flying ions, allowing "virtual" experiments to be performed. For further information, the reader can consult SIMION's website: "http://www.simion.com/"

6.2 Are we in the correct path?

In order to confirm our methodology, SIMION was used to simulate previous experimental results. Figure 6.1 shows the ion trap as presented in SIMION. Two methods were used to determine the trapping probability, one fast and

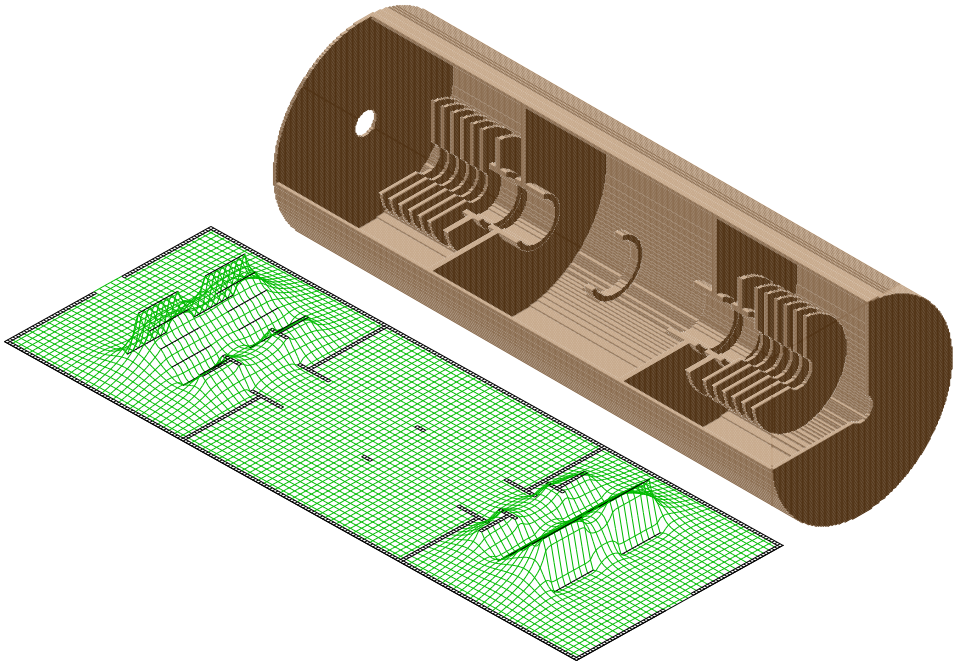

Figure 6.1: Visualization of the potential arrays simulated in SIMION.

one slow but rigorous. Let's start with by explaining the rigorous approach. The first approach consisted of finding the stability function, a function that takes a value of 1 if the ion remains trapped after $500\mu s$ or a zero if the ion

dies before that time. Mathematically

$$S(\overrightarrow{g_i}, V_z) = \begin{cases} 0 & \text{if } t_{flying} < 500\mu s \\ 1 & \text{if } t_{flying} \geq 500\mu s \end{cases}$$

where $\overrightarrow{g_i} = (r_i, vr_i, v\theta_i)$ fully characterizes a trajectory of an ion with kinetic energy, E_k, inside the trap. The stability function can be obtained using SIMION. A single ion is let fly with energy E_k at a specific position in the 3-dimensional space $\overrightarrow{g_i}$. The stability of this trajectory was determined using the criterion "was still flying or not after $500\mu s$". As the simulation was done in a background gas free environment, the *death* of an ion was defined as a collision with an element of the trap. Once a trajectory had been assigned 0 or 1, $\overrightarrow{g_i}$ was changed and an ion started flying again. This way, by scanning $(r_i, vr_i, v\theta_i)$, the function $S(\overrightarrow{g_i}, Vz)$ was found for a specific value of V_z. This is a 4-D problem, hence the slowness of the method. Having obtained the stability function, a Monte-Carlo type simulation was performed . For that, a FORTRAN code was written, where a set of N initial $\overrightarrow{g_i}$ was randomly generated . The code checked if the set $(r_i, vr_i, v\theta_i)$ corresponded to a stable trajectory or not. Just by counting how many ions had *fallen* in a stable trajectory, N_T, the trapping efficiency was obtained

$$\epsilon\ (V_z) = \frac{1}{N} \sum_{i=1}^{i=N} S(g_i, V_z) = \frac{N_T}{N}$$

To represent a realistic beam, random numbers were generated for normal distributions with a specific mean and standard deviation. The FORTRAN code runs in less than 5s, but the SIMION simulation takes more than a week in a relatively fast machine (2.8GHz, 1Gb of RAM) to compute the stability function. As it was desirable to study other parameters such as different geometries and beam energies, a faster method was developed.

The second method involved inverssing the order of the calculation. In the slow method SIMION was used to determine if a trajectory was or was

not stable by scanning the phase-space to find $S(\overrightarrow{g_i}, V_z)$. Afterwards, a large (N=10^6-10^8) number of random $\overrightarrow{g_i}$, which represented ions initial positions, were generated. With S, we were able to check if they corresponded to trap or not trap ions. This time the ions were randomly generated in SIMION and then they were propagated all at the same time and finally, checked how many were left after $500\mu s$. This was faster, around 30 minutes. However, with this faster method, you can not simulate as many ions, usually we generate just 100. The results of both type of simulations together with the experimental results of Zajfman [1] can be seen in figure 6.2, where the curves have been normalized to the small peak of the experimental values. Even if the result is not perfect, clearly the simulations reproduce the overall experimental results. The "long" simulations better reproduce the relative trapping efficiency between the regions. It is worth noticing the difference between the two simulations for the same beam energy, 4.2KeV. The reason for this discrepancy could be in the different methods used to randomize the ions. While in the FORTRAN code, it was possible to use a subroutine to generate a Gaussian distribution, in SIMION, the distribution is uniformly distributed. In order to try to get a better fit to the experimental curves, different energy beams were tried. For example, for a 4.0KeV beam, it fits the first peak, while the second one is shifted. The opposite happens for a 4.1KeV.

Overall, the results of the simulations predict two islands of stability as obtained experimentally. This is an indication that the use of SIMION as a tool to study the behavior of the ions in the trap is justified.

6.3 Improving the Design

For our experiments we would like to design a device with the maximum trapping efficiency. To achieve this we need to identify the limiting factors. The ion beam injected in the trap has an angular dispersion, so the angular

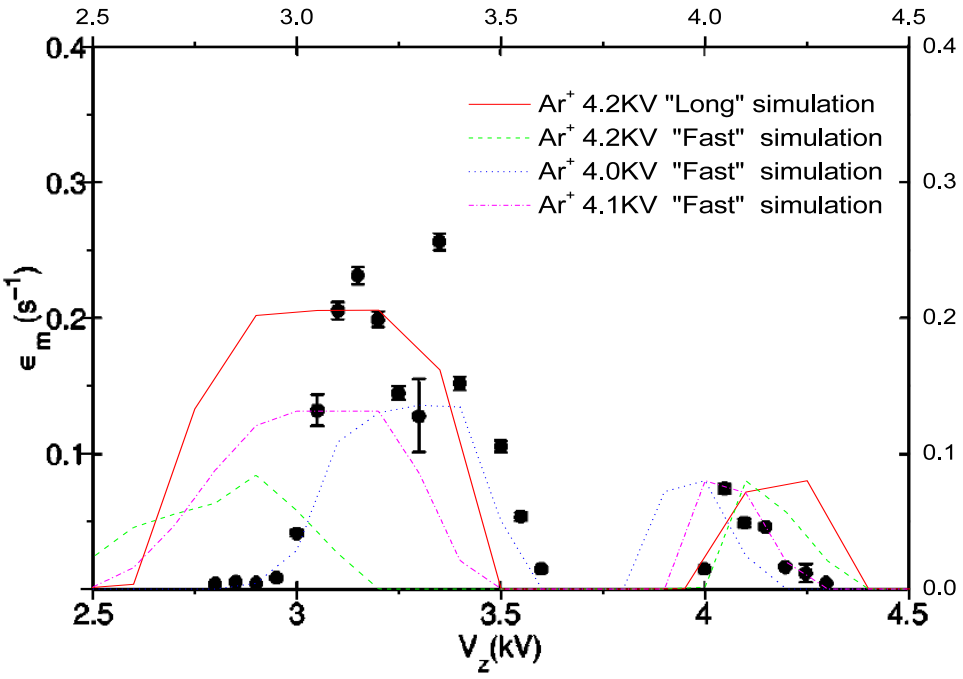

Figure 6.2: Relative efficiency as a function of the potential on the Einzel electrodes, V_z. Circles represents the experimental points.

acceptance is the key parameter. There are two ways to increase the angular acceptance: by making the trap shorter and/or wider. This view has been recently confirmed experimentally by D. Attia et. al. [2]. They showed that in their existing experimental setup, the phase space of the trap is filled very soon after injection. They demonstrated the existence of a correlation between the area of the transverse phase space and the measured lifetime. A consequence of their result is that the lifetime in the trap will also be a function of the trap length. In other words, a shorter and wider trap will increase the available phase-space.

The trapping efficiency curves for a new design were determined. In order to compare both traps, figure 6.3 shows some curves for the classic trap and for the QUB trap[1]. The two curves corresponding to the QUB

[1]From now on, I will use the term *classic* to refer to the Zajfman's [3] geometry and QUB to refer our new dimensions.

trap are done for the same plate voltage and for a voltage corresponding to the same potential on the trap axis. The reason behind this is that for a wider aperture, you need higher voltage to achieve the same voltage on axis.

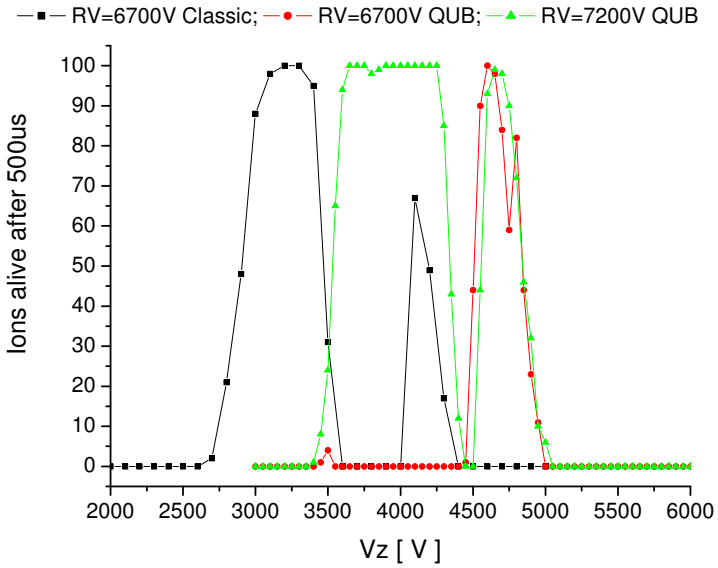

Figure 6.3: Number of ions still flying after $500\mu s$ in the simulations versus the potential applied in the Einzel lenses, V_z.

From figure 6.3 we can see that the peak for $RV = 7200V$, presents the two expected peaks. The bunching peak is 1.5 times bigger and the diffusion peak is wider and totally saturated in the QUB trap. Figure 6.3 shows how the new design performs better in this type of simulation.

The calculation of the acceptance angle for the four different cases, corresponding to the bunching and diffusive peaks for $RV = 6.7KV$ for the classic trap and for the $RV = 7.0KV$ for the QUB trap, are shown in figure 6.4. It is evident that in both regimes, diffusive and bunching, the QUB design traps more efficiently, especially in the synchronization mode.

This design was chosen for the QUB trap.

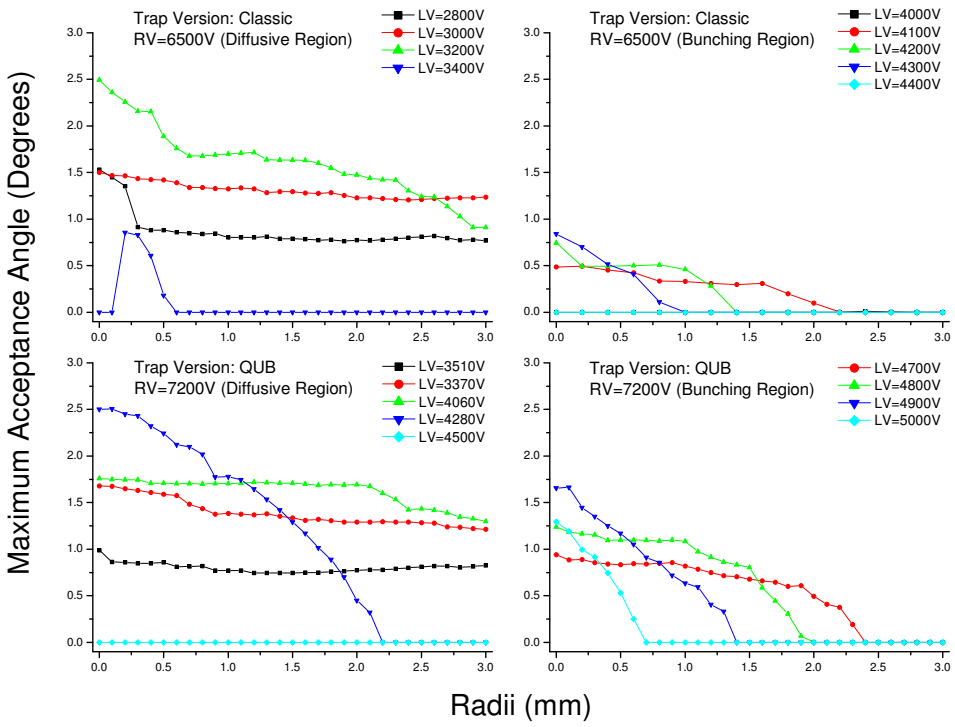

Figure 6.4: Maximum acceptance angle as a function of the radial distance from the axis of the trap for different set-ups.

6.4 Cooling Molecules

Our primary motivation for building an ion trap was to produce molecular ions in their ground vibrational state. For instance this could allow strong-filed dissociation of HD^+ to be studied. The reason for not choosing H_2^+ is that the lifetime of the first vibrational state ($\nu = 1$) is around 10^6s. In contrast, HD^+ which possesses a permanent dipole moment has a more manageable lifetime of $60ms$ [4]. A simple calculation can be done in order to study how the vibrational population of a trapped bunch of HD^+ would evolve.

For HD^+, as for any infrared active molecular ion, the time evolution of the vibrational populations $p_\nu(t)$ (ν indicates vibrational state) during the storage time is completely determined by the initial populations of the vibra-

tional states upon production and injection, $p_\nu(t=0)$, and by the radiative lifetime τ_ν of the different levels. The recursive rate equations describing the time evolution for each level ν are of the form [4]

$$\frac{dp_\nu}{dt} = \frac{1}{\tau_{\nu+1}} p_{\nu+1}(t) - \frac{1}{\tau_\nu} p_\nu(t) \tag{6.1}$$

If the initial population for levels above ν_{max} is assumed to be negligible ($p_\nu(0) = 0$ for $\nu > \nu_{max}$), the general solution of the set of rate equations is

$$p_\nu(t) = a_{vv} e^{-t/\tau_\nu} + \sum_{\nu'=\nu+1}^{\nu_{max}} a_{vv'} e^{-t/\tau_{\nu'}} + b_\nu \tag{6.2}$$

where $a_{vv'}$ and b_ν are time-independent constants. By inserting the general solution in equation 6.1 and assuming $\tau_\nu \neq \tau_{\nu+1}$, it is possible to obtain an iterative expression for $a_{vv'}$

$$a_{vv} = p_\nu(0) - \sum_{\nu'=\nu+1}^{\nu_{max}} a_{vv'} \quad \text{for } 0 \leq \nu \leq \nu_{max} \tag{6.3}$$

$$a_{vv'} = \frac{a_{v+1,v'}}{\tau_{\nu+1}(1/\tau_\nu - 1/\tau_{\nu'})} \quad \text{for } \nu+1 \leq \nu' \leq \nu_{max} \tag{6.4}$$

and b_ν.

If we take the experimental radiative lifetime and initial population of HD^+ from [4], using a home-made FORTRAN code to calculate the temporal evolution of the vibrational population, we find figure 6.5.

We see how at $t = 0$ there are a large number of states populated, so by simply waiting for a fixed period of time after the trap has been filled with ions, we have a powerful way of controlling a range of dissociation processes in HD^+, allowing to unambiguously identify the vibrational states involved, making comparison with theoretical models more transparent.

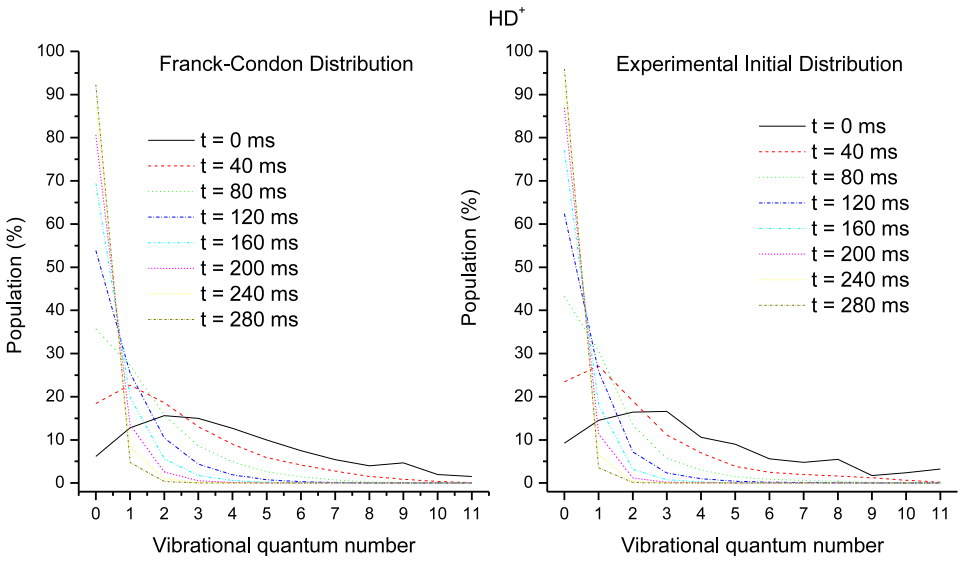

Figure 6.5: Evolution of the vibrational population of an HD^+ ion. The theoretical and experimental initial vibrational population have been taken from [5].

6.5 Virtual Experiments

In order to study the feasibility of the photo-dissociation experiment, 'virtual experiments' were performed. In the simulation, a bunch of HD^+ was created at the center of the trap. For each molecule, the initial position (x,y,z) was assigned randomly between certain limits: $0 < r < r_{max}$; $0 < z < z_{max}$, where $r = \sqrt{x^2 + y^2}$. The energy and the initial angle with respect to the trap axis was also random: $\Delta E = 1\%$; $\Delta\theta = \pm 0.5°$ (these parameters were kept constant in all the different simulations). The bunch was then *shot* by the laser. The laser focus was assigned a cylindrical shape perpendicular to the trap axis. If the molecule was founded inside the focus, it was split into two particles: H and D. To each one, extra energy was assigned, corresponding to their share of the dissociation energy. As they are neutral, they are unaffected by the potentials and will fly straight to the detector. Two different types of experiment were simulated.

In the first virtual experiment, a channel electron multiplier (CEM) was

assumed to be on axis. With this set-up, the only information that is possible to retrieve is the time-of-fight of the neutral particle. This configuration is appropriate if the laser polarization axis is parallel to the trap axis. If that is the case, H and D will produce four different peaks. If we have a diatomic molecule that is dissociating, and we assume that the dissociation energy is transformed integrally into kinetic energy of the atomic components (the atoms dissociated are not in any excited state), we can write:

$$\Delta E = (E_k)_1 + (E_k)_2 = \frac{m_1}{2}v_1^2 + \frac{m_2}{2}v_2^2 \tag{6.5}$$

If we apply momentum conservation in the center of mass frame:

$$\overrightarrow{p_{cm}} = 0 = m_1\overrightarrow{v_1} + m_2\overrightarrow{v_2} \tag{6.6}$$

we arrive at

$$\overrightarrow{v_1} = -\frac{m_2}{m_1}\overrightarrow{v_2} \tag{6.7}$$

By combining 6.7 and 6.5 we obtain:

$$\begin{aligned} |v_1| &= \sqrt{\tfrac{m_2}{m_1}}\sqrt{\tfrac{2\Delta E}{m_1+m_2}} \\ |v_2| &= \sqrt{\tfrac{m_1}{m_2}}\sqrt{\tfrac{2\Delta E}{m_1+m_2}} \end{aligned} \tag{6.8}$$

If the distance from the laser focus to the detector is $D = v_0 t_0$, with $v_0 = \sqrt{2E_0/M}$, where $M = m_1 + m_2$, then we have four different time-of-flights:

$$\begin{aligned} t_1 &= \tfrac{D}{v_0 \pm v_1} \\ t_2 &= \tfrac{D}{v_0 \mp v_2} \end{aligned} \tag{6.9}$$

So with the set of equations above, it is possible to predict the position of the peaks. If $D = 340mm$, $E_0 = 2.0KeV$, $\Delta E = 1.0eV$, the position of the four peaks are: $t(H - forward) = 0.919\mu s$, $t(D - forward) = 0.933\mu s$, $t(D - backward) = 0.963\mu s$ and $t(H - backward) = 0.979\mu s$.

A snapshot of the ions flying is shown in figure 6.6, and the time-of-flight spectrum together with the result of equation 6.9 is plotted in figure 6.7. The

reason for the slight discrepancy between the simulation and the theoretical prediction is due to the randomization of the energy of the molecular beam. Equation 6.9 has proved very useful in estimating at which time we are expecting to have the peaks. In order to be able to resolve the dissociation peaks, a time resolution better than 10ns is needed.

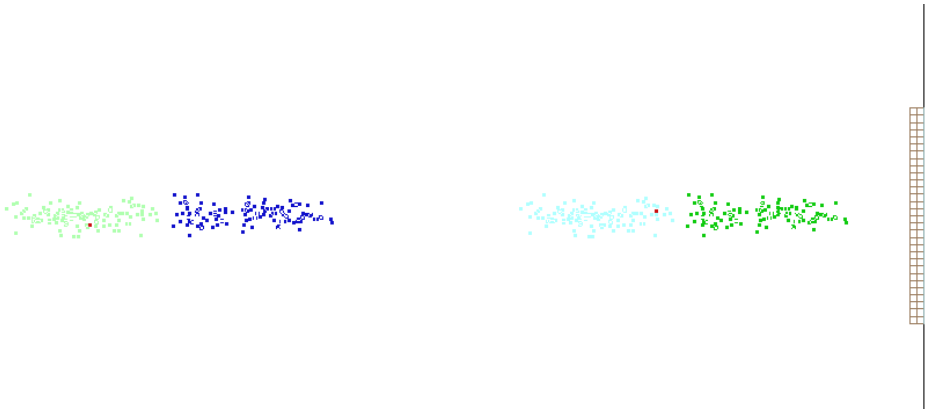

Figure 6.6: Snapshot of a simulation where the laser polarization is parallel to the trap axis.

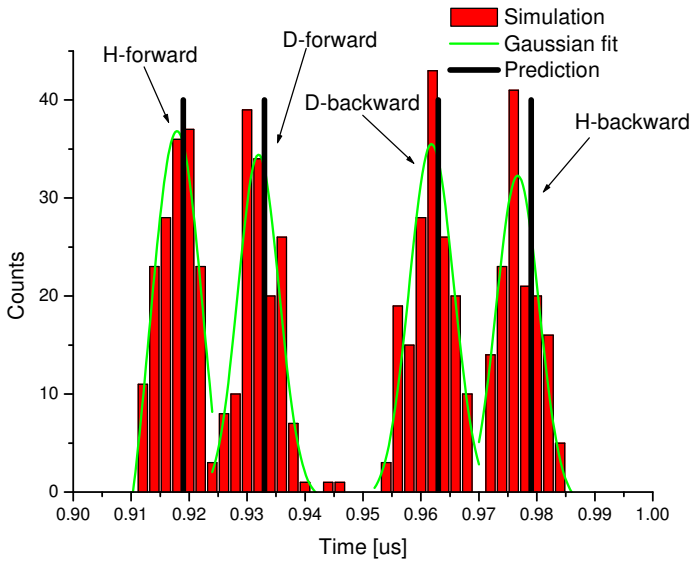

Figure 6.7: Bars: Time of flight spectrum obtained from the simulation; Green curves: Gaussian fit to the TOF spectrum; Black Lines:Positions predicted by equation 6.9.

In a second simulated experiment, the laser polarization was rotated through 90° so it was perpendicular to the trap axis. For this experiment a microchannel plate (MCP) could be used to obtain spatial information. With this configuration we can simulate the behaviour of the molecule assuming that the molecular axis has been aligned by the laser with itself before dissociation. A snapshot of the ions flying can be seen in figure 6.8. The result of the simulation can be plotted in figure 6.9. Figure 6.9a) shows the position of the hits in the MCP, while 6.9b) is the projection of all the counts towards the y axis. In figure 6.9b) the four different peaks are clearly differentiated. We conclude that for a 2KeV HD^+ beam, with a dissociation energy of 1eV, a spatial resolution of 1mm or better is needed.

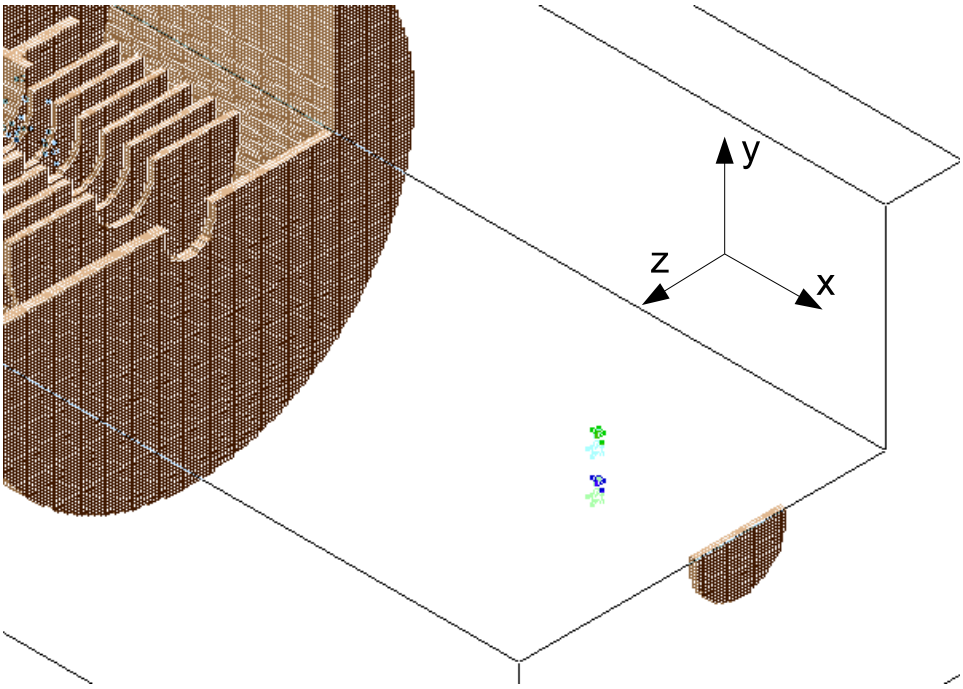

Figure 6.8: Snapshot of a simulation where the laser polarization is perpendicular to the trap axis.

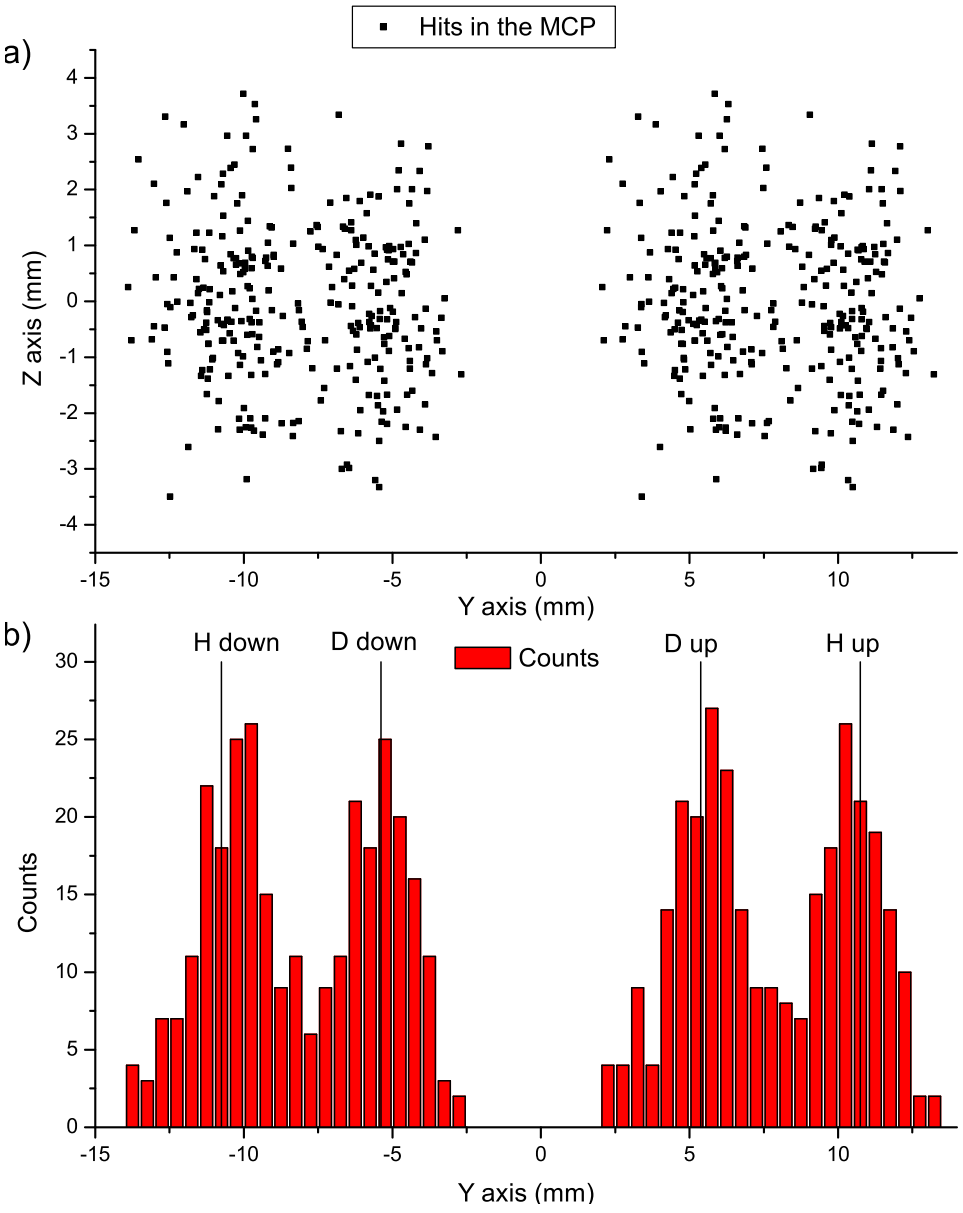

Figure 6.9: Results of the Simion simulation for dissociation when the laser polarization is perpendicular to the trap axis. a)2D signal in a virtual MCP; b)Projection to the y-axis of the data in a).

References

[1] H. B. Pedersen, D. Strasser, O. Heber, M. L. Rappaport, and D. Zajfman, Phys. Rev. A **65**, 042703 (2002)

[2] D. Attiaa, D. Strassera, O. Hebera, M.L. Rappaportc, D. Zajfman, Nuc. Instr. Meth. Phys. Res. A **547**, 279 (2005).

[3] M. Dahan, R. Fishman, O. Heber, N. Altstein, D. Zajfman and W.J. van der Zande, Rev. Sci. Instrum. **69**, 6748 (1998).

[4] Z. Amitay, D. Zajfman, and P. Forck, Phys. Rev. A **50**, 2304 (1994).

[5] Z. Amitay, A. Baer, M. Dahan, J. Levin, Z. Vager, D. Zajfman, L. Knoll, M. Lange, D. Schwalm, R. Wester, A. Wolf, I.F. Schneider and A. Suzor-Weiner, Phys. Rev. A **60**, 3769 (1999).

Chapter 7

QUB LEIBT: Set-up and First Results

In this chapter, we describe the experimental set-up, the acquisition techniques and report the first measurements with the QUB LEIBT .
The technical drawing and a picture of the ion trap can be seen in figure **??**.

7.1 Interaction Chamber

When a mass selected ion beam enters the ion trap beam line, the first thing that the ion beam finds when it arrives at the interaction region is a 4-way cross which holds a set of deflectors plates ($\pm 200V$) and a lens ($\pm 5KV$), see figure 7.2. The voltages are controlled by LabView home-made software. Immediately after, the ion beam arrives at the two 6-way cross chambers that host the ion trap. The two regions are separated by a small hole (8mmØ), which provides differential pumping, see figure 7.2. When the beam enters this region, the first thing it finds is another set of vertical and horizontal deflectors, of small size (14x25mm) which can provide additional control of the injection condition. After that, there is a small aperture of 4mm, which

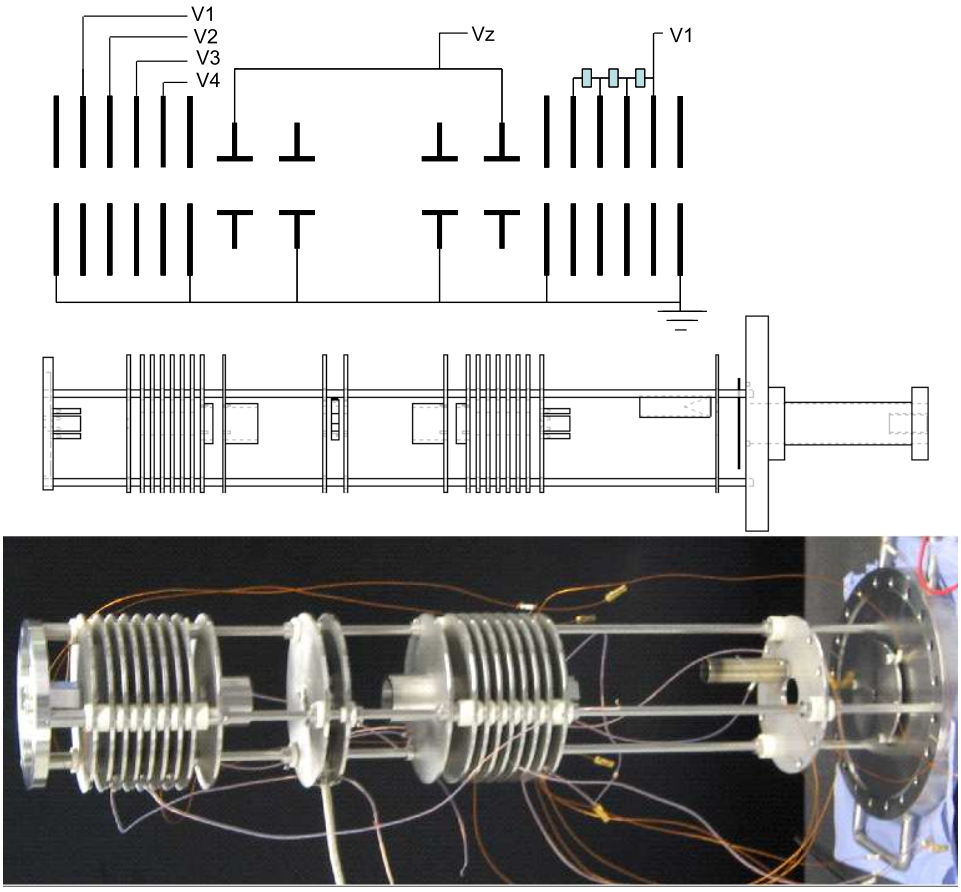

Figure 7.1: Technical drawing of the final design of the QUB LEIBT and the real version of it. It is possible to see the faraday cup and some of the guiding system, as well as the Kapton wire used for the connections.

has a twin found at the exit of the trap. We labelled them as *entrance* and *exit aperture*. Their function is twofold, first they ensure a parallel beam along the trap and second offer us two points where to monitor the ion current. The last aperture plate supports the last set of horizontal and vertical deflectors.

7.1.1 Detectors

The interaction chamber is equipped with three different detectors. The positive/negative ion beam is detected by an off axis Faraday Cup by applying a

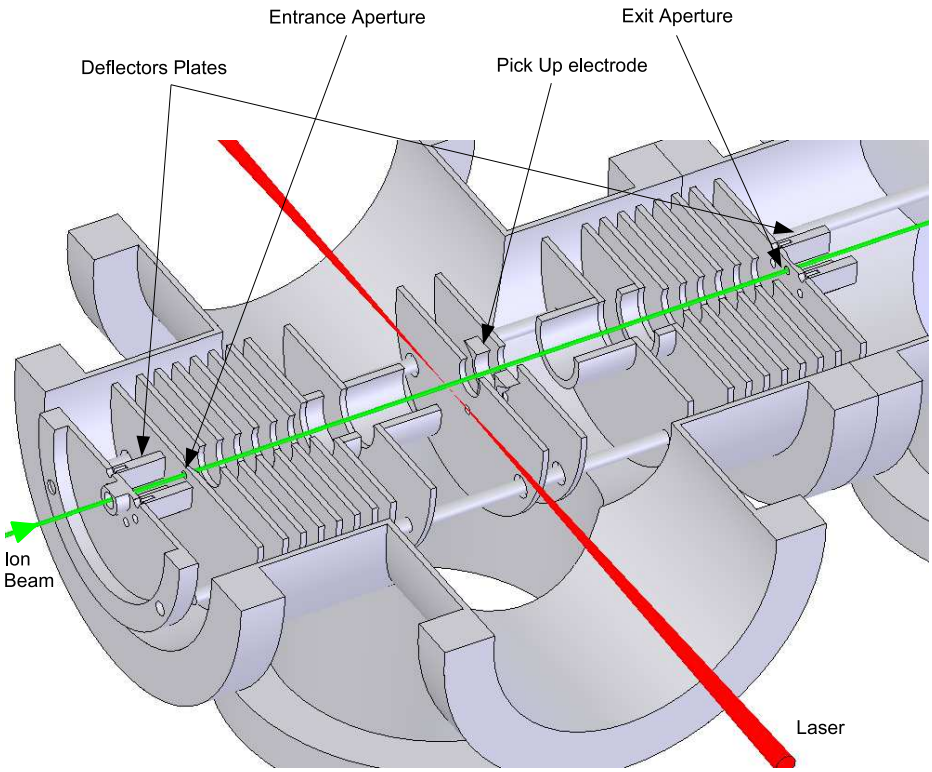

Figure 7.2: Visualization of the ion trap inside the first 6-way chamber. Indications for several elements described in the text.

voltage to the last set of deflectors, figure 7.3. A commercial ceramic channel electron multiplier (CEM) from AmpTek is located on-axis to enable the detection of the neutral particles. To decrease the noise signal, a repeller plate was introduced, see figure 7.3. The third detector is a cylindrical pickup electrode of length 7mm with an inner diameter of 18mm. When charged particles pass through the pickup, an image charge is induced on its surface. This is converted into a voltage by a charge-sensitive amplifier.

7.2 Ion Beam Injection

The ion bunch is obtained by pulsing the voltage on a beam deflector. A TTL signal is inputted to a high voltage switch ($< 100ns$) in a push-pull arrangement (BEHLKE). The TTL pulses that control the switches are generated

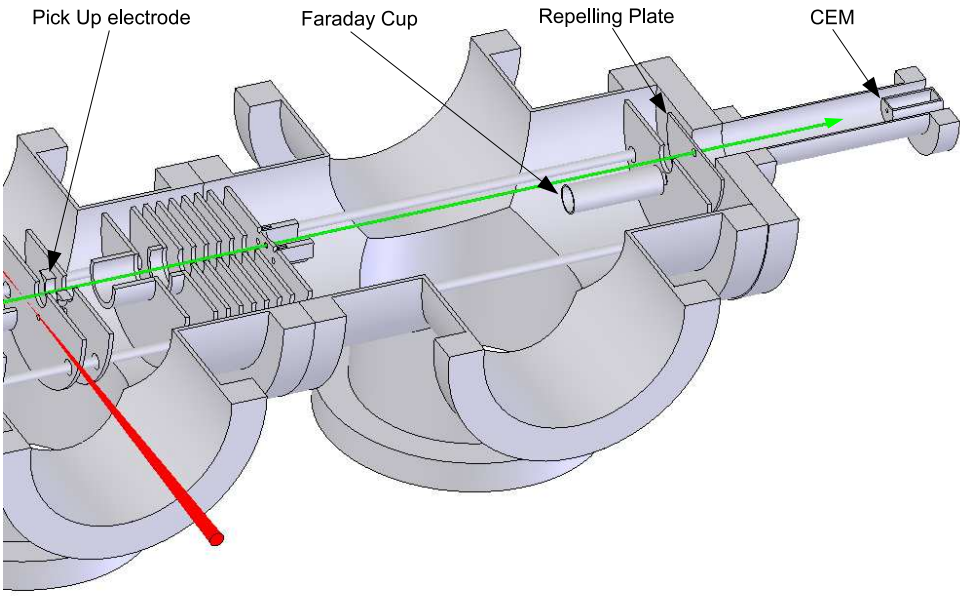

Figure 7.3: Visualization of the second 6-way-cross chamber together with the faraday cup and the CEM.

using a National Instrument counter timer card (PCI-6602), controlled by LabView. The *ion gate*[1] pulsing unit is positioned before the last bending element (magnet or quadrupole), otherwise the neutrals generated before the gate generate a large continuum noise rate on the CEM.

Figure 7.4 is the front panel of the LabView software created for the control of the deflection and injection. In the diagram on figure 7.4, it is possible to see the connections of the different plates of the ion trap. The exit mirrors are all connected through resistors in such a way that $V2 = \frac{3}{4}V1$, $V3 = \frac{2}{4}V1$, $V4 = \frac{1}{4}V1$. The entrance mirror must be independently controlled as a resistive divider will slow down the pulse edge (eg. if plate has $C = 10pF$; $R = 1M\Omega \Rightarrow RC = 10\mu s$). As we only had one pulser, this was used to lower the voltage on V1 only, which was sufficient to allow the ions to enter the trap.

[1]The deflector in charge of the obstruction of the ion beam at an early stage in the beam line will be refered as "the ion gate" or just "the gate"

We found that in order to obtain sufficiently fast rise and fall times ($< 100ns$), it was necessary to use a HV power supply with a current capability of at least 10mA. This was required so that sufficient charge could be driven into the plates in this short time period. The multiple injection sequence

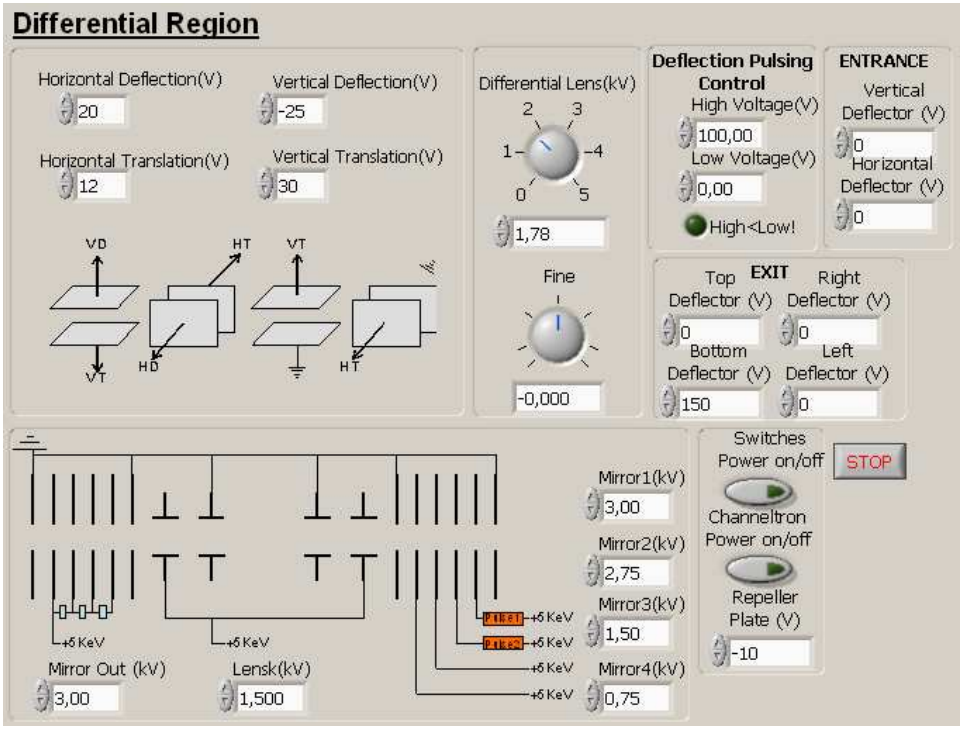

Figure 7.4: Control Panel of the ion beam steering and ion trap voltages. The power for the pulsers and the CEM are also controlled from this panel.

can be seen in the diagram on figure 7.5. Thanks to the 6602NI-PCI card which can produce up to 8 fully configurable pulses with a resolution of 25ns with LabView, it was possible to write a code to produce the desired pulse sequence. One of the card channels was set to generate a pulse train (the trap pulse), while the other channel, corresponding to the gate pulse, was set-up as a *re-triggerable* pulse, which means that every time there is a transition from low to high in the trap channel, the gate pulse is launched, achieving the synchronization of both pulses.

We have four parameters to modify: gate delay, gate width, trap delay and trap width (see figure 7.5). The trap delay corresponds to the time that we allow the ions to be in the trap[2]. The trap width is the time that the voltages in the entrance side of the trap are earthed, so during this time the ions can get in (and out!) of the trap. This parameter must be long enough for the ions to arrive at the trap before restoring the high voltage, but short enough that the ions do not escape from it. The gate width transforms into length from the velocity of the ion beam, giving a measurement of how many ions are you injecting into the ion trap. The gate delay is the dumping time, in the sense that any ion still in the trap escapes while the trap entrance walls are low. This time has to be larger than the period time of the ions in the trap to ensure an empty trap for the next injection.

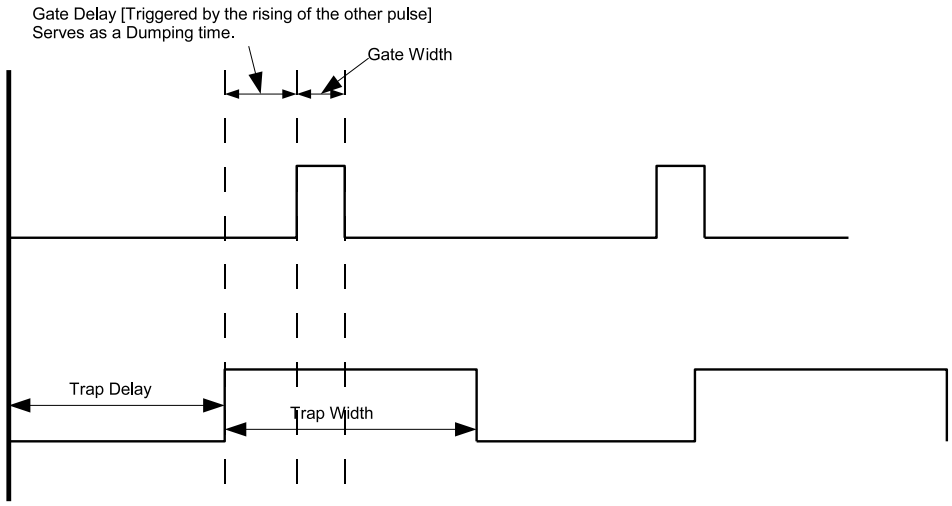

Figure 7.5: Diagram of the pulse sequence used for the injection of the ion beam in the trap.

[2]Except in the first injection when it is just dead time.

7.3 Signal Extraction

The signal acquisition system, at the present, is based on home-made LabView codes. The front panel can be seen in figure 7.6. This code is designed to allow the study of the trapping efficiency and the lifetimes of the ions in the trap. In order to do so, a measurement of how many ions are in the trap as a function of time needs to be done. The loss mechanism that can be monitored is the neutralization through electron capture (positive ion) or detachment (negative ion). In order to detect this neutral, it has to be travelling fast (in the field free region) and in the direction of the CEM.

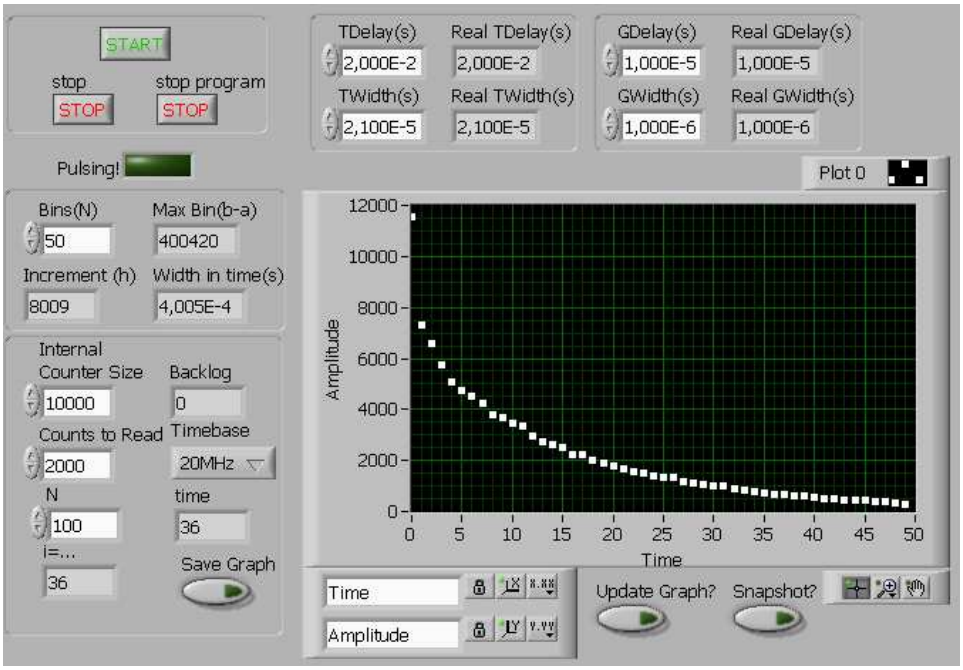

Figure 7.6: Control panel for all the time parameters involve in the injection of the beam the display options (number of bins, Δt), the buffer memory size and how many registers from the buffer are to be read for each internal loop (bigger means a faster graph updated but buffer can then overload).

During an experimental run, the injection of ions is repeated multiple times to obtain good statistics. A program was written which time labelled each event in a buffer which accumulates the counts. The counts are reg-

istered in the buffer as the number of cycles of the internal time-base. A diagram can be seen in figure 7.7, where CEM represents the TTL pulse sent by the detector, *internal time base* is the built-in clock of the acquisition card, which can be set-up to 20MHz or 80MHz, and *buffer* is the actual value that the software receives from the card. When the code reads a change from high to low in the gate pulse for the first time in a experimental run, the code sets the flag *armed counter*, in other words, the acquisition starts.

The information recorded in the counter is actually the time associated with each count. By multiplying it by the time base, the time with respect the *armed counter* point is obtained. By counting how many counts are in a temporal bin, a decay curve is found. The algorithm used to achieve this is as follow

$$Bin(x) = \left|\frac{x - |\frac{x}{N_{max}}|N_{max}}{h}\right| \tag{7.1}$$

where $h = N_{max}/Bins$ and x is the value in the buffer. Example: if the period (in terms of the internal clock) is 20, you have 5 bins and when you read from the buffer you obtain 33, that count has to be placed in bin $= \left|\frac{33-|\frac{33}{20}|20}{20/5}\right| = \left|\frac{33-|1.65|20}{4}\right| = \left|\frac{33-1\times20}{4}\right| = \left|3.25\right| = 3$. So it will add 1 to the number of counts in the third bin. This method is extremely fast, allowing the processing of the data in real time and to keep the amount of memory required for the buffer low.

7.4 Loss Processes

In figure 7.6, we can see an experimental decay curve while the experiment was running. In the numerical simulations performed with SIMION, it was assumed a background free "world", where no neutralization by electron capture or detachment from the residual gas could take place[3]. The self-

[3]The presence of background gas was actually implemented in the code afterwards.

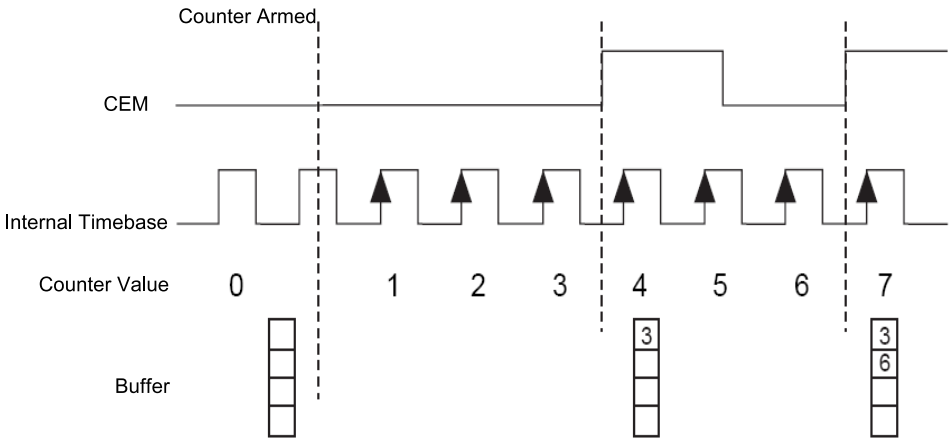

Figure 7.7: Diagram of the acquisition sequence. The *counter armed* line is considered t_0. See text.

interaction of the ions in the bunch was not taken into account either.

The ion-loss processes of an stable ion[4] are due to collisions either with the residual gas or among the ions themselves. For a beam of X^+ ions, the different ion-loss processes can be expressed as:

(a) $X^+ + R^0 \rightarrow X^0 + R^+$

(b) $X^+(p_i) + R^0 \rightarrow X^+(p_f) + R^0$

(c) $X^+(p_i^1) + X^+(p_i^2) \rightarrow X^+(p_f^1) + X^+(p_f^2)$

where (a) represents the neutralization of the trapped ion (X^+) by the residual gas (R); (b) represents ions trapped by a initial stable trajectory defined by p_i, colliding (elastic or inelastically) with the background gas leading to unstable trajectory defined by p_f, and (c) has the same meaning as (b), but this time the scattering occurs with another ion from the bunch itself.

We will assume that further ionization of trapped ions, which also leads to an unstable trajectory, is a negligible phenomena.

[4]The ions lost at the very start, due that they are not in an stable trajectory, are not taken into account.

7.4.0.1 Electron capture

To quantify the description of collisions, Pederson et. al. [1] defined the probability P_i per revolution in the trap that an ion moving on a trajectory i in the phase space undergoes a collision of type j, where j is one of the process described above (j=a,b,c)

$$P_i = 1 - e^{-\lambda_j^i} \tag{7.2}$$

where λ_j^i is the average number of collisions in one revolution for the process j. For the case $j = a, b$, λ_j^i can be written as:

$$\lambda_j^i = n_r \int \sigma_j(v_i) v_i dt \tag{7.3}$$

where n_r is the density of the residual gas, and $\sigma_j(v_i)$ is the crossection of the process j as a function of the ion velocity v_i, and the integral is over one revolution of trajectory i.

For the electron capture case, the cross section can be assumed to be constant over the ranges of ions in the trap [2], allowing us to rewrite equation 7.3 as

$$\lambda_a^i = k \frac{\sigma_a P}{T} \int v_i dt \tag{7.4}$$

where k is a constant $[k = 9.656e18 K/cm^3 Torr]$, P is the residual gas pressure, and T is the temperature. The integral represents just the length of the trajectory, that in a crude approximation could be taken as twice the length of the trap. For the experimental system described in [1], $P \sim 5 \cdot 10^{-10} Torr$, $T \sim 300K$, $\sigma_a \sim 10^{-15} cm^2$, and $\int v_a \, dt \sim 35.5cm$, the value of λ obtained is $\sim 6 \cdot 10^{-7}$. If the corresponding lifetime is given by $\tau = Period/\lambda$, we obtain a lifetime of $\tau_a = 5s$.

7.4.0.2 Ion-neutral scattering

The ion-neutral scattering can be represented by a Fermi-Thomas potential [3], leading to:

$$\frac{d\sigma}{d\Omega} = \frac{\sigma}{\pi} \frac{\theta_{min}^2}{(\theta_{min}^2 + \theta^2)} \tag{7.5}$$

where σ is the total scattering cross section and $\theta_{min} = \hbar/(\mu v a)$ is the minimum angular deflection (for this model to be valid) for a system with reduced mass μ, relative velocity v, and atomic radius a. It can be demonstrated that, within this model, the total scattering cross section is proportional to $1/v^2$[3]. Using equation 7.3, we can write the average number of collision of an ion with the residual gas in one revolution as:

$$\lambda_b^i = k \frac{\sigma_b(v_0) v_0^2 P}{T} \int \frac{dt}{v_i} \tag{7.6}$$

where $\sigma_b(v_0)$ is the scattering cross section at a known velocity v_0 that leads to scattering into angles larger than the acceptance angle. Equation 7.6 is a function of the exact value of Vz and the injection condition through the integral. Again, for the experimental setup of [1]: $\sigma_b(v_0) \sim 10^{-15} cm^2$, $v_0 = 1.4 \cdot 10^7 cm/s$, $P = 5 \cdot^{-10} Torr$, $T = 300K$, and taking the value of the integral[5] as $0.5 \cdot 10^{-12} s^2/cm$, a value of $\lambda_b = 1.6 \cdot 10^{-6}$ is obtained, which corresponds to a lifetime for this process of $\tau_b = 1.8s$

The maximum angular acceptance of the trap plays a key role in this loss mechanism, as a trap with bigger angular acceptance will tolerate bigger scattering angles.

7.4.0.3 Ion-ion scattering

The ion-ion scattering is an important process only in the regions where the ion density is large, i.e. at the turning points, where the ion velocity is small.

[5]The numerical value of $\int \frac{dt}{v_i}$ was calculated using SIMION

For the ion-ion scattering, process c), the average number of collision in one revolution can be expressed as [1]:

$$\lambda_c^i = \int \rho \sigma_c(\triangle v_i) \triangle v_i dt \tag{7.7}$$

where ρ is the density of ions in the beam and $\sigma_c(\triangle v_i)$ is the cross section for scattering of ions with relative velocities $\triangle v_i$. Considering only the turning points, we can rewrite equation 7.7, taking into account that $\sigma_c(\triangle v_i) \propto 1/(\triangle v_i)^2$, as:

$$\lambda_c^i = \rho_{t.p.} \sigma_c(\triangle v_0) \triangle v_0^2 \Big\langle \frac{1}{\triangle v_i} \Big\rangle \tag{7.8}$$

where $\rho_{t.p.}$ is the density in the turning point, that can be estimated using SIMION. An estimate of the average time between ion-ion collisions, for a beam density of $10^6 cm^{-3}$ at the turning point and using equation 7.8, yields a value of $\tau_c = 350ms$, [1].

7.5 Experimental Results

7.5.1 Optimization Techniques.

In order to ensure that the rising of the entrance walls of the trap is done at the right timing, a scan of the values of the "Trap Width" was performed at each energy beam used. In figure 7.8 we can see an example, where the counts registered in the 2^{nd} bin as a function of the Trap Width of a 110nA beam of a 2KeV Ar^+ is plotted. The data was taken over 20 seconds per each data point. 2^{nd} bin means from $t = t_0 + \Delta t$ to $t = t_0 + 2\Delta t$, where t_0 and Δt are (for figure 7.8) $0s$ and $1.003 \cdot 10^{-3} s$ respectively. The trap configuration and timing was: $Vz = 2.4KV$, $TD = 1 \cdot 10^{-2} s$; $GD = 1 \cdot 10^{-5} s$ and $GW = 1 \cdot 10^{-6} s$.

From the figure 7.8, we observe a plateau where the trapping efficiency does not change drastically. If the trap closes too early, the ions will not reach it in time, while if you close the trap too late, they will be reflected and will

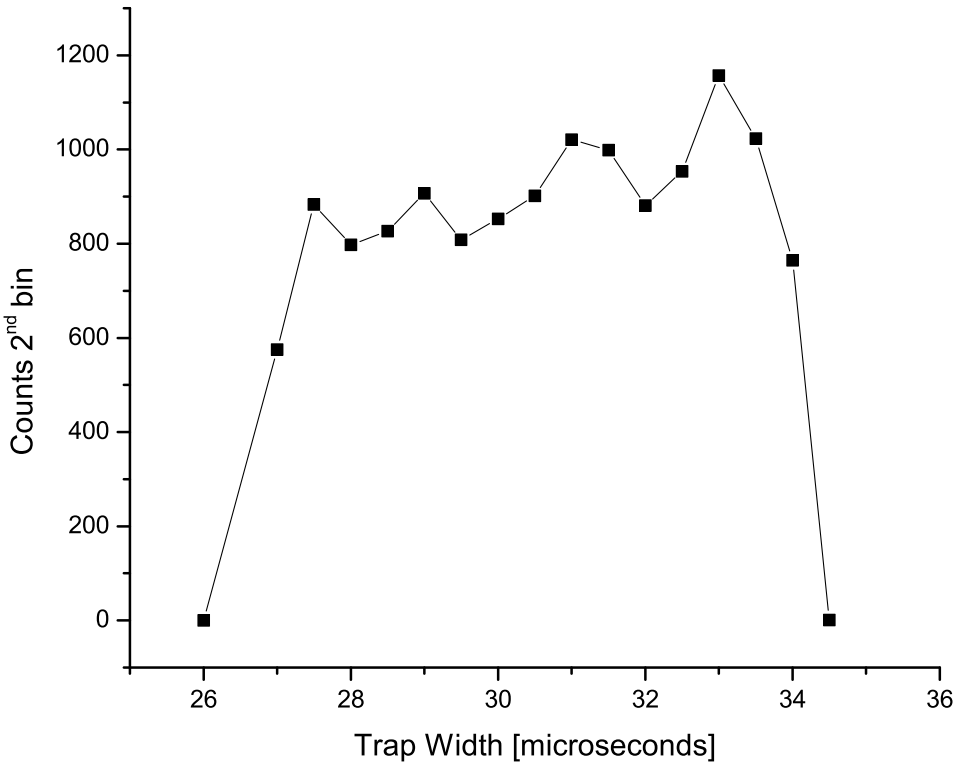

Figure 7.8: Counts registered in the 2^{nd} bin as a function of the Trap Width of a 110nA beam of a 2KeV Ar^{+}.

escape. The time window observed in 7.8 is exactly the period of the ions in the trap ($6.5\mu s$).

It was found that optimal trapping conditions were obtained when the beam transmission to the Faraday cup was maximized with the lens and reflection voltages on as observed in figure 7.9.

7.5.2 Trapping Efficiency Curves.

We need to find out what percentage of the initially injected ions are still in the trap after a certain time. The definition of the trapping efficiency given earlier can be modified so it is more convenient for the data that we obtained from the detector:

$$\epsilon = \frac{N(\Delta t)}{N_0} = \frac{S(\Delta t)}{\alpha N_0 \Delta t} = \frac{\epsilon_r}{\alpha} \tag{7.9}$$

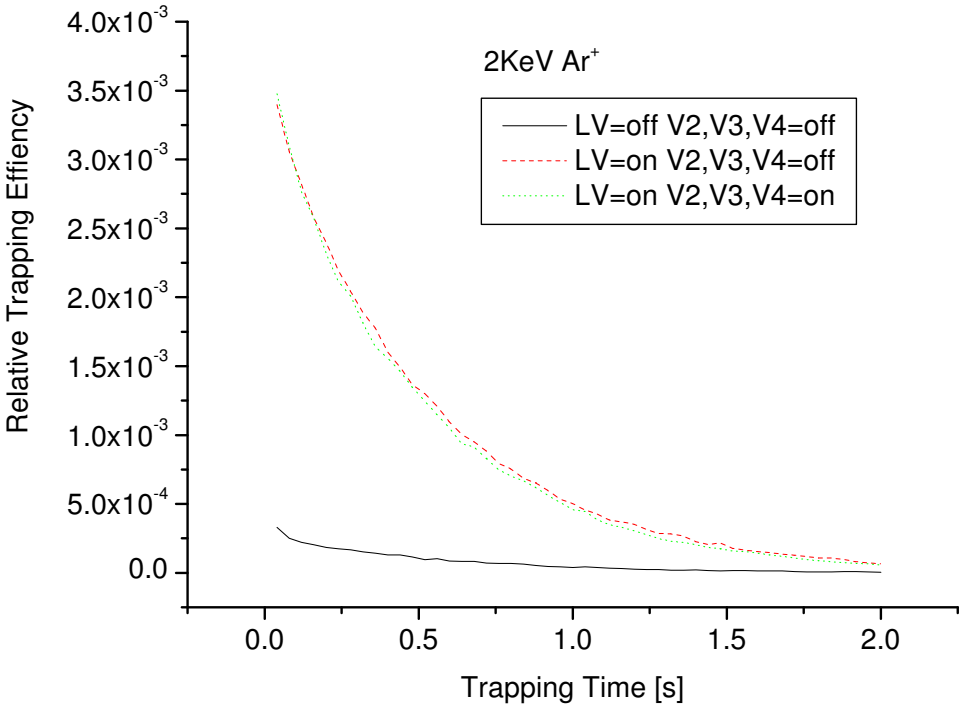

Figure 7.9: Decay curves for when the beam was tuned with: Solid line: LV, V2, V3, V4 off; Long-dashed: LV on, V2, V3, V4 off; Short-dashed: LV, V2, V3, V4 on. [From now on, Lens Voltage=LV, and not Vz as before]

where α is a constant of proportionality (that accounts for the neutralization process, the CEM efficiency and the geometrical acceptance of the detector), N_0 is the initial number of ions, Δt is the interval time at which the signal was measured and $S(\Delta t) = counts(\Delta t)/Injections$. A good estimation of the initial number of ions can be obtained using $N_0 = t_{bunch} I/e$, where t_{bunch} is the time that the Ion Gate is open for and I is the current measured in the faraday cup. All together, it is possible to express the relative trapping efficiency ϵ_r as

$$\epsilon_r = \frac{Counts(\Delta t)\ e}{\Delta t\ Injections\ t_{bunch} I} \tag{7.10}$$

The methodology used to determine the different experimental parameters needed to compute ϵ_r was the following. The value of the 'Lens Voltage' was changed, and using the software described in section 7.3, the value of the

second bin was determined. The curves of ϵ_r as a function of the focal voltage are a representation of the trapping efficiency at relatively *short times*. The trapping efficiency curves obtained are plotted in 7.10, where the species, background gas and value of the 'Mirror Voltage' are specified.

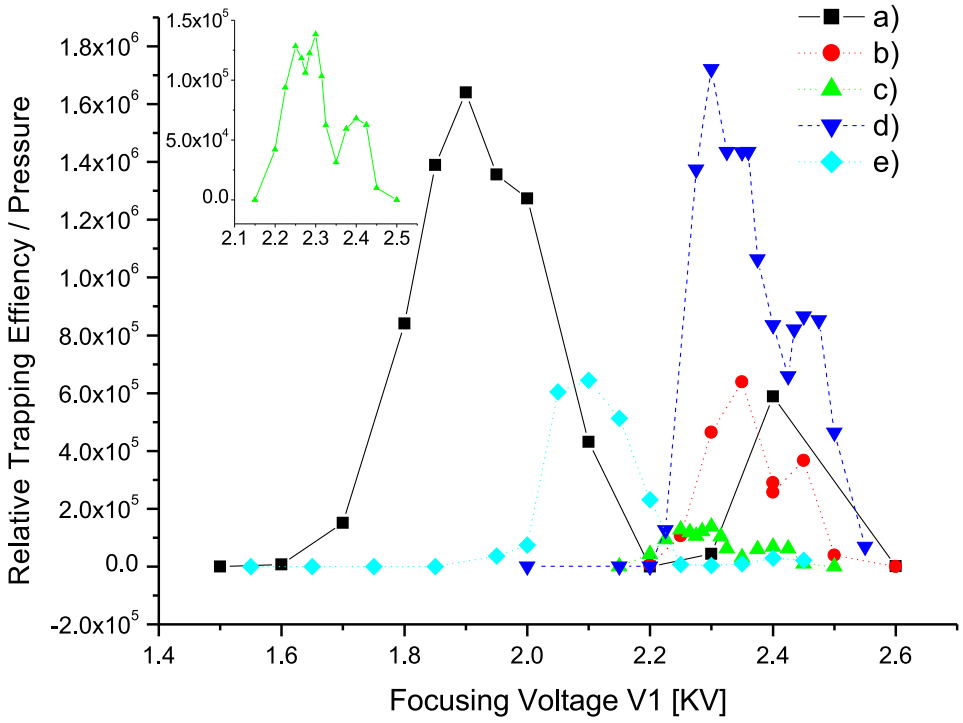

Specie	*Beam Energy*	*Reflector Voltage*	*Background Pressure*	*Graph*
H_2^+	2.0 KeV	3.33 KV	6.59e-9 mbar	a)
H_2^+	2.0 KeV	3.00 KV	5.9e-9 mbar	b)
Ar^+	2.0 KeV	2.90 KV	6.8e-9 mbar	c)
Ar^+	2.0 KeV	3.0 KV	4.02e-9 mbar	d)
He^+	2.0 KeV	3.50 KV	4.02e-9 mbar	e)

Figure 7.10: Relative trapping efficiency for several species and mirroring voltages. The insert is a zoom of the Ar^+ at V1=2.9KV.

The two sets of data taken for a value on V1 of 3.0KV are plotted in figure 7.11 together with the simulation results. We notice that the simulations produce two well differentiated peaks while in the experiment they overlap.

To understand better what *short times* meant earlier, the periods of

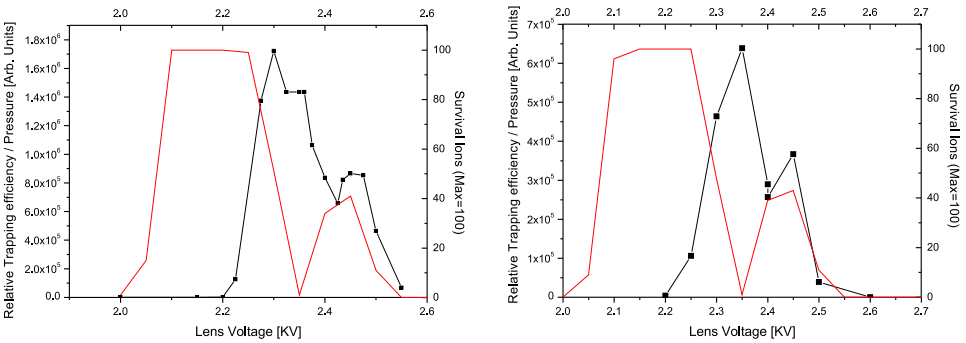

Figure 7.11: Relative trapping efficiency as a function of the lens voltage. Left: 2KeV beam of Ar^+; Right: 2KeV beam of H_2^+. Solid Curve: Simulations; Square-Line: Experimental points.

the different cases have been calculated using Simion3D for an ion exactly at the center of the trap, with $3KV$ on the mirroring plates and $0KV$ on the focusing lens (so this is the minimum period possible for this specific voltage on the mirrors) and for $LV = 2KV$, see table 7.1. The calculation for $LV = 2KV$ shows how much the period changes with the value applied to the lenses voltage. The dependence of the period with the radius is very weak and introduces no significant change with respect to the calculations done at the exact center of the trap. The number of oscillations shown in table 7.1 corresponds to the number of times that the ions would have to fly forward and backward inside the trap before being neutralized and detected as a count in the 'second bin'.

Table 7.1: Periods obtained for different species using SIMION.

Species	Beam Energy	RV	dt	Period (LV=2KV)	Period (LV=0KV)	Oscillations (LV=2KV)
H_2^+	2.0KeV	3.00KV	4e-3s	1.64e-6s	1.51e-6s	2439-4878
H_2^+	2.0KeV	3.33KV	4e-3s	1.56e-6s	1.42e-6s	2564-5128
Ar^+	2.0KeV	2.90KV	3e-3s	7.58e-6s	6.97e-6s	395-791
Ar^+	2.0KeV	3.00KV	2e-2s	7.34e-6s	6.72e-6s	2724-5449
He^+	2.0KeV	3.50KV	0.04s	2.17e-6s	1.98e-6s	18433-36866

7.5.3 Decay Curves

In figure 7.12a), trapping curves at LV corresponding to peaks of figure 7.10 are plotted. Each curve was fitted to a first, second and third order exponential decay, the fit with a parameter R^2 closer to 1 was determined the best fit. A better fit for an n^{th} order decay is usually associated with n mechanisms taking part in the decay. As we know, there are three loss-mechanism in the ion trap: electron capture, ion-neutral scattering and ion-ion scattering, all of them having different timescales. Another factor is the presence of excited states in the ion beam generated by the ion source. Different long-lived electronic or vibrational states would have different electron-crossections, so their decay would be different from one another.

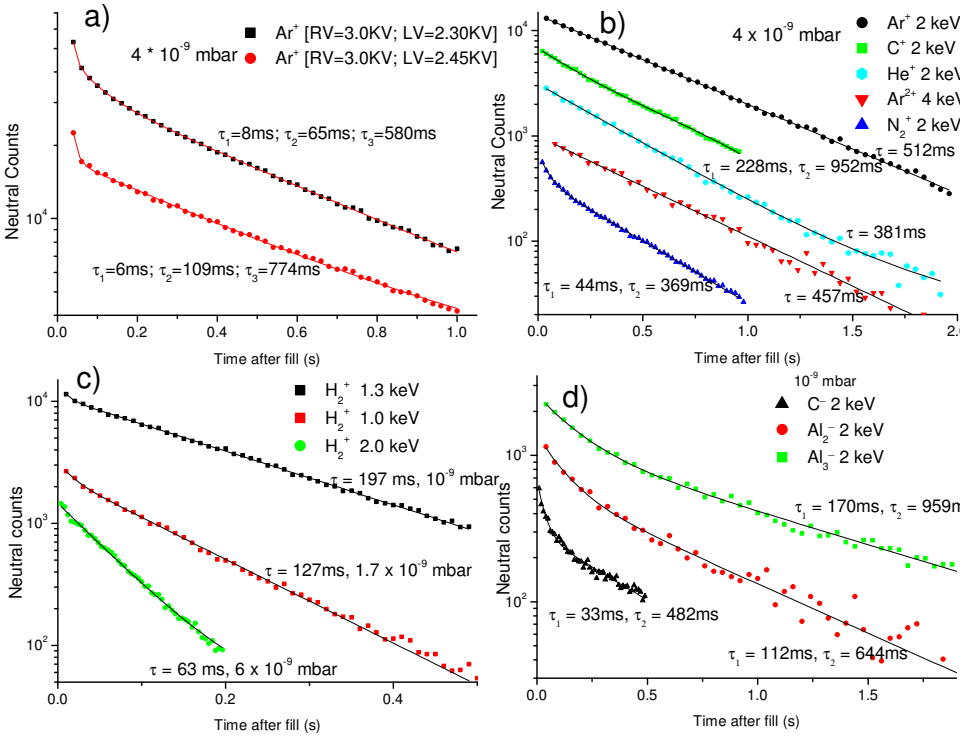

Figure 7.12: Decay Curves. Points: Experimental points; Solid Curve: 1^{st}, 2^{nd}, 3^{rd} exponential fit.

We can compare our lifetimes with these obtained by other groups with

similar devices. Table 7.2 give some of the lifetimes reported[6]. The lifetime normalized to $10^{-10}mbar$ is also given.

Table 7.2: Comparison of lifetimes achieved by several groups. Normalized lifetime at $10^{-10}mbar$.

Specie	Beam Energy	Pressure	Lifetime	Normalized lifetime	Publication
Xe^+	4.2KeV	$3.9 \cdot 10^{-10}mbar$	1.6s	6.4s	[5]
Ar^+	4.2KeV	$3.9 \cdot 10^{-10}mbar$	0.95s	3.8s	[5]
D_2^+	4.2KeV	$3.9 \cdot 10^{-10}mbar$	0.36s	1.44s	[5]
HD^+	4.2KeV	$5.3 \cdot 10^{-10}mbar$	0.27s	1.44s	[5]
N_2^+	4.2KeV	$2.7 \cdot 10^{-10}mbar$	0.98s	2.61s	[5]
Ar^+	4.2KeV	$3.9 \cdot 10^{-10}mbar$	0.164s	0.656s	[6]
Ar^+	2.8KeV	$5.6 \cdot 10^{-10}mbar$	1.7s	9.51s	[4]
Ar^+	2.KeV	$4.0 \cdot 10^{-9}mbar$	0.774s	30.8s	QUB
Ar^{2+}	2.KeV	$4.0 \cdot 10^{-9}mbar$	0.457s	18.3s	QUB
He^+	2.KeV	$4.0 \cdot 10^{-9}mbar$	0.381s	15.3s	QUB
C^+	2.KeV	$4.0 \cdot 10^{-9}mbar$	0.952s	38.1s	QUB
N_2^+	2.KeV	$4.0 \cdot 10^{-9}mbar$	0.369s	14.8s	QUB
H_2^+	2.KeV	$1.0 \cdot 10^{-9}mbar$	0.197s	1.97s	QUB
C^-	2.KeV	$1.0 \cdot 10^{-9}mbar$	0.482s	4.82s	QUB
Al_2^-	2.KeV	$4.0 \cdot 10^{-9}mbar$	0.644s	6.44s	QUB
Al_3^-	2.KeV	$4.0 \cdot 10^{-9}mbar$	0.959s	9.59s	QUB

A direct comparison with previous work is difficult as we have used lower energies and hence the cross section may be different but from the normalized lifetimes it appears that our ion trap has longer lifetimes. We postulate that

[6]In some cases, values of the lifetime for the bunching and for the synchronization regions were available. The longest lifetime is the one given in the table.

this is due to the increased angular acceptance which increases the stable phase space and limits loss of ions due to elastic scattering from background gas and ion-ion collisions.

7.5.4 High Precision Measurements

7.5.4.1 Diffusive region

As has been discussed earlier, in the diffusive mode, the trapped bunch disperses with time and eventually fills the whole length of the trap. If we measure the neutrals produced in the trap as a function of time with a time resolution lower than period of the trap, a burst of neutrals is produced when the bunch is travelling toward the detector. This behaviour should be more accentuated at times close to the injection, when ions are still bunched. High time resolution results obtained in the diffusive regime are shown in figure 7.13.

It is possible to see how the bunch nature of the beam starts to disappear around 1ms.

By performing a Fourier Transform to the data of figure 7.13, figure 7.14 is obtained. Even with the bunching disappearing after just 1ms, it is possible to obtain the oscillating frequency with a series of corresponding higher harmonics. By fitting a gaussian function to the first peak, we obtain an experimental measurement of the frequency of the ions in the trap of $140838 \pm 424\ Hz$ ($\frac{f}{\Delta f} = 167$).

7.5.4.2 Synchronization mode

We have seen that the bunching nature of the injected beam is lost around $1ms$ for the specific case of $RV = 3.33KV$ and $LV = 1.9KV$. In the synchronization mode we expect this non-diffusive time to last longer. Looking back to the trapping efficiency ϵ_r curves, a good bunching behaviour is expected for LV around $2.35 - 2.4KV$. The results for a 2KeV of Ar^+ with

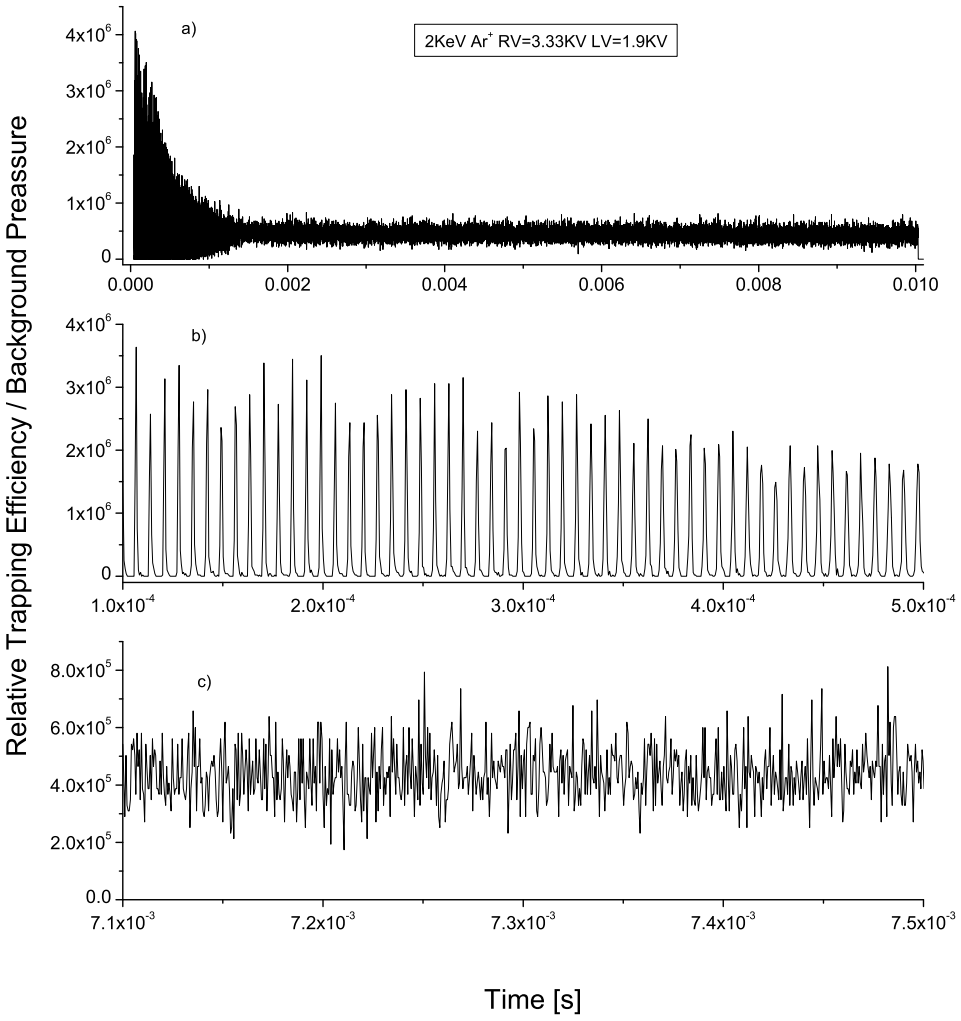

Figure 7.13: High precision decay curve measurement of Ar in the Diffusive region. a)Full time range of the measurement. b)Zoom into the early time, where the ions still form a bunch c)Zoom into the region where the ions fill the trap.

$RV = 3.0KV$ are plotted in figure 7.15, where the study was done for several values of LV. This time, the bunching is observed to survive until $10ms$ for $LV = 2.35KV$, while just until $2ms$ for $LV = 2.45KV$. As can be seen from the four small graphs in figure 7.15 which show the time evolution of the signal, it is not the bunching which disappears but the signal that is statistically too low.

If a FFT is performed on the data of figure 7.15 corresponding to $LV =$

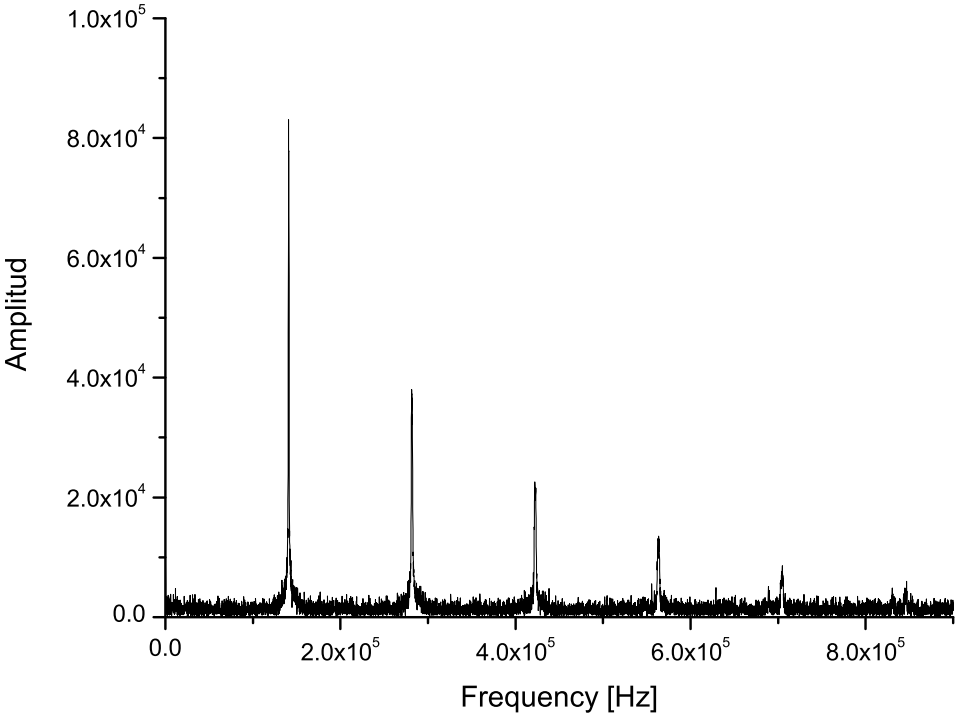

Figure 7.14: FFT of Ar data for dispersive mode.

$2.35KV$ and perform a Lorentzian fit (fits better than a Gaussian in this case) to the first peak, we obtain a frequency of $130282 \pm 80\ Hz$ ($\frac{f}{\Delta f} = 809$). This gives a period of $7.67\mu s$, while with Simion you get $7.57\mu s$. The two things to notice here are the excellent agreement with the simulation result and that the accuracy in the determination of the experimental value has increased substantially with respect to the diffusive mode, even though the statistics in this last measurement were not as good.

The reason behind this discussion of the measurement of frequency is due to the possible use of the ion trap as a mass spectrometer thanks to the fact that $\frac{1}{f} \propto \sqrt{\frac{M}{q}}$. If we assume a period of $5\mu s$, a trapping time of $200ms$, and a length of the trap of $150mm$, the trap acts as a time of flight analyzer of $11.6Km$ long!

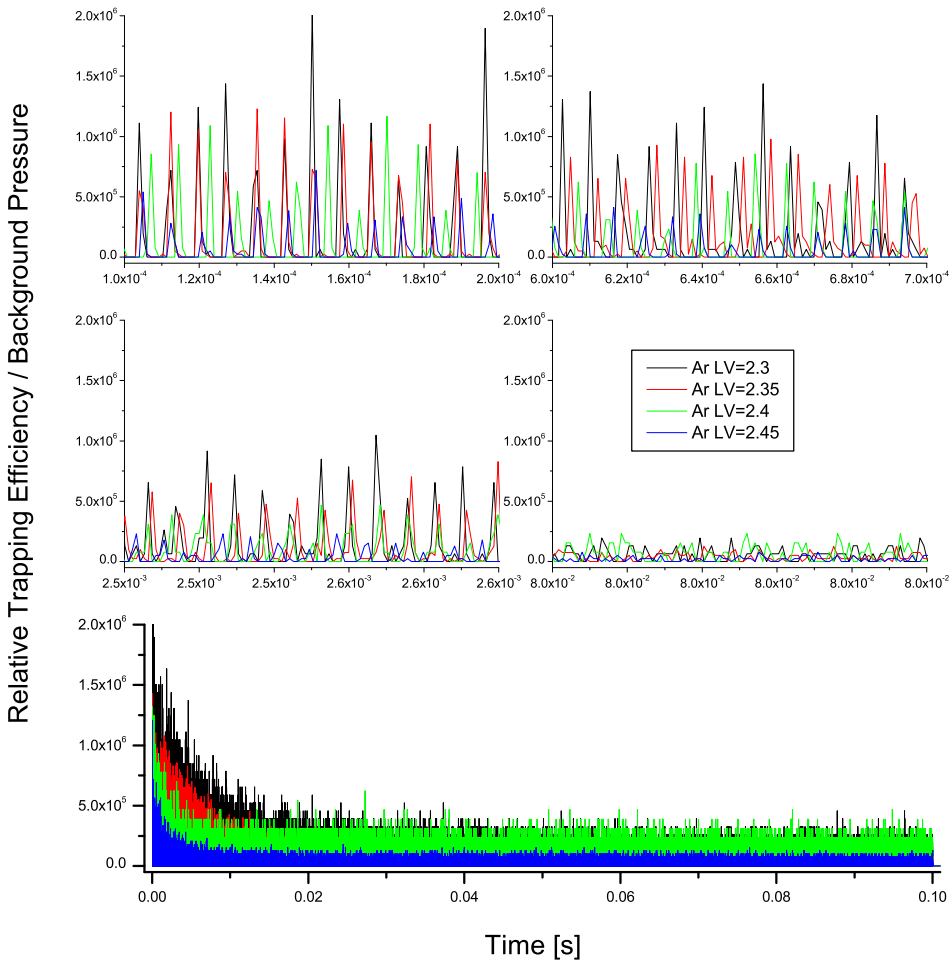

Figure 7.15: High Precision bunching mode for Ar.

To finalize this section, I would like to show the transition from low to high time accuracy. Figure 7.16, shows different measurements for a 2KeV of N_2^+ (RV=3.0KV LV=2.35KV) for different time widths of the bin. We can see that by using equation 7.10, which takes into account the width of the bin, the different curves are approximately coincidental.

The graph for N_2^+ is quite surprising in the sense that even if we should be in the bunching mode, the bunching disappears before 1ms and seems to come back for a short time around 2.5ms. A possible explanation to this behaviour could be the presence of several bunches.

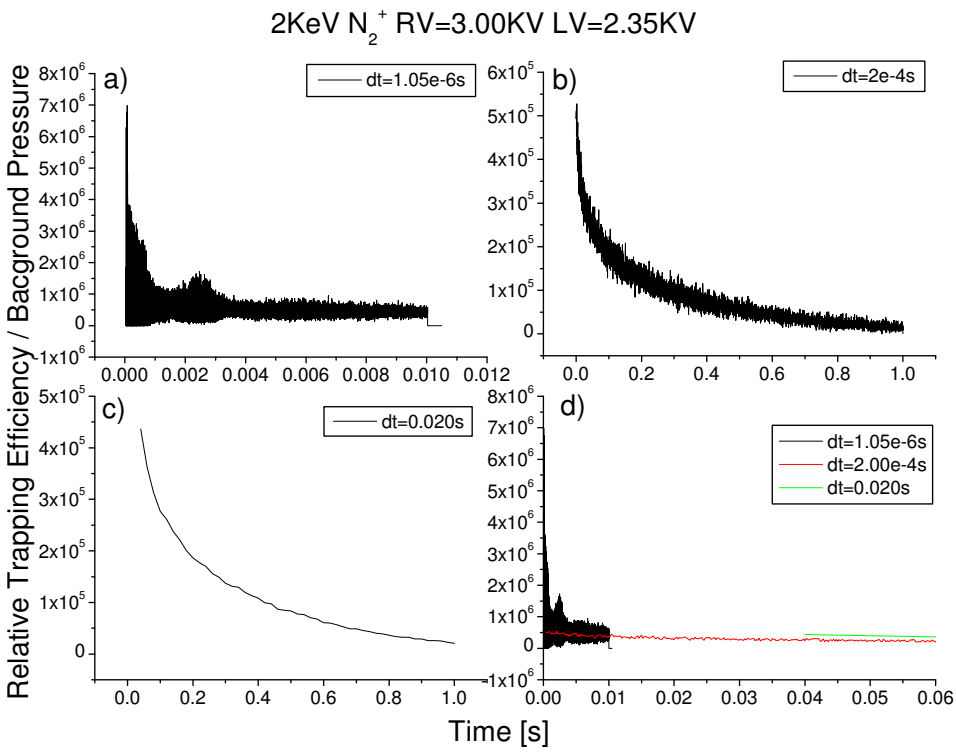

Figure 7.16: Decay curves for a 2KeV N_2^+ beam obtained for several bin sizes. a) $\Delta t = 1.05 \cdot 10^{-6} s$; b) $\Delta t = 2.0 \cdot 10^{-4} s$; c) $\Delta t = 2.0 \cdot 10^{-2} s$; d)Illustrate the normalization procedure used.

7.5.5 A Demonstration of Population Manipulation using Laser Radiation.

Trapped ions could be irradiated using laser pulses of energy $2.5 \mu J$, $300 fs$, $\lambda = 800 nm$ and a repetition rate of 250kHz using the output of a Coherent REGA9100 amplifier. This has been done with aluminium clusters, as shown in figure 7.17.

If the decay curves obtained when the laser is 'off' and when it is 'on', are parallel (in a log scale), it would mean that the decay mechanism in both is the same: neutralization with the background gas. If the curve corresponding to when the laser is 'on' decays faster, it would mean that the laser is contributing to the depletion of the population of trapped ions.

There are clearly two regimes for the case of Al_2^- when the laser is 'on': an initial fast decay (where the rate is initially a factor 5 higher than in the absence of the laser); and a slower second decay at later times. The two second order exponential fits appear to become parallel curves for later times, meaning that there are some states of Al_2^- which are unaffected by the laser. This conclusion must be quantified by the fact that there are poor statistics at the end of the "laser on" curve. But if this conclusion holds true, it will mean that we have removed ions with higher vibrationally excited levels and hence the remaining ion show a lower internal temperature. This methodology can become very useful in situations where the lifetimes are too long for spontaneous decay to the ground state. By using a laser with a photon energy just below that needed to ionize the ground state of the molecule , it should possible to obtain a "cooled" molecular beam, in the sense that the only molecules left would be in the ground state configuration.

For this results, the laser intensity was low enough ($< 10^8 W/cm^2$) for multiphoton processes to be negligible. The vertical electro affinity for the two studied clusters are [7] $EA(Al_2^-) = 1.55eV$ and $EA(Al_3^-) = 1.90eV$. The vertical electron affinity is the difference in the energy between the ground state of the anion and the energy of the neutral cluster having the same geometry as the negative molecule. For Al_2^-, this should support the hypothesis that there is enough energy to ionize excited vibrational levels but not the ground state.

For the case of Al_3^- there is a small, but clear increase in the neutral rate. This can just indicate that a fraction of the initial population of Al_3^- are in excited states with electro affinities lower than the photon energy.

7.6 Conclusion

In this second part of the thesis we have shown how we have developed a linear electrostatic ion beam trap based on the principles of an optical res-

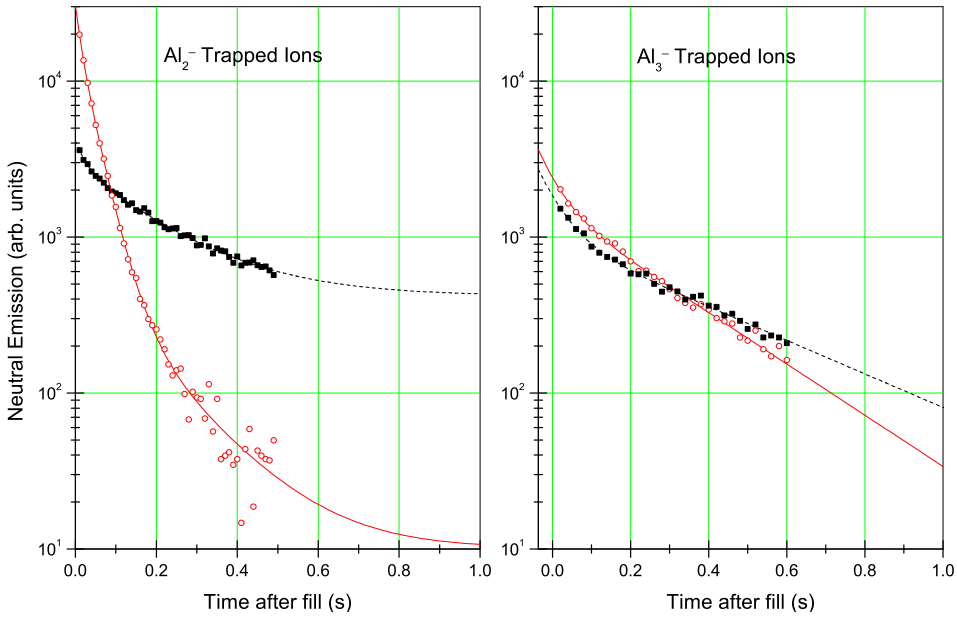

Figure 7.17: Differences between trapped aluminium cluster with and without laser. Full Squares: experimental data when the laser is off; Empty Circles: experimental data when the laser is on; Lines: 2^{nd} order exponential fit.

onator. Simulations were carried out before the actual construction to improve the trapping efficiency with respect to others LEIBTs. This improved design with associated electronic and control software was constructed and tested under ultra-high vacuum condition in our laboratory. These improvements were justified by experimental results which showed a dramatic improvement in trap lifetimes.

Thanks to our high resolution acquisition system, we have been able to see experimental evidence of diffusive and bunching behaviour. By doing a fourier transform of this high resolution data, the capability of the device as a mass spectroscopy has been assessed. Using an in-house 300fs laser system, we have demonstrated the capability of depleting the number of ions in the trap. Using aluminium clusters which are expected to be initially formed in a range of vibrational states, we show that it is possible to deplete higher vibrational levels and influence the vibrational population.

7.7 Future Experiments

The device has the capability of performing a number of unique experiments. The results in this thesis show that HD^+ ions can be trapped for long enough ($t_{trapping} > 300ms$) to allow nearly 100% to decay into their ground vibrational state. This will enable the first experimental studies on the dissociation of the Hydrogen molecular ion in its ground state using an intense fs laser (from the intense ASTRA Laser at RAL).

These type of studies can be extended to a vast diversity of molecular ions, thanks to the availability of ion sources at QUB (a negative sputtering ion source and a penning type source). Due to the fact that the trap is electrostatic (there is no mass limitation) it would allow studies of cooled DNA, proteins and other massive molecules to be performed. The existence of a MALDI source in QUB and the expertise in this area, makes this a highly interesting path to follow.

With the combination of the available ion sources, the new developed linear electrostatic ion beam trap and the strong laser group which is installing a new laser fs system, the group is strongly positioned for the future.

References

[1] H. B. Pedersen *et al.*, Phys. Rev. A **65**, 042704 (2002).

[2] G. J. Lockwood, Phys. Rev. A **2**, 1406 (1970).

[3] J. D. Jackson, in *Classical Electrodynamics*, edited by 2nd ed. (Wiley, New Yorkr, 1975).

[4] H. F. Krause, C. R. Vane, and S. Datz, in *Proc. 16th Int. Conf. On Application of Accelerators in Research and Industry*, edited by ed J L Duggan and I. L. Morgan (AIP Conf. vol 576, New York: AIP, 2001).

[5] M. Dahan *et al.*, Rev. Sci. Instrum. **69**, 6748 (1998).

[6] H. B. Pedersen *et al.*, Phys. Rev. Lett. **87**, 055001 (2001).

[7] B. K. Rao and P. Jena, J. Chem. Phys. **111**, 1890 (1999).

Appendix A

Calculations

A.1 Calculation of the Shift factor

Vector Poynting = Intensity; E=electric field

$$I = \langle S \rangle = \frac{\langle E^2 \rangle}{\mu_0 c}$$
$$E_L = E_0 \cos(\omega t) \rightarrow \langle E^2 \rangle_L = \frac{E_0^2}{2}$$
$$E_C = E_0[\cos(\omega t)\hat{x} + \sin(\omega t)\hat{y}] \rightarrow \langle E^2 \rangle_C = E_0^2$$
$$\Rightarrow I_L = \frac{I_C}{2}$$
$$N_L^{Theory}(I) = N_C^{Theory}(I \cdot 1.31)$$
$$N_L^{Exp}(I_L) = N_C^{Exp}(I_L \cdot 1.31) = N_C^{Exp}(\frac{I_C}{2} \cdot 1.31)$$

A.2 Bending Magnet

Axial field of a Helmholtz Coil carrying a current I (From "Foundations of electromagnetic theory", Reitz)

$$B_z(z) = \frac{N\mu_0 I a^2}{2}\Big\{\frac{1}{(z^2+a^2)^{3/2}} + \frac{1}{[(2b-z)^2+a^2]^{3/2}}\Big\} \qquad \text{(A.1)}$$

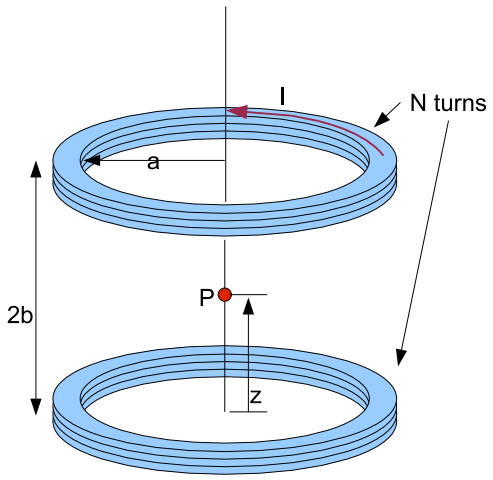

Figure A.1: Hello

At $z = b$ the first derivative vanishes: $\frac{dB_z}{dz}\big|_{z=b} = 0$. If $z = b$ and $2b = a$, then $\frac{d^2B_z}{dz^2}\big|_{z=b} = 0$, leaving:

$$B_z(z) = \frac{\mu_0 NI}{a}\frac{8}{5^{3/2}} \tag{A.2}$$

The field $B_z(z)$ can be develooped in a Taylor's seris about the point $z = \frac{1}{2}a$. Thanks that the first three derivatives vanish, and evaluating the fourth explicitly, $B_z(Z)$ can be written as:

$$B_z(z) = B_z(a/2)\Big\{1 - \frac{144}{125}\Big(\frac{z - a/2}{a}\Big)^4\Big\} \tag{A.3}$$

(B is in Tesla)

Lorentz Force for $\overrightarrow{E} = 0$:

$$\overrightarrow{F} = q\overrightarrow{v} \times \overrightarrow{B} \tag{A.4}$$

Like $\overrightarrow{v} = (v, 0, 0)$ and $\overrightarrow{B} = (0, 0, B)$,we can write $F = qvB$. Together with $F = ma = m\frac{v^2}{r}$ we obtain $v = qBr/m$. If the beam is accelerated by a differential potential V, then it will have a kinetic energy $E_k = qV = \frac{1}{2}mv^2$ so we can write:

$$B = \frac{\sqrt{2V}}{r}\sqrt{\frac{m}{q}} \tag{A.5}$$

A.3 "Voltage labelling technique"

Consider the following reaction of a cluster anion caused by the laser field:

$$X_n^- + \hbar w \rightarrow X_i^{q+} + (q+1)(e^-) \tag{A.6}$$

As the beamline is at grounded, the kinetic energy of the negative ion beam is $-S$, where S is the potential applied to the cathode, so $E_b = -S$. If the interaction region has a negative bias (blue coded in figure A.2), then the beam is slow down and the beam energy becomes $E_{PI} = -S + I$. After the interaction with the laser pulse, we have a product with a positive charge $+q$, and if the incident negative ion was a cluster of n atoms, dissociation may have occurred to leave the positive ion made of i atoms. Like the velocity does not change with the laser interaction, the kinetic energy of the product is now $E_1^{'} = \frac{i}{n}(I - S)$. The time spend travelling in the region 1 can be expressed as $t_1 = d_1\sqrt{\frac{m_1}{2(I-S)}}$, where m_1 is the mass of the original cluster anion and d_1 is the length of region 1.

In region 2, the positive ions are decelerated further while undisturbed negative ions are re-accelerated to their original beamline voltage. In this region, positive ions generated by background gas collisions before the biased interaction region are decelerated to their original energy (E_b). Therefore positivi ions generated inside the interaction region require a different deflection voltage than those produced outside the interaction region. This allows us to reduce the background noise considerably as the path length from the magnet to the interaction region (about a 1m) is much larger than the length of the interaction region. In order to calculate the time of flight in this section, we have to take into account that the field is changing linearly with the distance x. If we express the beam energy in function of the distance travelled x as $E_2(x) = E_1^{'} + qI\frac{x}{d_2}$ we can calculate the corresponding

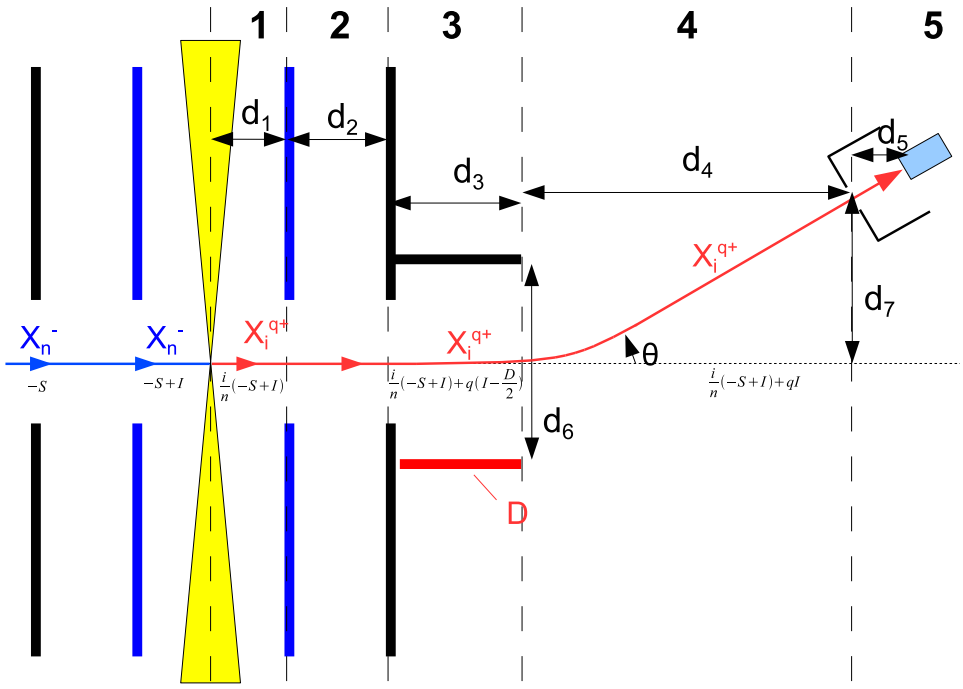

Note: the thickness of all the plates is 4mm. Measurements are made to and from the centre of these plates.

d_1 = 12mm, d_2 = 10mm, d_3 = 24mm, $d_4 \approx$ 43mm, $d_5 \approx$ 8mm, d_6 = 16mm, $d_7 \approx$ 17mm, $\theta \approx \tan(d_7/d_4) = 21.5°$

Figure A.2: Diagram of the 4-Way Slit used to position the laser and ion beam.

t_2

$$\begin{aligned} v(x) = dx/dt \Rightarrow dt = dx/v(x) \\ t_2 = \int_0^{d_2} [\tfrac{2}{m_2}(E_1' + qI\tfrac{x}{d_2})]^{-1/2} \\ t_2 = \tfrac{d_2}{qI}\sqrt{\tfrac{2}{m_2}}[\sqrt{qI + E_1'} - \sqrt{E_1'}] \end{aligned} \tag{A.7}$$

where d_2 is the length of region 2 and m_2 is the mass of X_i^{q+}.

On entering the deflection plates, region 3, one plate is grounded and the other is biased positively (D) to push positive ions into the detector. This means that if the ions pass close to the center of the plate, they will experience a retardation as well as a deflection due as to the potential applied of about D/2, so the velocity of the incoming particle would be $v_x = \sqrt{\frac{2}{m_2}[E_1' + q(I + \frac{D}{2})]}$, so the time it would take the particle to cross

the region 3, is $t_3 = d_3/\sqrt{\frac{2}{m_2}[E_1' + q(I - \frac{Dy}{d_6})]}$.

The angle which the ion is deflected through is given approximately by

$$\tan\theta = \frac{v_y}{v_x} = \frac{qDd_3}{2E_3d_6} \tag{A.8}$$

Region four has a ground potential and this field free region makes up the largest part of the flight time. The energy of the ions and thus their TOF is dependent on the charge state and the fragment mass. Therefore by voltage labelling the interaction region I, the different products can be separated in time as well as by deflection. Here the energy and TOF are given by

$$\begin{aligned} E_4 &= \tfrac{i}{n}(-S + I) + qI \\ t_4 &= d_4/\sqrt{\tfrac{2}{m_2}[E_1' + qI]} \end{aligned} \tag{A.9}$$

Finally, using a similar analysis in region 5 as we did for region 2, we obtain

$$\begin{aligned} E_5 &= \tfrac{i}{n}(-S + I) + qI - \tfrac{qVx}{d_5} \\ t_5 &= \tfrac{2d_5}{qV}\sqrt{\tfrac{2}{m_2}}[\sqrt{qI + E_1'} - \sqrt{q(I - V) + E_1'}] \end{aligned}$$

Appendix B

Fortran Code

B.1 Calculation of the Ion Yield using ADK theory.

```
************************************************************************
C
C NAME: F_Adk_CircVsLinear.f
C AUTHOR: Jofre Pedregosa Gutierrez
C
C DESCRIPTION: Calculation of X --> X+ using tunneling theory (ADK)
C  ussing an expression for an arbitray orbital quantum number l.
C
C
C         Linear and circular polarize light is calculated
C
C this program is write for a l=1 shell!!! The population of m=0 and m=1
C are computed separately and added at the end:
C              X+ = (1/3)X+(m=0) + (2/3)X+(m=1)
C
C Here i use the relation => P(F+)=1-P(F)
C
```

```
CDATE: started:C 30/04/04
C
*************************************************************************
      program F_Adk_CircVsLinear
      implicit none
      doubleprecision ans,aux,aux0,aux1,aux2,d,E0,epsi,f,h,h1,ia,ib
     +,intensity,Ip,lambda,phi,pi,tau,v0,w,w0,x1
      doubleprecision b0(0:1),b1(0:1),b2(0:1),ionaux(0:1),ionyield(0:1)
      integer flag,i,i1,in,m,ni,nmax,zq
      doubleprecision y1(0:1025)
      common /ni/ni,/nmax/nmax,/tau/tau,/linear/b0,b1,b2,/E0/E0
      parameter(pi=3.141592654d0)

***********************************************
      ! Parameters of the final graph
***********************************************

      parameter(
!First intensity point of the graph
!Lasr intensity point of the graph
     +Ia=1.d15, ![W/cm2]
     +Ib=1.d16, ![W/cm2]
     +In=5) !number of points of the graph
!-----------------------------------------------
      !ni number of points for the numerical integrations.
      ni=128
      nmax=int(log(real(ni))/log(2.))
!-----------------------------------------------

*************************
      ! Ion parameters
*************************
```

```
!Ionization Potential.
      Ip=17.42d0          ![eV]
     +   /27.2113961d0      !Conversion to atomic units.

!is the charge state where is left the ion in the X—>X+ for the ADK.
      zq=1

****************************
      !Laser Parameters
****************************

!Full width half maximum for the temporal profile [seconds].
!(Pulse of the laser)
      tau=30.0d-15 ![seconds]
     + / 2.4189d-17 !conversion to atomic units

!Wavelength of the laser [cm]
      lambda=800d-7  ![cm]

!w is the energy of 1 photon in eV
! w=h[eV*s]*c[m/s]/Lambda[m]
      !becouse lambda is in cm, i need to change to m
      w=(4.1357d-15*2.9979d8/(lambda*1.d-2)) ![eV]
     + /27.2113961d0                    !conversion to atomic units

************************************
      ! Laser Beam Line Paramters
************************************
!Focal of the lens used to collimate the laser [cm]
      f=10d0   ![cm]

!Diameter of the laser before being collimated [cm]
      d=1.5d0  ![cm]
```

```
!w0 is the minimum waist radius at 1/e2 [cm]
      w0=4*f*lambda/d   ![cm]

      v0=( (pi**2) * (w0**4) )/lambda ![cm^3]

***********************************************
      ! Parameters for the ADK rate formula:
***********************************************

!Explained in the subroutine adkprefactors

! eq.(2) from ADK paper.
      E0=(2*Ip)**1.5d0
! Calculate the factors on the expression of the rate:
! rate(E)=b0*(E^(-b1))*exp(-b2/E)
! that way, I don't need calculate them each time as them remain
!constant during all the calculation.
!I store the prefactors for the case l=1,m=0, and l=1,abs(m)=1.
      do m=0,1
        call adkprefactors(zq,ip,m,aux0,aux1,aux2)
        b0(m)=aux0
        b1(m)=aux1
        b2(m)=aux2
      enddo
!-----------------------------------------------------
! Calculate the step size in such a way that is equally spaced once is
! plotted in a log-log scale.
      h=dlog10(Ib/Ia)/In
!I open the file where the data is going to be stored.
      open(unit=1,file="F_Adk_CircVsLinear.dat")
      print*, 'The calcuation has started, please wait...'
!I start with the loop that will do the calculation for each intensity:
```

```
!               IonYield(I0)
      do i=0,In
! In theory, the lower limit for the intensity integral should be zero
! but i take 1d10 as a lower limit, assuming that all the way until
! that is zero.
        print*, 'Calculating the point number',i,' of',In
        intensity=10**(dlog10(Ia) + (h*i))
        h1=(intensity-1.d10)/ni
! I calculate the ionyield for the case of circular polarize light and
! linear polarize light: flag=0 => Linear; flag=1 => Circular
        do flag=0,1
! I use a loop to calcuate the different m contributions. The ionyield
! for m=0 and the case m=1 are calculate indepently, and pondered once
! i have the respective ionyields.
          do m=0,1
! Here I calculate the function to integrate in all the points where it
! will be needed.
            do i1=0,ni
!x1 here is the integral over the intensity.
              x1=1.d10 + h1*i1
!x1 is in SI units, but is change inside phi program
!epsi is just a variable that help to write easily.
              epsi=dsqrt( (intensity/x1) - 1.d0)
!aux is the rate integrated over time.
              aux=phi(flag,m,x1)
              y1(i1)=(1.d0-dexp(-aux))
     +         *(epsi/x1) * (5.d0 + epsi**2)
            enddo
! romfxi is the subroutine that calculate the integral.
            call romfxi(y1,h1,ans)
            ionaux(m)=ans
          enddo
        IonYield(flag)= ( V0/6.d0 ) *
```

```
     +    ( (1.d0/3.d0)*ionaux(0) + (2.d0/3.d0)*ionaux(1) )
          enddo
          write(1,*) intensity,IonYield(0),IonYield(1)
        enddo

        close(1)
        print*,'The calculation has finished.'
        print*, 'Data saved in "F_Adk_CircVsLinear.dat".'
        end program F_Adk_CircVsLinear
*************************************************************************
        function  phi(flag,m,x)
        implicit none
        doubleprecision h2,t,ta,tb,adklinear,tau,phi,x,w,adkcirc
        integer i2,ni,flag,m
        double precision rate(0:ni)
        external adklinear,adkcirc
        common/tau/tau,/ni/ni
! I consider infinit as t=2*tau
        tb=2*tau !tau is already in a.u.
        ta=-tb
        h2=(tb-ta)/ni
!-------------------------------------------------------------------------
        do i2=0,ni
          t=ta+h2*i2
          if(flag.eq.0) rate(i2)=adklinear(m,t,x)
          if(flag.eq.1) rate(i2)=adkcirc(m,t,x)
        enddo
        call romfxi(rate,h2,phi)
        return
        end function phi
*************************************************************************
        ! ADK ( Tunneling )
! Reference: M.v.Ammosov, N.B. Delone, and V.P. Krainov, Sov.Phys.Jetp
```

```
! 64(6) December 1986
! Correction in:F.A Ilkov, J.E. Decker and S.L. Chin; J.Phys. B:At. Mol.
! Opt. Phys. 25 (1992)4005-4020
*****************************************************************
      function adklinear(m,t,I0)
      implicit none
      double precision adklinear,b0(0:1),b1(0:1),b2(0:1),e,i0,it,tau,t
      integer m
      common /linear/b0,b1,b2,/tau/tau

!I(t)=I0*(sech(a*t)^2); a= arccosh(sqrt(2))/ ( Tau/2); a=1.76274717/tau
      It=I0/((dcosh(1.76274717d0*t/tau))**2)
!       It=I0/((dcosh(2.63391579d0*t/tau))**2)
!       It=I0*dexp( -8 * (t/tau)**2 )

! in atomic units I=E^2
      ! E[au]=5.33801176d-9*dsqrt( I[w/cm2])
      E=5.33801176d-9*dsqrt(it)
              ! eq 13a of Reference
        adklinear=b0(m)*( E**(-b1(m)) )*dexp(-b2(m)/E)
      return
      end function adklinear
! *****************************************************************
      subroutine adkprefactors(zq,ip,m,b0,b1,b2)
      implicit none
      double precision b0,b1,b2,ip,no,pi,e,lo
      integer zq,m
      parameter(pi=3.1415926d0,e=2.718281828d0)

!Correction in:F.A Ilkov, J.E. Decker and S.L. Chin; J.Phys. B:At. Mol.
! Opt. Phys. 25 (1992)4005-4020
! rate(F)=b0*(F**(-b1))*exp(-b2/F), where F is the amplitude of the
! external field
```

```
! no = effective principal quantum number
      no=zq * (2.d0*Ip)**(-0.5d0)
! lo = effective orbital quantum number
      lo=no-1

!Prefactors:
      b1=2.d0*no -m -1.5d0

      b0=( (3/(2*pi))**1.5d0 )
     +  *( (zq**2) /(3* no**3)  )
     +  * 3 !f(l,m) => f(1,0)=f(1,1)=3
     +  *( ((4* e**2) / (no**2 - lo**2) )**no )
     +  *( ((no-lo)/(no+lo))**(lo+0.5d0) )
     +  *( ((2* Zq**3)/(no**3))**b1 )

      b2=(2* zq**3)/(3* no**3)

      return
      end subroutine adkprefactors
*****************************************************************
      function adkcirc(m,t,I0)
      implicit none
      double precision adkcirc,b0(0:1),b1(0:1),b2(0:1),e,i0,it,t,tau,E0
      integer m
      common /linear/b0,b1,b2,/tau/tau,/E0/E0
      ! 1w/cm2=1.55367965d-16 atomic units of intensity
      It=I0/((dcosh(1.76274717d0*t/tau))**2)
!       It=I0/((dcosh(2.63391579d0*t/tau))**2)
      E=5.33801176d-9*dsqrt(it)
        !eq 25 of reference
!(pi*E0/3E) is the factor to change to circular.
        adkcirc=dsqrt(1.047197551d0*(E0/E))
```

```
     +    *b0(m)*( E**(-b1(m)) )*(dexp(-b2(m)/E))
      return
      end function adkcirc
*****************************************************************
! romfxi is a very fast routine I have wrote myself. I didn't find
! anything(or I did not look enough maybe?) fast enough. So I decided
! to work on my own algorithm and after some weeks, here is my baby...

      subroutine romfxi(y,h,ans)
! x(0:n) contain, where x(0)=a(lower limit of the integral)
! and x(n)=b(upper limit of the integral
      implicit none
      double precision ans,h,sum
      integer i,j,k,n,nmax,st
      common/ni/n,/nmax/nmax
!       nmax=int(log(real(n))/log(2.))
      double precision t(0:nmax,nmax),y(0:n)
      do i=1,nmax
       st=n/(2**i)
       sum=0
       do j=st,(n-1),st
        sum=y(j)+sum
       end do
       t(0,i)=((h*st)/2.d0)*(y(0)+y(n)+2*sum)
      enddo

      do i=2,nmax
       do k=1,i-1
        t(k,i)=((4**k)*t(k-1,i)-t(k-1,i-1))/((4**k)-1)
       end do
      end do
      ans=t(nmax-1,nmax)
      return
```

```
      end subroutine romfxi
```

B.2 Calculation of the time evolution of the vibrational population

```
C
C NAME:
C AUTHOR: Jofre Pedregosa Gutierrez
C DESCRIPTION: Calculate the population of vibrational states as a
C function of time.
C DATE: start: 09/06/04
C
      program main
      implicit none
      double precision a(0:11,0:11),p,pt0(0:11),t,tau(0:11),sum
     +,store(0:11,0:11)
      integer i,j,k,v,vmax
      common /vmax/vmax
      print*, 'Calculation started, please wait...'
      vmax=11
! Initial populations(in %) and radiative lifetimes(in miliseconds):
! Source: Z.Amitay et. al. Phys. Rev. A; 60, 3769 (1999)
      Pt0(11)=3.25d0 ; tau(11)=14.d0
      Pt0(10)=2.40d0 ; tau(10)=13.80d0
      Pt0(9)=1.75d0 ; tau(9)=13.70d0
      Pt0(8)=5.50d0 ; tau(8)=12.30d0
      Pt0(7)=4.80d0 ; tau(7)=11.00d0
      Pt0(6)=5.60d0 ; tau(6)=10.50d0
      Pt0(5)=9.00d0 ; tau(5)=12.00d0
      Pt0(4)=10.60d0 ; tau(4)=15.50d0
      Pt0(3)=16.60d0 ; tau(3)=18.75d0
      Pt0(2)=16.40d0 ; tau(2)=28.25d0
      Pt0(1)=14.50d0 ; tau(1)=60.00d0
```

```
      Pt0(0)=9.25d0 ; tau(0)=1.d100

      do i=0,vmax
       sum=pt0(i)+sum
      enddo

! Calculate the coefficients a(v,v'):
      do i=vmax,0,-1
        do j=vmax,i,-1
          if(j.eq.i)then
            sum=0.d0
            do k=vmax,i+1,-1
              sum = sum + a(i,k)
            enddo
            a(i,i)=Pt0(i)-sum
          else
            a(i,j)=a(i+1,j)/( tau(i+1) * ( (1/tau(i)) - (1/tau(j)) ) )
          endif
        enddo
      enddo

      do j=0,11
      t=0.d0+40.d0*j
      open(unit=1,file="Vibration_Population.dat")
      do v=0,vmax
! To calculate P, first I need calculate first the sumatori involve:
        sum=0.d0
        do i=v+1,vmax
          sum = sum + a(v,i)*dexp(-t/tau(i))
        enddo
        p=a(v,v)*dexp(-t/tau(v)) + sum
        store(j,v)=p
      enddo
```

```
      enddo

99    format (I3,12(3X,D10.4) )
      do i=0,11
      write(1,99)i,store(0,i),store(1,i),store(2,i),store(3,i)
     + ,store(4,i),store(5,i),store(6,i),store(7,i),store(8,i)
     + ,store(9,i),store(10,i),store(11,i)
      enddo
      print*, 'Calculation finished.'
      end program main
```

Appendix C

Publications

Publications

2004

"Evidence for rescattering in intense, femtosecond laser interactions with negative ion"

J. Pedregosa-Gutierrez, P. A. Orr, J. B. Greenwood, A. Murphy, J. T. Costello, K. Zrost, T. Ergler, R. Moshammer and J. Ullrich.

Physical Review Letters, **93** (2004), 223001

"Theoretical and experimental study of the extreme ultraviolet photoabsorption spectrum of triply ionized yttrium"

P. Yeates, E. T. Kennedy, J-P. Mosnier, P. van Kampen, M. W. D. Mansfield, J. Pedregosa-Gutierrez, J. B. Greenwood, Ph. V. Demekhin, I. D. Petrov, B. M. Lagutin, V. L. Sukhorukov, L. A. Demekhina and J. T. Costello

Journal of Physics B: Atomic, Molecular and Optical Physics, **37** (2004) 4663-4680

"Time evolution of ion guiding through nanocapillaries in a PET polymer"

N. Stolterfoht,R. Hellhammer, Z.D. Pesic, V. Hoffmann, J. Bundesmann, A. Petrov, D. Fink, B. Sulik, M. Shah, K. Dunn, J. Pedregosa, R.W. McCullough

Nuclear Instruments and Methods in Physics Research B **225** (2004) 169-177

2003

"Double ionization of atomic negative ions in an intense laser field"

J.B. Greenwood, G.F. Collins, J. Pedregosa-Gutierrez, J. McKenna, A. Murphy, J.T. Costello.

Journal of Physics B: Atomic, Molecular and Optical Physics, **36** (2003), L235-L240(1)

Conferences/Workshops

2005

37th EGAS: European Group for Atomic Systems:

"An Electrostatic Ion Trap for Studies of Quantum Molecular Dynamics"

J. Pedregosa-Gutierrez, P. A. Orr, I. D. Williams, J. B. Greenwood

2004

ECAMP VIII: 8th European Conference on Atomic and Molecular Physics:

"Effects of laser polarization in strong field electron double detachment from F^-

J Pedregosa-Gutierrez, P A Orr, J B Greenwood, A Murphy, J T Costello, K Zrost, T Ergler, R Moshammer, J Ullrich

2003

QUAMP I: Quantum, Atomic & Molecular Physics Conference

"Strong Field Multiple Ionization of Negative Ions"

Greenwood J.B., Collins G.F., Pedregosa-Gutierrez J., McKenna J., Murphy A., Costello J.T.

LEIF: Low-Energy Ion beam Facilities

"Strong Field Multiple Ionization of Negative Ions"

Greenwood J.B., Collins G.F., Pedregosa-Gutierrez J., McKenna J., Murphy A., Costello J.T.